Out-of-equilibrium physics of cellular symmetry breaking orchestrated by the active cytoskeletal systems confined in cell-sized spaces

坂本, 遼太

PhD Dissertation

Out-of-equilibrium physics of cellular symmetry breaking orchestrated by the active cytoskeletal systems confined in cell-sized spaces

KYUSHU

UNIVERSITY

Department of Physics, Kyushu University

SAKAMOTO Ryota

February 25, 2022

Abstract

Symmetry and symmetry breaking are fundamental concepts that form the basis not only in basic physics but also in biological phenomena. At the single cell scale, spherical cells self-replicate by symmetric cell division, while the direction of cell migration is determined by the symmetry breaking of cell shape. In the last century, the top-down approach based on molecular biology has revealed that these cellular symmetry breaking events are driven by the "actin cytoskeleton", which consists of myosin motor proteins generating contractile forces along actin filaments. However, the physical mechanism of the symmetry breaking is still poorly understood, as the top-down approach does not provide mechanical understanding of the cellular symmetry breaking.

To overcome this bottleneck, we adopted a bottom-up approach to create "artificial cells" as a simplified model of living cells, allowing us to control cell size, protein concentration, and the cell membrane molecules, which is challenging in living cells. Moreover, artificial cells are suited to study the mechanics because they are decoupled from complex biochemical signaling that regulates the activity of the actin cytoskeleton in living cells. In Chapter 1, we outline the recent developments of in vitro systems and how it has provided key biophysical understandings of the actin cytoskeleton. We also outline how the biophysical properties of the actin cytoskeleton have been characterized by the theoretical framework called "active gel theory", which describes the mechanics and dynamics of the active cytoskeletal systems.

Although previous studies revealed the biophysical properties of the actin cytoskeleton, the underlying physical mechanism of the cellular symmetry breaking is still poorly understood. To establish the simple physical understanding of cellular symmetry breaking, we develop simplified artificial cell models that recapitulate the following characteristic symmetry breaking of the biological phenomena:

1. Symmetry and symmetry breaking of cell nucleus positioning

2. Spontaneous migration driven by the symmetry breaking of cell shape

3. Rotational symmetry breaking of the contractile actomyosin wave

In this thesis, combining the simplified artificial cells with quantitative image analysis and physical analysis based on active gel theory, we explored the underlying physical mechanism of cellular symmetry breaking.

In Chapter 2, I explore how the position of the cell nucleus is controlled by the actin cytoskeleton. To make an artificial cell model of the nucleus positioning, we encapsulated both the cytoplasmic actin-myosin networks and a spherical 'cluster' (a model of cell nucleus) into water-in-oil droplets. Notably, we found that the cluster was located at the center in large droplets, while the cluster was located around the edge in small droplets. Based on the image analysis, we found that the inwardly contracting actin wave exerts a centripetal force on the cluster, while actin bridges were outwardly contracting the cluster. Based on this observation, we proposed a "tug-of-war model" in which the cluster position is determined by the balance of these two antagonistic forces. Combining the active theory and the molecular perturbation experiments, we showed that the positioning symmetry breaking occurs when the characteristic time scale required for the maturation of the bridge becomes faster than the period of wave. Together, this result will shed the light on the long-standing question of the nucleus positioning in cell biology from the mechanical point of view.

As Pierre Curie described "it is the asymmetry that creates phenomena (P. Curie, 1894)", symmetry breaking could trigger higher-order biological phenomena. In Chapter 3, indeed, we realized the spontaneous migration of artificial cell droplets by implementing the symmetry breaking of the droplet shape in addition to the positioning symmetry breaking. We found that the actin flow was propagating in the direction opposite to the migrating direction, where the physical interaction between the actin flow and the lipid membrane generates the driving force, which we called active friction. Furthermore, by sandwiching the droplets between the glass substrates,

we showed that the migration velocity decreased when the spacing was narrowed. We theoretically explained this geometrical dependence by the balance between active friction and viscous resistance, by which we elucidated the physical basis of the actomyosin-based motility that utilizes the surrounding environmental constraints.

In Chapter 4, by strengthening the binding between actin filaments and the lipid membrane interface, we induced the rotational symmetry breaking of the ring-shaped actin wave and realized various actin wave dynamics from actin flow to rotational wave. Such rotational symmetry breaking of actin wave have been reported in various cell types, while the underlying physical mechanism that drives the symmetry breaking is still poorly understood both theoretically and experimentally. We constructed a numerical simulation to explain the phase diagram of various wave phenomena: flow, ring-shaped wave, and rotation wave. Combining the numerical simulation with the molecular perturbation experiments, we elucidated the key factors of the transition, which are the strength of contraction force and the polymerization speed, and proposed the physical mechanism that breaks the symmetry of the active gels.

Before closing the Abstract section, it is worthy to mention the phrase "What I cannot create, I do not understand. (R. P. Feynman, 1988)", which is the basic idea of the bottom-up artificial cell approach to reconstruct complex living cells from building blocks. In the Conclusion section, we discuss the future perspective of artificial cell research and out-of-equilibrium physics of the actin cytoskeleton. The physical principles revealed by artificial cells not only provide new insights into how cell functions are controlled through symmetry breaking, but also enable us to develop a unified theory of active gels by extracting the characteristic symmetries from different biological phenomena. Thus, we believe our approach will open up a new avenue of "our-of-equilibrium physics of life", where artificial cells recapitulating the characteristic symmetries of living cells reveal the physical laws underlying cellular symmetry breaking, providing an integrative understanding of the biological phenomena.

Contents

Chapter 1

Introduction

"It is the assymetry that creates phenomena."

— Pierre Curie

1.1 Biological Phenomena and Symmetry Breaking

Symmetry and symmetry breaking play fundamental roles in physics, such that the energy conservation is derived from the translational symmetry of time [1], macroscopic magnetization is emerged from the symmetry breaking of the microscopic alignment of spins [2], and the elemental particle of pi-meson is generated from the spontaneous symmetry breaking [3]. Notably, not only basic physics but also recent biophysics studies have suggested that the concept of symmetry breaking plays important roles in biological phenomena. For example, the positioning symmetry of the cell nucleus either at the center or the edge of the spherical cell determines the developmental process [4, 5, 6] (Fig. 1.1a), the direction of cell migration is determined by the symmetry breaking of cell shape [7] (Fig. 1.1b), and the radial retrograde flow inside of the adherent cell breaks the chiral rotational symmetry [8] (Fig. 1.1c). Although the importance of symmetry breaking in biological phenomena is getting recognized, underlying physical mechanisms are still poorly understood due to the lack of suitable experimental platforms and theoretical tools focusing on the mechanical and dynamical aspects of the cellular symmetry breaking.
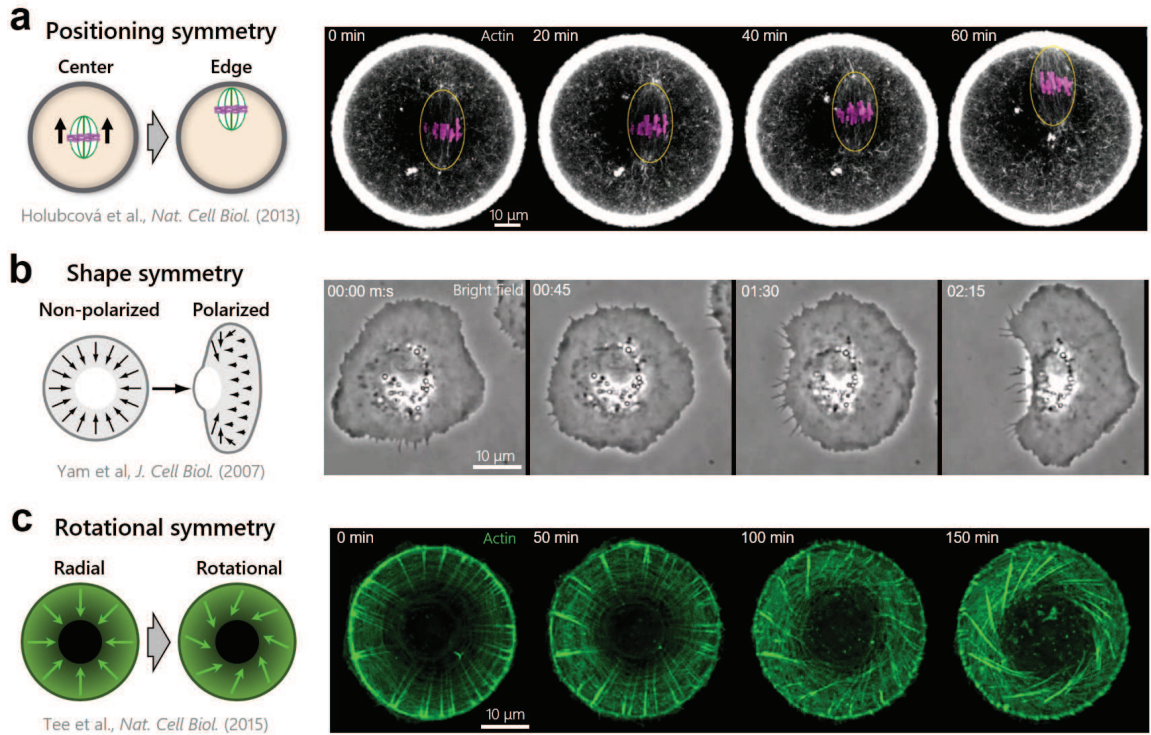
Figure 1.1: (**a**) The nucleus positioning symmetry breaking in the mouse oocyte. The position of the spindle is changed from the cell center to the edge (close to the cell membrane) just before the reductional division. (**b**) The shape symmetry breaking of the keratocyte adhered onto the glass substrate. The circular cell shape is changed to the half-circle (i.e., polarized) at the onset of the cell migration. (**c**) The rotational symmetry breaking of the radial actin flow in the fibroblasts. The radial inward actin flow is destabilized and the chiral symmetry of the flow direction is broken. Images were adapted from [12, 7, 8].

1.1.1 Cellular symmetry breaking driven by actin cytoskeleton

One of the most prominent features of biological systems is their autonomous ability to convert chemical energy into mechanical work. Importantly, the actin cytoskeleton drives most of the cellular force generation and symmetry breaking [9]. The actin cytoskeleton is mainly composed of rod-shaped actin filaments (F-actin) and the associated myosin molecular motors that generate contractile stress by coupled with ATP hydrolysis (Fig. 1.2a-c). The complex of F-actin inter-connected by myosin is called the actomyosin network, responsible for various cellular mechanics and symmetry breaking. On the one hand, a dense cortical actomyosin network underlying beneath the cell membrane drives the symmetry breaking of cell shape such as cell division [10] and polarity formation at the onset of cell migration [11] (Fig. 1.2d). On the other hand, a sparse actomyosin network exists within the whole space in cells, which controls the positioning of the cell nucleus and meiotic spindle [4, 12], and is also responsible for actin flow that drives cell migration [13] (Fig. 1.2d). Although the top-down approach of molecular biology such as genetic modification on living cells has been identified the key proteins and biochemical signaling pathways involved in the control of cellular symmetry breaking, it is still difficult to understand the underlying physical mechanism only with this top-down approach because the experiments using living cells are often limited by the narrow working conditions set by evolution and also by the cell type-specific properties. Thus, experimental systems that allow us flexible control of experimental physical parameters have been desired to test the physical hypotheses.
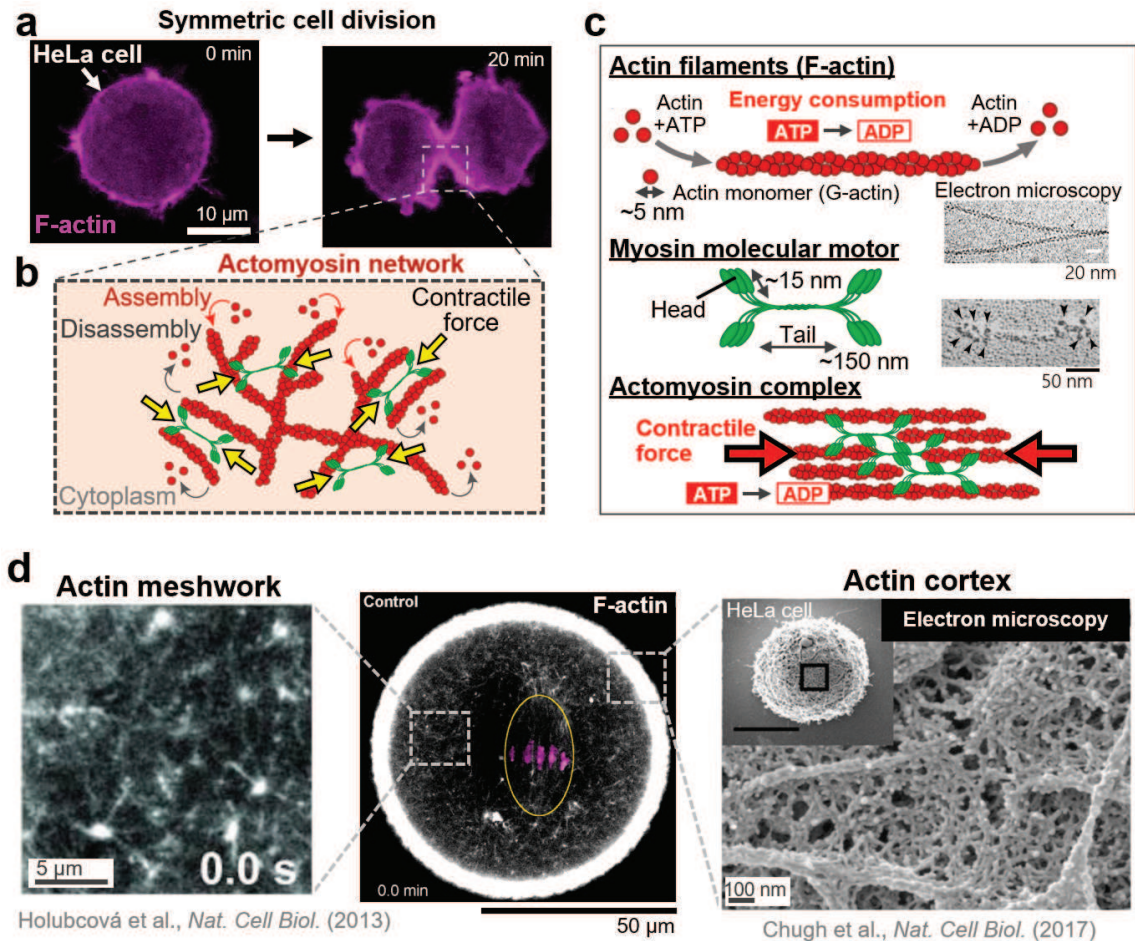
Figure 1.2: (**a**) The snapshots showing the dividing HeLa cell. The rounded spherical shape of the cell is broken by the contractile force of the actomyosin network. (**b**) Schematic of the actomyosin network. (**c**) Schematic of the actin filaments and myosin molecular motors. Actin filaments are polymerized from actin monomer (G-actin) bound with ATP, while it is depolymerized with ATP hydrolysis. Myosin motors bound to the actin filaments induce sliding stress on the filaments, resulting in the net contractile force. (**d**) Distinct states of the actomyosin network. A sparse actin meshwork is dispersed in the bulk space within the cell, while a dense actin cortex lies beneath the cell membrane. Images were adapted from [12, 14, 15].

1.1.2 Bottom-up approach: Artificial cells

To overcome the limitation of living cell studies and enable the flexible control of experimental physical parameters, simplified experimental model systems composed of minimal cellular components have been developed (Fig. 1.3a). *In vitro* reconstituted systems such as purified actomyosin network and actin-intact cytoplasmic extracts were confined in a cell-sized liposome or water-in-oil droplets to mimic living cells, called artificial cells, which have been utilized to understand how minimal components drive the cell-like self-organization. Importantly, the bottom-up reconstruction of artificial cells allows us flexible control of physical parameters, such as cell size, shape, protein concentration, and lipid composition, well-suited for experimentally testing the physical hypothesis and developing theoretical models (Fig. 1.3b) [16, 17, 18, 19, 20, 21, 22]. On the one hand, extracts-in-droplets have been used as rigid spherical confinement, in which various cell-like contractile behaviors of actomyosin networks were revealed, ranging from spontaneous actin flow [23, 24], cortical actomyosin induced shape deformation [25], connectivity induced contractility transition [26], and the control of the positioning of the nucleus-like large structure [28, 29] (Fig. 1.3c). On the other hand, liposomes (lipid bilayer vesicles) have been used to study the deformation of the cell-like lipid bilayer membrane driven by the actin cytoskeleton, ranging from spike-like membrane deformation [30] and contractile ring induced deformation [31] (Fig. 1.3d). Note that the contractility of the actin cytoskeleton is usually controlled through biochemical signaling pathways in living cells that obscures the mechanical contribution of the actomyosin network and also make it difficult to interpret the experimental results and also to construct simple theoretical models [32, 96]. On the other hand, using artificial cells, we can decouple the mechanics from biochemical signaling, so that the artificial cell system is an ideal experimental model system to investigate mechanics and the physical mechanism of the cellular symmetry breaking, well-suited to develop simple theoretical models.
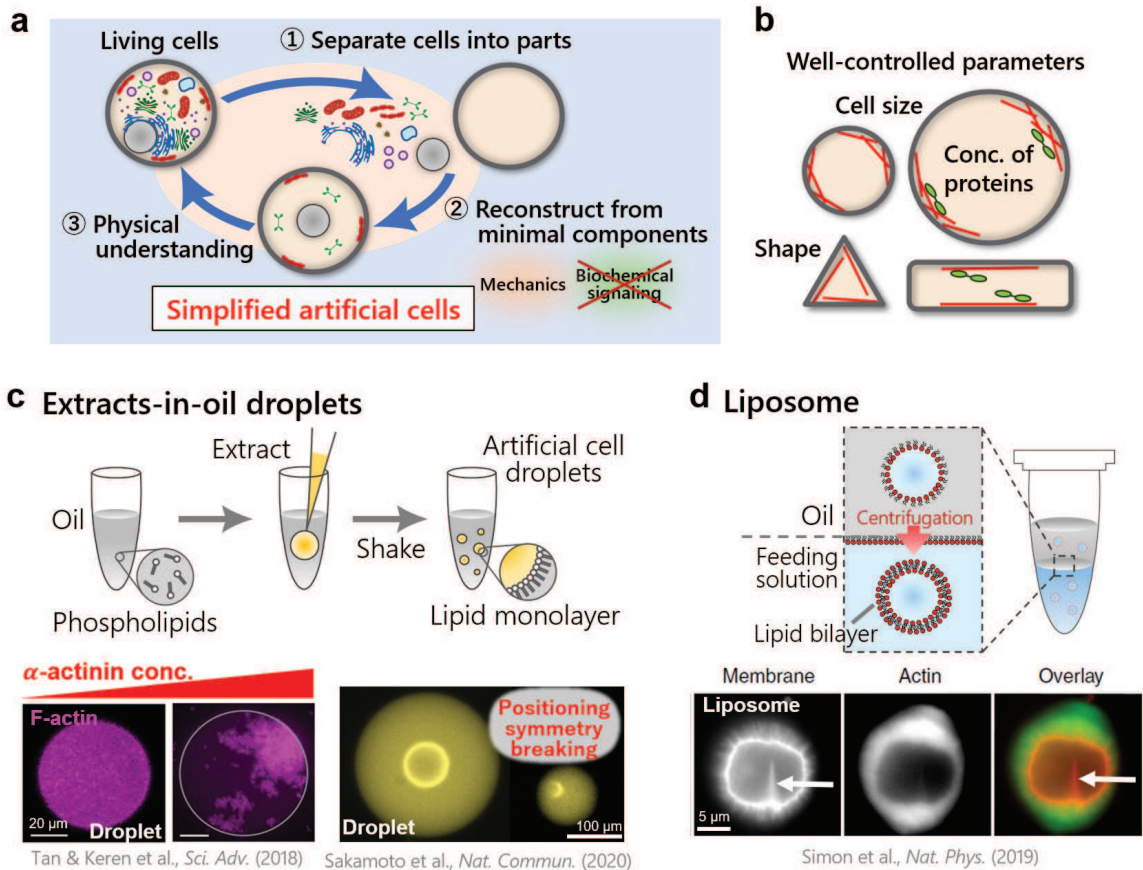
Figure 1.3: (**a**) Schematic showing the idea of the bottom-up approach to construct simplified artificial cells. (**b**) Schematic showing the advantages of artificial cells. The cell size, shape, and concentration of proteins can be flexibly controlled in artificial cells. (**c**) Preparation procedure of extracts-in-oil droplets. By mixing the extracts with the mineral oil that contains phospholipids or surfactants, one can obtain the variously-sized droplets covered with a functional lipid monolayer. The bottom images show examples of researches utilizing the droplet-based system. (Left) Increased connectivity of the network initiates the network contraction [26]. (Right) The nucleus-like large structure breaks its positioning symmetry [28]. (**d**) Preparation procedure of a liposome. After making the water-in-oil droplet, the droplets are transferred through a lipid monolayer interface, by which the lipid bilayer vesicle (i.e., liposome) can be obtained. The bottom images show the membrane deformation called 'spike' (indicated by the white arrow) induced by the polymerization of the actin network [30]. Images were adapted from [26, 28, 30].

In addition, not only the cell-scale behavior of the active cytoskeletal systems, intracellular structures such as the meiotic spindle was reconstituted in vitro using *Xenopus* egg extracts, by which the spindle mechanics were quantitatively studied [33] (Fig. 1.4a-c). Moreover, artificial cells can also be used to study the gene expression using the designed DNA, by which size-scaling of the protein synthesis was revealed in the TXTL (Transcription and Translation) system using *E. coli (Escherichia coli)* extracts [34] (Fig. 1.4d-g). Together, artificial cells using purified and cytoplasmic extracts have been significantly developed in the last decades and provided fruitful understanding from gene expression to cell mechanics.
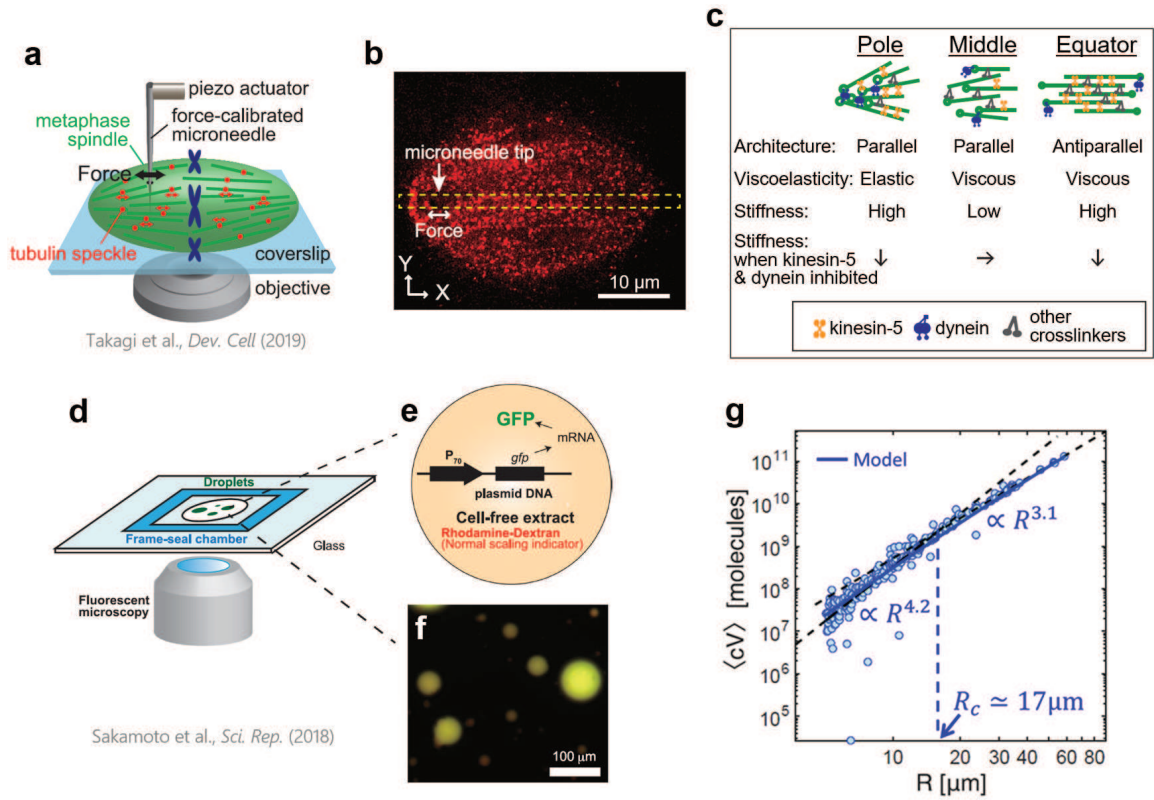
Figure 1.4: (**a**) Schematic showing the microneedle-based mechanical measurement. (**b**) Snapshot of the spindle labeled with the fluorescent tubulin speckles. (**c**) The local mechanical properties obtained by the micromanipulation. (**d**) Experimental setup of the observation chamber with the height of 300 μm. (**e**) The plasmid DNA coding the gfp as a reporter of the protein synthesis in the cell-free extract of E.coli. (**f**) The synthesized GFP intensity after 900 min. (**g**) The anomalous size-scaling of the total amount of the synthesized protein in the droplets smaller than $R_c < 17$ μm. Images were adapted from [33, 34].

1.1.3 Active gel theory: Physical descriptions of cytoskeletal systems

The recent theoretical development provided a framework to describe the non-equilibrium mechanics and self-organization of actin cytoskeleton, called active gel theory. The main difference from classical theory of polymer gels is two folded: (i) unlikely to the classic polymer gels, the crosslinking of the polymer network is not permanent but undergoes dynamic binding and unbinding of crosslinkers and also individial actin filaments changes the length by polymerization and depolymerization, where these dynamics are termed turnover [9]. (ii) Because the actin network contains myosin motor protein, this polymer network generates internal contractile stress that drives dynamic self-organization and symmetry breaking. So far, various theoretical frameworks have been proposed to describe the specific biological phenomena, such as active polar gels [36, 37], two-fluid model [38, 39], advection-reaction-diffusion systems [40, 41, 42], and agent-based simulations [43]. One of the most general frameworks was called hydrodynamic theory of active gels [44], which consists of the several set of equations. The constitutive equation for the active gel in the long-time limit is written as

$$\sigma_{ij} = \sigma_{ij}^p + \sigma_{ij}^a \tag{1.1}$$

where σ_{ij} is the total stress tensor, σ_{ij}^p is that of the passive system, and σ_{ij}^a is the new active part for active gels, which is given by

$$\sigma_{ij}^a = \zeta Q_{ij} + \bar{\zeta}\delta_{ij} \tag{1.2}$$

where the coefficients ζ and $\bar{\zeta}$ depend on the densities of motor and filament, and also the change in chemical potential $\Delta\mu$ associated with hydrolysis of ATP. Negative values of ζ and $\bar{\zeta}$ represent the spontaneous contractile behavior. The nematic order

parameter Q_{ij} in Eq. (1.2) is written as $Q_{ij} = \langle n_i n_j - \frac{1}{3}\delta_{ij}\rangle$, where n_i is a unit vector in the direction of filaments considering the myosin induced contractile stress along the actin filaments, and the average is taken over a mesoscopic volume. The stress σ_{ij}^p in Eq. (1.1) is the sum of a hydrodynamic term $\sigma_{ij}^h = \eta_b \partial_k v_k \delta_{ij} + 2\eta_s(\partial_i v_j + \partial_j v_i - \frac{2}{3}\partial_k v_k \delta_{ij})$, in which η_b and η_s are the bulk and shear viscosities, respectively, and a term σ_{ij}^{bs}, which depends on density and the broken symmetry variables. These are the terms used for equilibrium systems.

Notably, because of the turnover of crosslinkers, elastic behavior takes part in timescales shorter than their bound lifetime [44]. Assuming that these timescales are longer than microscopic times, the active gel description is extended to include the elastic regime by introducing a relaxation Maxwell time, τ_{M}, on which the network becomes fluid due to turnover of passive cross-linkers enabling network rearrangements, such that

$$\left(1 + \tau_{\mathrm{M}}\frac{\mathrm{D}}{\mathrm{D}t}\right)(\sigma_{ij} - \sigma_{ij}^a - \sigma_{ij}^{bs}) = \eta_b \partial_k v_k \delta_{ij} + 2\eta_s\left(\partial_i v_j + \partial_j v_i - \frac{2}{3}\partial_k v_k \delta_{ij}\right) \qquad (1.3)$$

where $\mathrm{D}/\mathrm{D}t$ denotes the convected corotational time derivative. On timescales shorter than τ_{M}, the time derivative in Eq. (1.3) dominates and thus the system behaves as an elastic medium with shear modulus η/τ_{M}, while on timescales longer than τ_{M}, the time derivative can be neglected and Eq. (1.1) is recovered.

By coupling the constitutive equation with the conservation equations describing the advection, diffusion, and turnover of myosin and actin filaments (Fig. 1.5a), these equations were used to describe dynamic behaviors of actomyosin networks in a wide range of time scales and length scales, ranging from blebbing [45] (Fig. 1.5b), cell division [46] (Fig. 1.5d), cell migration [47] (Fig. 1.5c), cortical flows [48], to cytoplasmic flows [49].
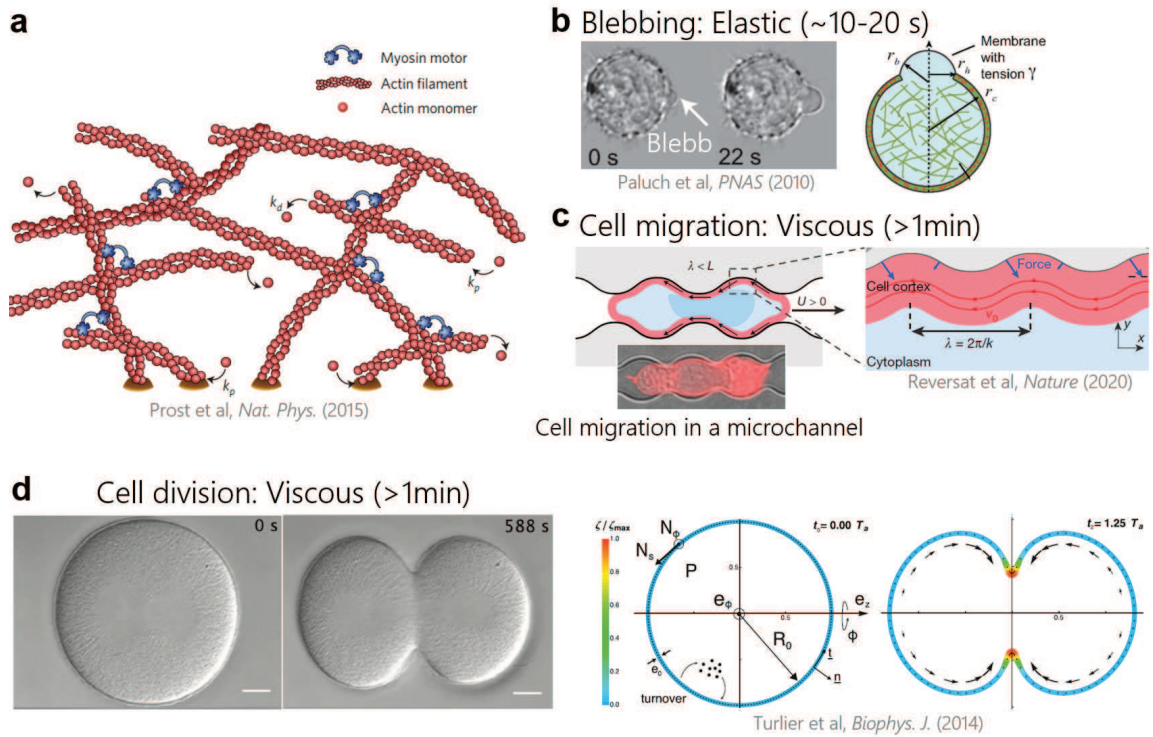
Figure 1.5: (**a**) Schematic showing the actomyosin network undergoing the polymerization and depolymerization. Actin crosslinking proteins are not shown for simplicity. (**b**) Blebbing can be described by the elastic active gel theory as its time scale is shorter than the time scales of turnover of actin filaments and crosslinker (∼10-20 s). (**c**) Schematic showing the migrating cell in a microchannel made of polydimethylsiloxane (PDMS). Cell migration is driven by the contractile actin flow which can be described as a hydrodynamic viscous active flow because of the longer time scale larger than the turnover time scales. (**d**) Cell division is typically on the order of several minutes, thus it can be described as viscous hydrodynamic active gels. (Left) Bright-field images of a dividing sea urchin zygote. (Right) Numerical simulation of the cell division. Images were adapted from [44, 45, 47, 46].

1.1.4 Active fluid model: active stress-driven symmetry breaking

Here, we briefly explain how the symmetry breaking of active gels emerges by performing a linear stability analysis on 1D active fluid model. Here, we consider the active fluid consists of actin filaments and myosin motor proteins, which is advected by the contractility induced flow of active fluid. The constitutive equation is given by

$$\frac{\partial \sigma}{\partial x} = \gamma v \tag{1.4}$$

where σ is total stress, v is the flow velocity of the active fluid, and γ is the friction coefficient describing drag on the substrate (cytosol/plasma membrane). Total stress is given by

$$\sigma = \eta \frac{\partial v}{\partial x} + \zeta \Delta \mu(c) \tag{1.5}$$

where the first term is the viscous stress, the second term is the active stress, and c is the local density of actin filaments. For simplicity, here we assume that the myosin density is proportional to the local density of actin filaments. The active stress is assumed to be given by $\zeta \Delta \mu(c) = (\zeta \Delta \mu)_0 f(c)$, where $(\zeta \Delta \mu)_0$ is the effective active stress that depends on the local number of bound myosin per actin filaments and change in chemical potential associated with ATP hydrolysis, and $f(c) = c/(c_0 + c)$ is an arbitrary function chosen to avoid contractility to diverge. In addition, mass conservation of filaments is given by

$$\frac{\partial c}{\partial t} + \frac{\partial J}{\partial x} = 0 \tag{1.6}$$

where mass flux is given by the sum of diffusion and active advection $J = -D\partial_x c + cv$. By performing a linear stability analysis around the uniform state such that $c =$

$c_0 + \delta c\, e^{\lambda(k)t + ikx}$ and $v = \delta v\, e^{\lambda(k)t + ikx}$, we can obtain the following dispersion relation

$$\lambda(k) = -k^2 D \left(1 - \frac{\text{Pe}\, c_0 \partial_c f(c_0)}{1 + k^2 l^2} \right) \tag{1.7}$$

where $l = \sqrt{\eta/\gamma}$ is the characteristic length scale, and Peclet number $\text{Pe} = (\zeta\Delta\mu)_0/\gamma D$ is the ratio of the diffusive time scale $\tau = l^2/D$ to an active advective time scale $\tau_a = l/U$ with characteristic active flow speed $U = (\zeta\Delta\mu)_0/\sqrt{\eta\gamma}$. Note that the diffusive time scale is not expected to be largely altered by active stress, thus the Pe is primaly controled by the magnitude of active stress. The instabilities of the homogeneous state is emerged when the Pe become larger than the critical value $\text{Pe}_c = (1 + k^2 l^2)/c_0 \partial_c f(c_0)$ (Fig. 1.6a-c). In this case, it was previously shown that there is a stable peak of high actin density sustained by a convergent actin flow, balanced by diffusion away from the concentrated peak [40] (Fig. 1.6d). In addition, Moore et al. showed that the 2-dimensional simulation of the active fluid model exihibits the more complex pattern, such as spot, stripe, and dynamically contracting network [42] (Fig. 1.6e-g). Recent numerical simulation of polymerizing actin network in infinite-half space performed by Levert and Kruse also reported a chaotic contractile behavior of the actomyosin network [50]. Together, this simple theoretical analysis shows that the active gel theory is a useful tool to describe the symmetry breaking and pattern formation of the active cytoskeletal systems.
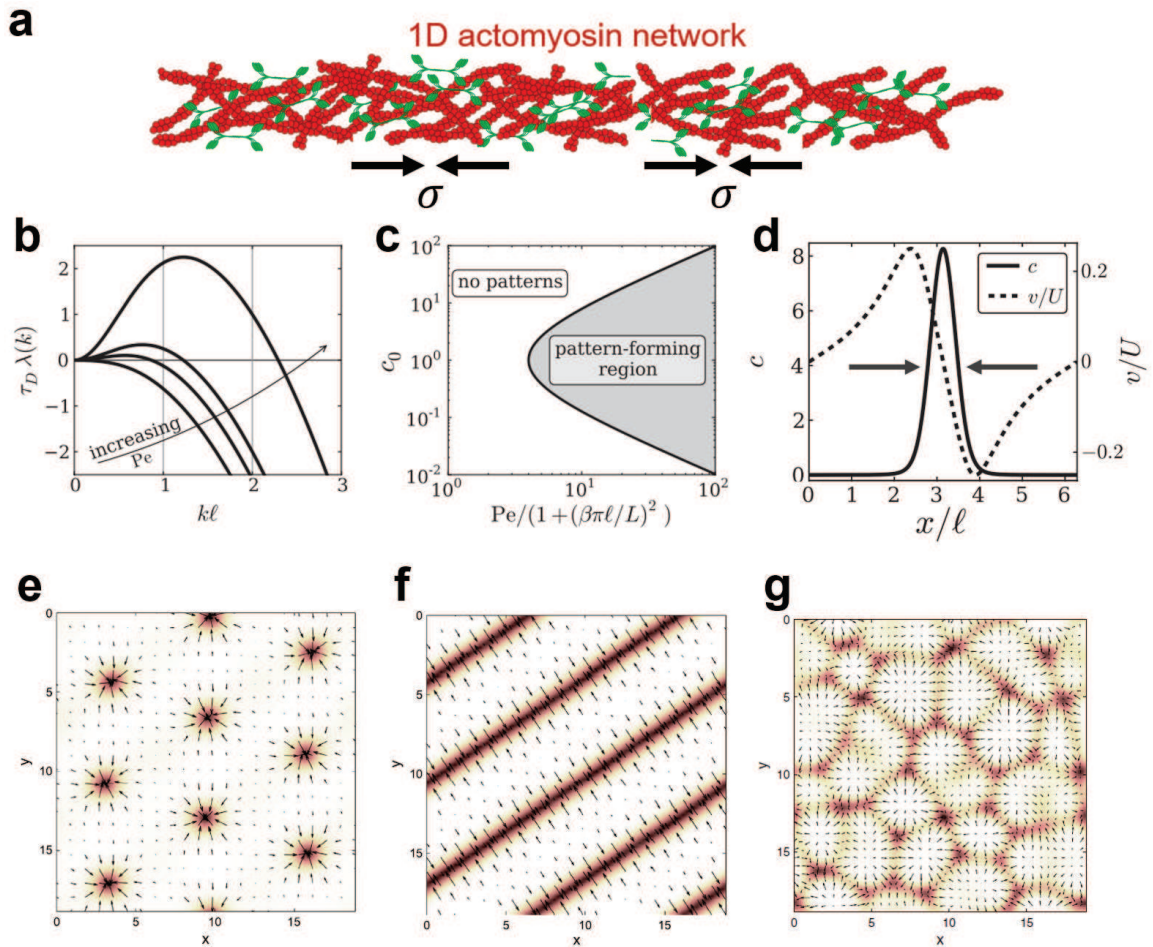
Figure 1.6: (**a**) Schematic of the 1-dimensional actomyosin network subjected to the internal total stress σ. (**b**) The dispersion relation of Eq. (1.7). (**c**) The phase space of the pattern forming instability calculated from Eq. (1.7). (**d**) The numerically calculated steady-state of Eqs. (1.4)-(1.6). (**e-g**) Numerical simulation of the two-dimensional active fluid. (**e**) Spot pattern. (**f**) Stripe pattern. (**g**) Dynamically merging network. Images were adapted from [40, 42].

.

1.2 Cytoplasic Extracts to Maintain Physiological Turnover

One of the most important abilities of actin filaments is the turnover, in which the cycle of polymerization and depolymerization enables cells to reuse the actin monomer again. The turnover of actin filaments plays a significant role to maintain the dynamics such as actin flow during cell migration [7, 11]. At the leading edge of the migrating cells, newly formed actin filaments are contracted to the rear edge, thereafter the accumulated actin filaments are depolymerized spontaneously or by several actin-depolymerizing proteins that prevent the depletion of the actin monomer pool [51] (Fig. 1.7a).

In vitro studies using purified actin and myosin, however, it is usually difficult to maintain a fine balance between polymerization and depolymerization of actin filaments, thus the contractile behavior of the actomyosin network will immediately end in several minutes [19]. Thus, static structures such as cortical actin network [17, 52] or membrane deformation [30, 53] have been mainly studied using purified systems.

To overcome such limitations in purified systems, actin-intact cytoplasmic extracts have been developed to study the dynamic property of actomyosin networks. Cytoplasmic actomyosin networks are usually prepared by the centrifugation of epithelial HeLa cells or *Xenopus* eggs [54, 16, 55] (Fig. 1.7b). Not only actin and myosin, but the cytoplasmic actomyosin networks also contain various actin associated proteins such as actin polymerizing protein Arp2/3 and Formins, actin severing (i.e., depolymerizing) protein cofilin and gelsolin, thus it can maintain the turnover and physiologically relevant actomyosin dynamics [16, 56]. In this section, we will discuss the findings given by making use of the turnover of cytoplasmic extracts.
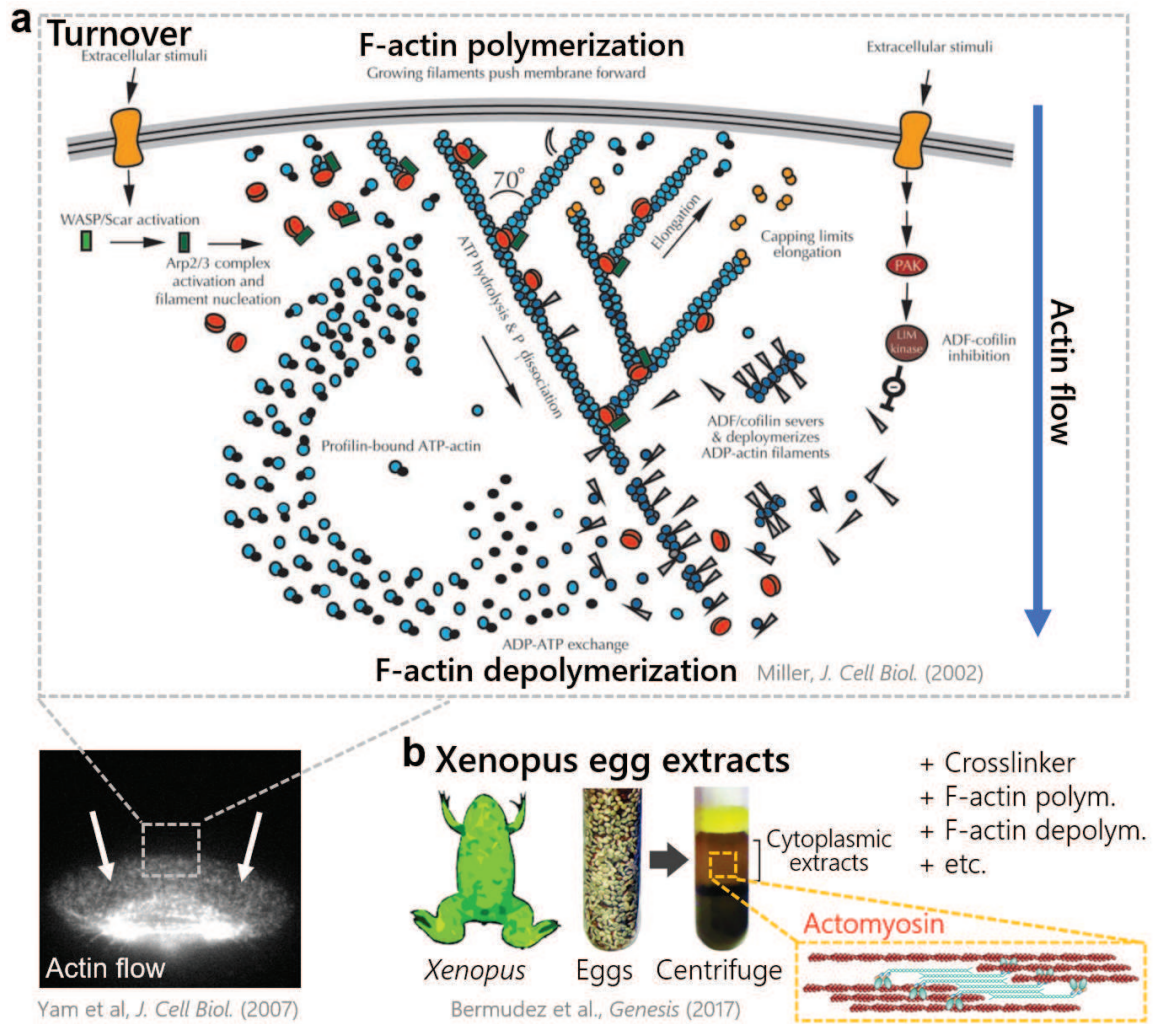
Figure 1.7: (**a**) Schematic of the turnover of actin filaments at the leading edge of the migrating keratocyte. To sustain the actin flow, polymerized F-actin must be depolymerized and reused to polymerize new actin filaments, where F-actin is actively polymerized by Arp2/3 complex and actively depolymerized by cofilin. (**b**) Cytoplasmic actomyosin networks are extracted from the *Xenopus* egg by centrifugation. Although the cytoplasmic extracts containing various actin-associated proteins are not as simple as purified systems, it sustains the turnover dynamics and enables us to study the physiologically relevant actomyosin dynamics. Images were adapted from [51, 7, 55].

1.2.1 Gelation-contraction in bulk extracts

To study the dynamic behavior of contractile actomyosin network, Field et al. developed actin-intact cytoplasmic extracts of *Xenopus* eggs [16]. Notably, they found that the periodic gelation-contraction of actomyosin networks sustained for more than 6 hours, supposed to emerge from the polymerization and depolymerization of actin filaments (Fig. 1.8a). Indeed, using *Lysteria* comets, they showed actin polymerization protein Arp2/3 is highly activated in the extracts and proposed a model of gelation-contraction (Fig. 1.8b,c). This study showed that both active polymerization and depolymerization play an important role in dynamic actomyosin contraction.
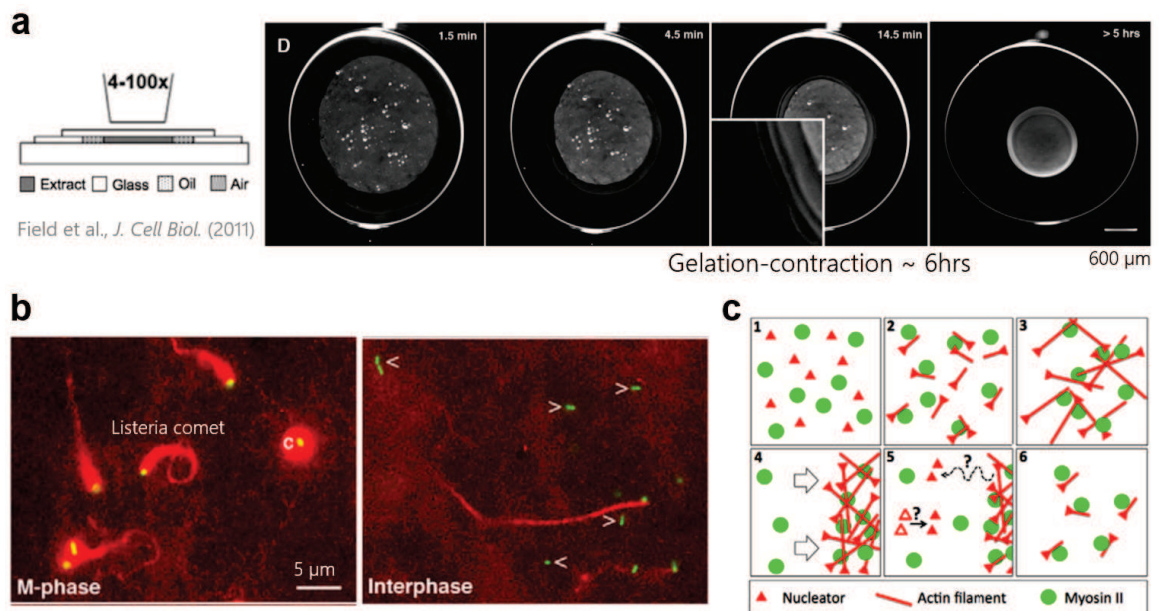
Figure 1.8: (**a**) The gelation-contraction of the bulk cytoplasmic actomyosin network extracted from *Xenopus* eggs. (**b**) *Listeria* (green) is mixed with the extracts to evaluate the activity of Arp2/3. *Listeria* is known to utilize endogenous Arp2/3 to polymerize the actin filaments to move by the counter-action of the actin polymerization. Note that the listeria comet is only visible in the M-phase extracts, suggesting that the Arp2/3 is highly activated and involved in the gelation-contraction. (**c**) Conceptual model of gelation contraction. When actin filaments are sufficiently grown and interconnected with each other, the contractile force of myosin II is transmitted over the entire network, and the whole network contracts toward the center. In the meantime, the accumulated actin network is depolymerized and supplied to the bulk, which is reused for the next gelation-contraction cycle. Images were adapted from [16].

1.2.2 F-actin turnover sustains actin flow in droplets

Migrating cells utilize the turnover of actin filaments to sustain the actin flow, in which the depolymerized actin monomers at the rear side of the cell are transported to the leading edge by diffusion [7, 51] (Fig. 1.7a). To investigate such cell-like dynamic actin flow accompanied by the actin filament turnover, Pinot et al. encapsulated the cytoplasmic actomyosin networks in cell-sized water-in-oil droplets, formed extracts-in-oil droplet [23] (Fig. 1.9a). Confocal microscopy showed the emergence of cell-like stable actin flow generated by the local F-actin assembly at the surface of the droplet (Fig. 1.9a), where Arp2/3 activating VCA domain of WASP protein is known to be recruited at the extracts/oil interface due to its partial hydrophobic nature [54] (Fig. 1.9b). Importantly, they showed that either the inhibition of F-actin assembly by Cytocharasin D or the inhibition of F-actin disassembly by Phalloidin eliminated the actin flow, indicating that the continuous turnover of actin filaments is crucial to maintain the actin flow. Together, this study revealed the significance of efficient F-actin turnover to maintain cell-like actin flow in cell-sized confined spaces.
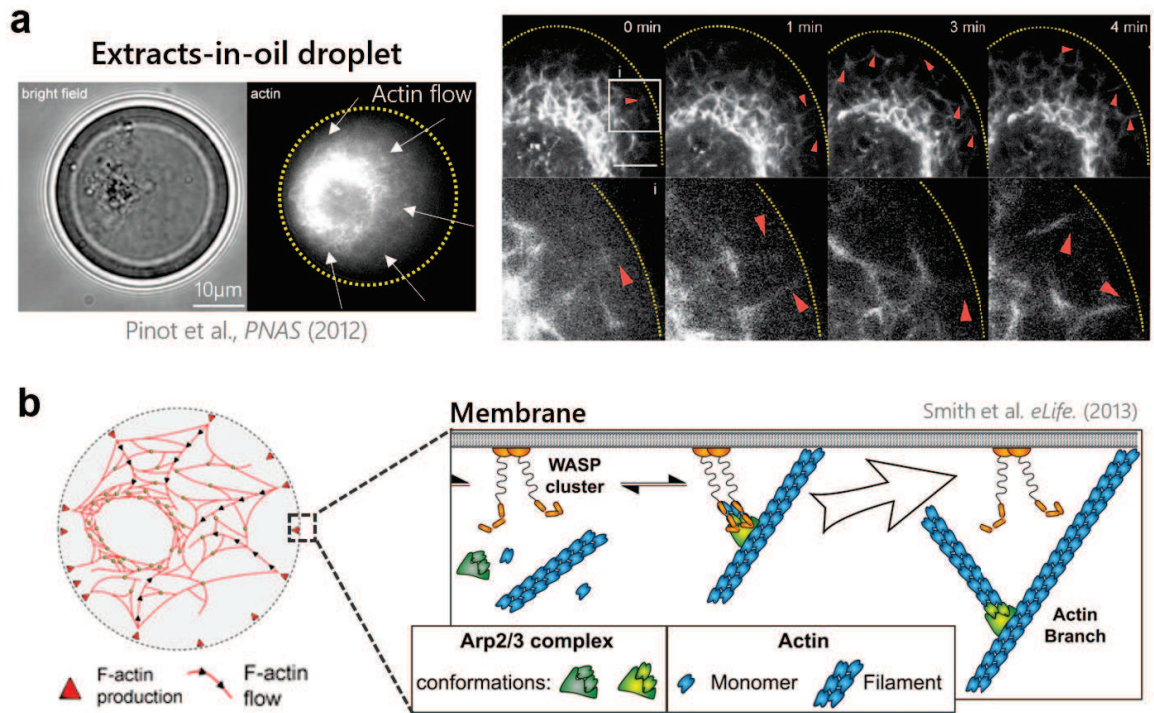
Figure 1.9: (**a**) The extracts-in-oil droplet showing inward actin flow generated from the periphery. The right zoom-in view shows the newly formed actin filaments at the surface of the droplet. (**b**) Schematic of the actin flow. The right zoom-in view shows the hypothetical mechanism of F-actin nucleation at the droplet surface, where Arp2/3 activating domain VCA of WASP protein could be localized at the extracts-oil interface due to its partial hydrophobic nature as indicated by the previous study [54]. Images were adapted from [23, 57].

1.2.3 Actin crosslinking regulates contractile behavior

In purified systems, it has been shown that the actomyosin network alone cannot effectively generate the contractile stress, but it requires sufficient actin crosslinking proteins that inter-connect the individual actin filaments [19, 27]. Then, what is the role of actin crosslinking and its turnover in cytoplasmic extracts exhibiting actin flow? To answer this question, Tan et al. developed an extracts-in-oil droplet system where the extracts were first diluted by 10 times, and then they added the actin crosslinking protein α-actinin to see the effect of network connectivity on the contractile behavior of the actomyosin network (Fig. 1.10a) [26].

To quantify the contractile behavior of the network, rod-shaped fluorescent tracer particles were mixed with the extracts and their trajectories were tracked (Fig. 1.10b). At the low α-actinin concentration (1-1.5 μM), there was just a local velocity fluctuation with correlation length $\sim$ 0.5 μm (Fig. 1.10c), which was originated from the myosin contractility induced local active diffusion of actin filaments (Fig. 1.10d). Notably, at the intermediate α-actinin concentration (2-2.5 μM), there was a large velocity fluctuation with correlation length $\sim$ 15 μm (Fig. 1.10c), indicating that the network reached critical connectivity that enabled the transmission of forces over the length scale much larger than the individual actin filaments, which is previously referred to as a signature of force percolation transition [58, 59] (Fig. 1.10d). At the larger α-actinin concentration (3-4 μM), the entire network contracted toward a single aggregate of the actomyosin network and the velocity fluctuation was small with correlation length $\sim$ 1 μm (Fig. 1.10c) because the entire actomyosin network is tightly crosslinked and formed a gel-like structure (Fig. 1.10d). Together, these results indicate that the actin crosslinking is crucial for generating an effective contractile force that spans over the entire cell-sized space.
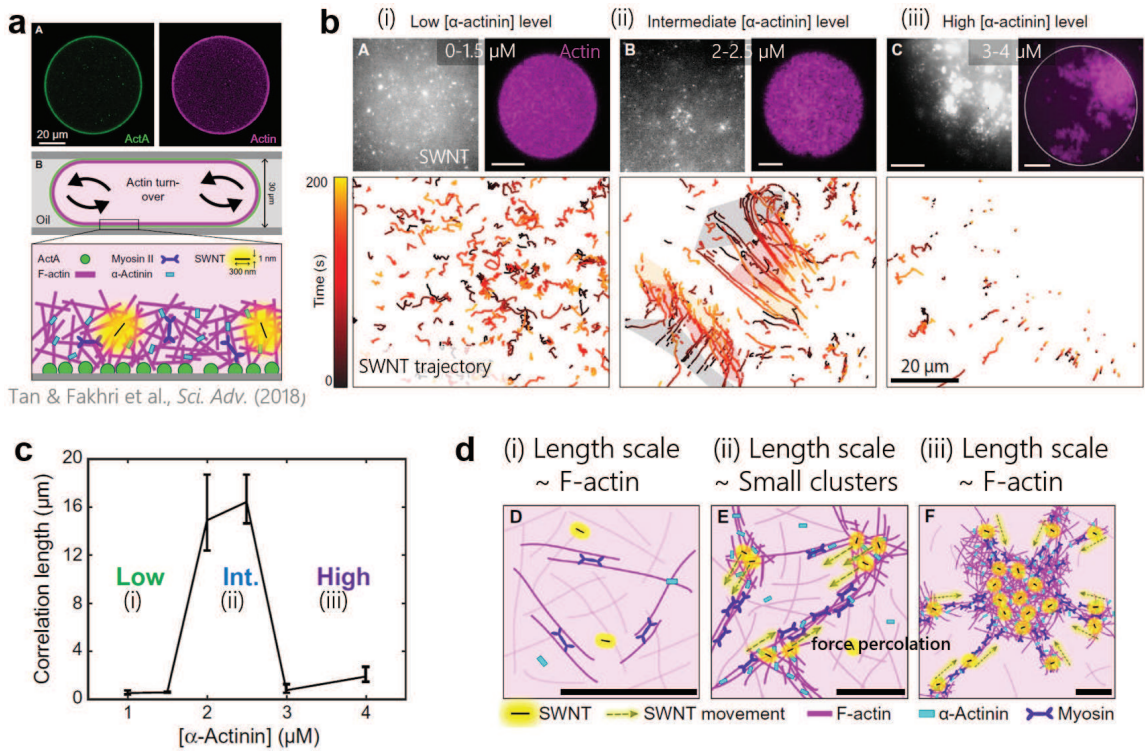
Figure 1.10: (**a**) Experimental setup. Cortical actomyosin network is formed at the surface of the extracts-in-oil droplet by localizing the Arp2/3 activating domain of ActA at the extracts-oil interface. (**b**) The α-actinin concentration-dependent state transitions of the contractile behavior of the actomyosin network. The bottom images are the trajectory of the single-walled carbon nanotube (SWNT) fluorescent probe. At a low α-actinin concentration, local fluctuation is observed. At an intermediate α-actinin concentration, large fluctuation of the small cluster region is observed, while there is no global contraction. At a high α-actinin concentration, the entire network is inter-connected and a single cluster is formed, in which the newly formed small clusters were fused to the large cluster. (**c**) The correlation length was calculated from the velocity fluctuation of the SWNT trajectories. It is notable that the correlation length takes the peak at the intermediate connectivity. (**d**) Schematic summarizing the microscopic states of the actomyosin network inter-connected with actin crosslinking protein of α-actinin. Images were adapted from [26].

1.2.4 Cell-like cortex formation and polarization

One of the distinct features of the cell is the highly-dense actomyosin network underlying beneath the cell membrane, called the actomyosin cortex [9]. Such cortical actomyosin network plays a significant role in deforming cell shape, ranging from cell division [10] to the polarization of cell shape at the onset of cell migration [11]. To reconstruct the actin cortex using cytoplasmic extracts, Shah & Keren used the actin polymerizing domain ActA conjugated with hydrophobic fluorescent marker BODYPI, by which the amphiphilic ActA complex is localized at the extracts-oil interface, forming a cell-like cortex (Fig. 1.11a) [25]. Notably, the localization of the actomyosin network at the droplet surface caused the shape deformation of the droplet, forming a local deformation called a 'cap' (Fig. 1.11b). By harnessing the simple spherical geometry of the droplet, they estimated the contractile stress of the deformation by constructing the following mechanical model of the local deformation. Given that a cytoskeletal force F per unit area is applied at the deformed region of the droplet, the Laplace equation at the deformation region is given by

$$F + \Delta P = 2\sigma \kappa_{\text{cap}} \tag{1.8}$$

where σ is the surface tension of the lipid monolayer and κ_{cap} is the local curvature of the cap region. Because the actomyosin-induced deformation is negligible in the outside of the deformed region (Fig. 1.11b), the pressure difference can be related to the local curvature κ_0 of the non-deformed region, $\Delta P = 2\sigma \kappa_0$. Substituting this to Eq. (1.8), one can estimate the contractile stress at the cap from the curvature difference as

$$F = 2\sigma(\kappa_{\text{cap}} - \kappa_0). \tag{1.9}$$

The contractile stress was estimated from Eq. (1.9) as ~ 20 pNμm^{-2}, which is ~ 10 times smaller than the epithelial cells measured from micropipette aspiration [45].

To summarize, not only this study showed that the way to reconstitute cell-like actin cortex using cytoplasmic extracts, but also showed that the simplified cell-like droplet enables one to develop the simple theoretical model and quantitative estimation, which is often challenging for liposome with lipid bilayer membrane due to its complex deformed shapes [60].
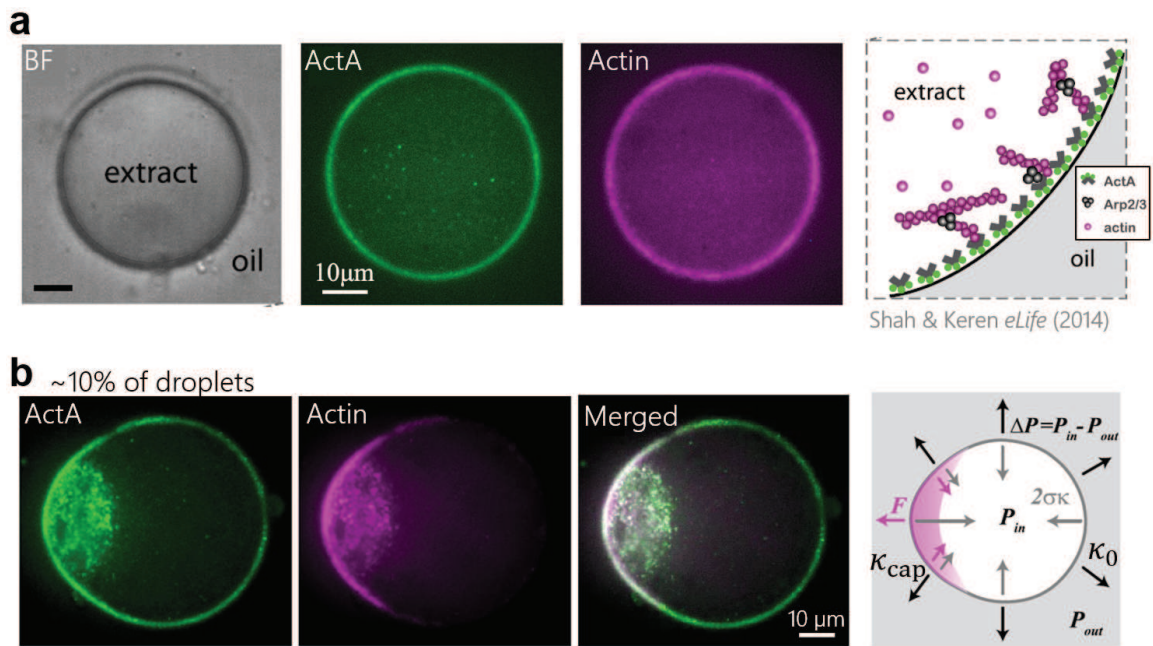
Figure 1.11: (a) Confocal images of the extracts-in-oil droplet forming cell-like actin cortex. The actin polymerizing protein Arp2/3 activating domain ActA is localized at the extracts-oil interface (right), by which the actin cortex is formed beneath the membrane due to the locally enhanced F-actin polymerization. (b) Approximately 10 % of droplets showed a polarized actin cortex. The right schematic showing the force balance of at the deformed droplet surface. Images were adapted from [25].

1.3 Active Gel Physics

The intriguing physical property of the actomyosin network is its various physical states depending on the density of F-actin, turnover rate, and the extent of crosslinking. Moreover, growing evidence suggests that such distinct actomyosin networks coexist within the cell, responsible for various biological functions. On the one hand, a dense actomyosin network is underlying beneath the cell membrane, called the actin cortex, supporting the shape of rounded cells and driving cell division [10]. On the other hand, a sparse actomyosin network is dispersed in the cell cytoplasm, responsible for the pulsatile contraction of epithelial cells [61, 62] and the positioning of the cell nucleus and spindle [4, 5]. At an intermediate density and crosslinking, notably, actin flow is responsible for the material transport [49] and also driving the cell migration [7, 13]. Together, these distinct physical states of the actomyosin network are referred to as active gels, in which physical properties and contractile behaviors were significantly altered depending on the density of F-actin, turnover rate, and the extent of actin crosslinking. Therefore, various theoretical descriptions have been developed depending on the distinct states of active gels. In this section, we will give an overview of the important theoretical descriptions used in my research.

1.3.1 Continuum description: Two-fluid model of active gels

One of the most simple way of developing active gel theory is to include the effect of active stress to the classic theory of polymer gels. Benerjee & Marchetti developed an active gel theory based on two-fluid model used in the classic polymer gel theory [38]. Here, cytoskeletal filaments are treated as a porous elastic network immersed in a viscous solvent (cytoplasm). The equation of motion of the gel is given by

$$\rho\partial_t^2\mathbf{u} = -\gamma(\partial_t\mathbf{u} - \mathbf{v}) + \nabla \cdot \sigma \tag{1.10}$$

where ρ is the density of the gel, $\mathbf{u}(r,t)$ is the displacement field of the gel, $\mathbf{v}(r,t)$ is the velocity of the permeating viscous fluid, γ is the friction coefficient between the gel and the permeating viscous fluid, where the first term in the right hand side of Eq.(1.10) is the friction between the gel and the permeating fluid. The permeating viscous fluid follows Navier-Stokes equation,

$$\rho_f \partial_t \mathbf{v} - \eta \nabla^2 \mathbf{v} + \nabla P = \gamma(\partial_t \mathbf{u} - \mathbf{v}) \qquad (1.11)$$

where ρ_f is the density of the fluid, η is the fluid viscosity. The stress tensor of the gel is composed of the sum of elastic, dissipative, active components

$$\sigma = \sigma^e + \sigma^d + \sigma^a \qquad (1.12)$$

where the elastic and dissipative part are the identical to the equilibrium system, such that

$$\sigma_{ij}^e = \left(\lambda + \frac{2\mu}{3}\right)\delta_{ij}\nabla \cdot \mathbf{u} + 2\mu\left(u_{ij} - \frac{1}{3}\delta_{ij}\nabla \cdot \mathbf{u}\right) \qquad (1.13)$$

where λ and μ is the bulk and shear Lame coefficients, and $u_{ij} = \frac{1}{2}(\partial_i u_j + \partial_j u_i)$. The dissipative part is given by

$$\sigma_{ij}^d = \eta_b \delta_{ij}\nabla \cdot \partial_t \mathbf{u} + 2\eta_s\left(\partial_t u_{ij} - \frac{1}{3}\delta_{ij}\nabla \cdot \partial_t \mathbf{u}\right) \qquad (1.14)$$

where η_b and η_s is the bulk and shear viscosity of the gel. The active stress is given by

$$\sigma_{ij}^a = \delta_{ij}\zeta(\rho, c_b)\Delta\mu \qquad (1.15)$$

where $\Delta\mu$ is the chemical potential difference due to the hydrolysis of ATP, the coefficient ζ depends on the densities of actin filaments and the bound myosin density c_b.

To complete the hydrodynamic description, we need equations describing the dynamics of bound and unbound motors with densities c_b and c_u, respectively. Assuming that the motor is bound to the actin filaments with the rate k_b and unbound with the rate k_u, mass conservation equations of the motor is given by

$$\partial_t c_b + \nabla \cdot (c_b \partial_t \mathbf{u}) = -k_u c_b + k_b c_u \tag{1.16}$$

$$\partial_t c_u = D\nabla^2 c_u + k_u c_b - k_b c_u \tag{1.17}$$

where D is the diffusion coefficient of free motor protein. Note that myosin II are classified as non-processive motor which spends unbound state most of the time during the total cycle duration [63]. In this case, we neglect the dynamics of free motor and it just acts as a motor resovior [38].

Finally, the four component active gels, composed of the gel, a viscous solvent, bound and unbound motor proteins, are closed by the incompressibility condition

$$\nabla \cdot [(1 - \phi_p)\mathbf{v} + \phi_p \partial_t \mathbf{u}] = 0 \tag{1.18}$$

where ϕ_p is the volume fraction of the gel. When the volume fraction of the network is very small ($\phi_p \ll 1$), Eq. (1.18) recovers the incombressibility of the ambient fluid, $\nabla \cdot \mathbf{v} \simeq 0$.

In the overdamped limit in 1D, the dynamic equations are reduced to

$$(\gamma - \eta_L \partial_x^2)\partial_t u = B_a \partial_x^2 u + \zeta \Delta \mu \partial_z \phi \tag{1.19}$$

$$\partial_t \phi = -\partial_x[(1 + \phi)\partial_t u] - k_u \phi \tag{1.20}$$

where $\eta_L = \eta_b + (4/3)\eta_s$, $B_a = \lambda + 2\mu - \zeta\Delta\mu$, and ϕ is the fraction of bound motors. Notably, we obtain a single differential equation for the displacement $u(x, t)$

by eliminating the bound motor fraction from these equations

$$\tau_{on}\gamma\partial_t^2 u + [\gamma - \eta_a\partial_z^2]\partial_t u = B_a\partial_z^2 u \tag{1.21}$$

where $\tau_{on} \sim 1/k_u$ is the time that the motor spends attached to the filament, and $\eta_a = \tau_{on}[B - \zeta\Delta\mu]$. The Eq. (1.21) indicates that the motor on/off dynamics provides the effective inertia to the dynamics of the network. Indeed, linear stability analysis and the numerical calculation of the active gel showed that there is a spiring-like oscillatory state and propagating waves [38, 39, 42] (Fig. 1.12a,b). A recent experiment of the purified actomyosin networks used the two-fluid model to explain the macroscopic contractile behavior of the gel, in which numerical calculation of the two-fluid model quantitatively reproduced the contractile speed of the gel using relevant material parameters [64] (Fig. 1.12c,d). Therefore, the two-fluid model showed that the active stress contribute to realize the dynamic contractile behavior of the active cytoskeletal network, which is the characteristic behavior of the active systems that cannot emerge in the classic equilibrium polymer gels.
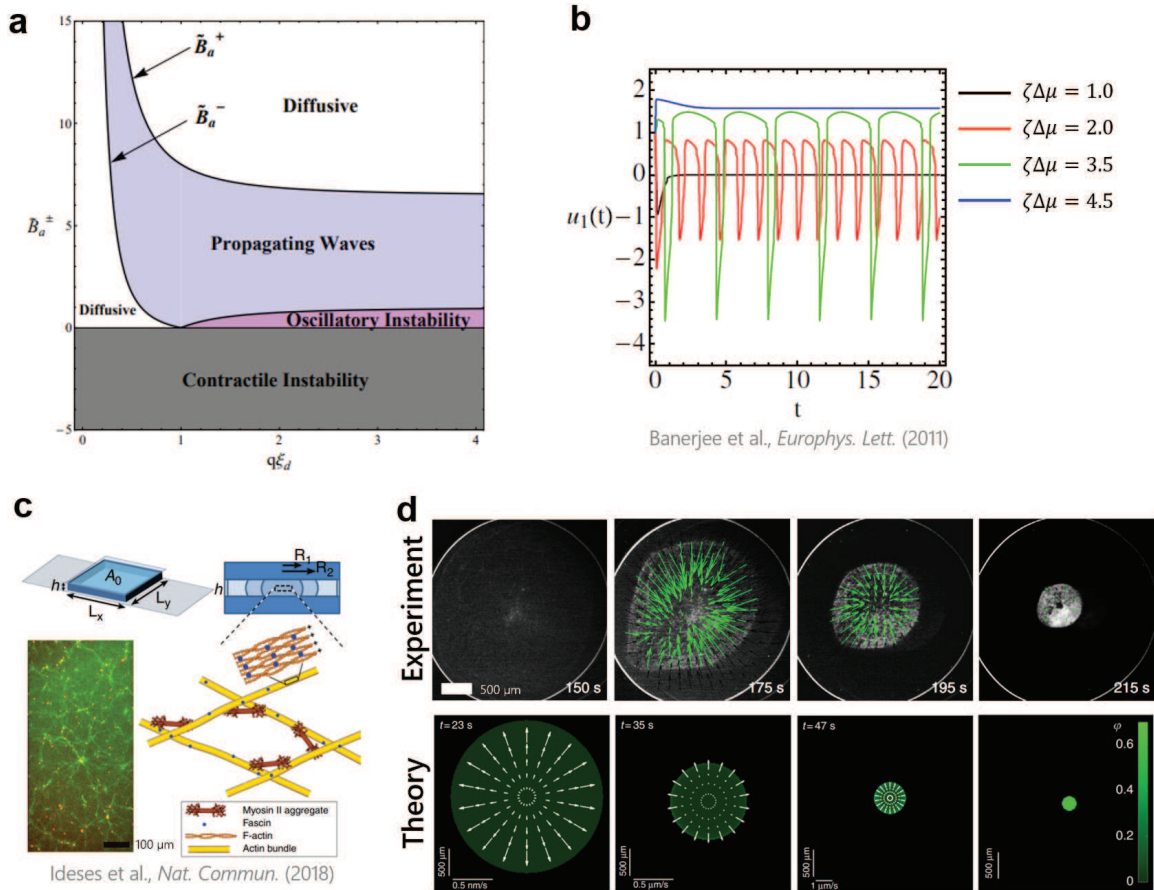
Figure 1.12: (**a**) Phase diagram calculated from Eqs. (1.19) and (1.20). (**b**) Numerically calculated oscillatory dynamics of the 1D non-linear two-fluid model [39]. (**c**) Schematic showing the experimental setup of the bulk actomyosin network contraction. The purified actin and myosin with actin crosslinking protein fascin are mixed and sandwitched between the glass substrates. (**d**) Comparison of the dynamics of the contracting actomyosin network between the experiment and the numerical simulation of the two-fluid model. Images were adapted from [38, 39, 64].

1.3.2 Agent-based model: Turnover controls the contractile behavior

In vitro experiments showed that sufficient actin-crosslinking is necessary to induce the contractile behavior, however, considering the myosin motor bound to the actin filaments, contractile and expansile states would be averaged out under the framework of linear elastic theory (Fig. 1.13a). How can the contractile state outweigh the expansile state through actin-crosslinking and turnover? To answer this question, Hiraiwa & Salbreux considered the simplest situation where the rod-shaped filaments are inter-connected by crosslinkers, and bound motor induce force along the filaments [43] (Fig. 1.13a). They showed that in the presence of crosslinkers, the bias towards the contractile stress arises from instabilities of the expansile configuration of filaments, thereby the contractile force dipole at final configuration becomes always positive (Fig. 1.13b).

On the other hand, in the case of a macroscopic network containing several thousands of filaments confined in a box, they found that the ratio between the filament turnover rate τ_f and the crosslinker turnover rate τ_c controls the contractility applied at the periphery of the box (Fig. 1.13c). For $\tau_f \gg \tau_c$, contracted filaments formed a cluster, whereas for $\tau_f \ll \tau_c$, filament turnover is too fast to reconfigure the filaments to the contractile configuration, thus the contractile stress applied on the wall is decreased. Therefore, the contractile stress takes the maximum value at an intermediate turnover ratio $\tau_f/\tau_c \sim 0.1 - 1$ (Fig. 1.13d). Interestingly, this value corresponds to the experimentally measured values of turnover rate of actin and cross-linker in the cell cortex, $\tau_f \sim 15 - 45$ s and $\tau_c \sim 7 - 14$ s, $\tau_c/\tau_f \sim 0.15 - 1$ [9]. This kind of state transition may be relevant to the crosslinker concentration dependence of the contractile behavior of the cytoplasmic actomyosin networks explained in section 1.2.3. Together, not only the presence of crosslinker plays an important role in effectively generating contractile stress on the network, but also the turnover of filaments and

crosslinkers crucially controls the contractile stress generation.
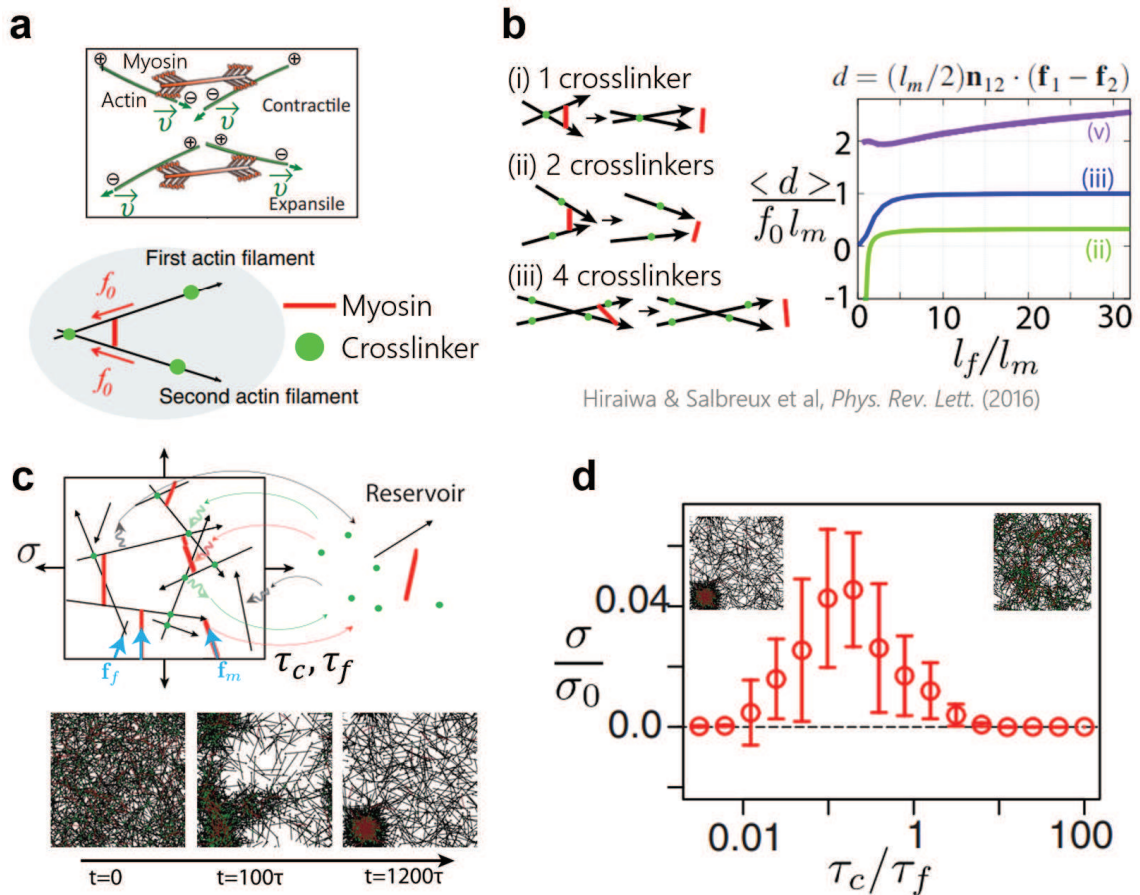
Figure 1.13: (**a**) Schematic of the myosin bound to actin filaments. Because the myosin walks on the actin filaments toward the + end, either the contractile or expansile forces are exerted to the filament depending on the configuration. The bottom simplified schematic shows a configuration of the agent-based simulation, where bound myosin (the red bar) exerts a force f_0 to the filament (+ end is denoted as the arrow) inter-connected by crosslinker (the green circle). (**b**) The force dipole of myosin d at the final configuration (i)-(iii) is calculated, where l_f and l_m denote the length of filaments and myosin, respectively. Note that the contractile configuration is stable in any configuration. (**c**) The macroscopic contractile stress of the network σ is calculated by confining the actomyosin network in a box, where all the components undergo turnover to the reservoir. The turnover rates of myosin motor, actin filaments, and crosslinker are denoted as τ, τ_f, and τ_c, respectively, where $\tau_f > \tau$ and $\tau_c > \tau$. The bottom images show the time course of the simulation. (**d**) The turnover rate dependence of the total stress. At $\tau_f > \tau_c$, clustering occurs, while at $\tau_f < \tau_c$, the filament turnover is too fast to reconfigure the filament to contractile configuration, thus the contractility take maximum at the intermediate ratio $\tau_f \sim \tau_c$. Images were adapted from [43].

1.3.3 Active fluid model: Friction force generated by actin flow

So far, we have been focused on the contractile behaviors of the actomyosin network within the cell body. On the other hand, cells must transmit intracellularly generated contractile stress to the external surrounding environments to propel the cell body forward during cell migration. The well-studied classic example is the cell migration on 2D substrate, in which focal adhesion efficiently transmits traction forces [65] (Fig. 1.14a). In contrast, recent studies showed that adhesion-independent migration is possible in 3D confinement such as microchannel and collagen network even in the absence of focal adhesion [13, 66, 47] (Fig. 1.14b). Importantly, when the substrate friction is reduced, this cell migration slows down (Fig. 1.14b). Based on this observation, the friction force generated by the physical interaction between the actin flow and the substrate was proposed as a propulsion force (Fig. 1.14c). The constitutive equation of the cortical actin flow is given by

$$\sigma_{ij} = \eta_b \partial_k v_k \delta_{ij} + \eta_s \left(\partial_i v_j + \partial_j v_i - \frac{1}{2} \partial_k v_k \delta_{ij} \right) + \zeta \Delta \mu \delta_{ij} \tag{1.22}$$

where η_b and η_s are the bulk and shear viscosity, v_k represents the cortical actin flow velocity, $\zeta \Delta \mu$ is the active stress. Here, only the viscous contribution of the actin flow was considered because the typical time scale of actin flow is on the order of minutes, while the turnover rate of crosslinker was $\sim$20 s, thus the elastic energy stored in the network is released [13].

They separately considered the constitutive equation of the actin flow at the contact region where the cell is in contact with the wall and the non-contract region at the front and rear part. First, the pressure difference acts as a drag of the medium

acting against the motion of the cell,

$$P^r_{out} - P^f_{out} = -\alpha_D U \tag{1.23}$$

where U denotes the migration velocity of the cell, α_D is the effective drag coefficient (Fig. 1.14c). The fluid drag is related to the stress tensor through the normal force balance given by the Young-Laplace equation

$$C_{ij}\sigma_{ij} = P_{in} - P_{out} \tag{1.24}$$

where C_{ij} is the curvature tensor of the cell surface

Second, as the actin flow propagates from the front to the rear side of the droplet, external shear stress acts on the region where the cell is in contact with the wall, $\Sigma_{out} = -\alpha v$, where v is the relative velocity between the actin flow and the substrate, and α is the associated friction coefficient at the cell-substrate interface (Fig. 1.14c). The tangential force balance is then given by

$$\nabla \cdot \sigma = \alpha v \tag{1.25}$$

Together with the constitutive equation Eq. (1.22), cortical actin flow speed is determined by the contractile force gradient between the front and rear part of the droplet,

$$\eta \partial_x^2 v = \alpha(v + U) - \partial_x \zeta \Delta\mu \tag{1.26}$$

where $\eta \equiv \eta_s = 2\eta_b$, and v is now velocity taken in the cell reference frame. Note that Eq. (1.26) corresponds to the Stokes equation with a positive pressure gradient (in this case, active stress). Together with the force balance at the rear and front side Eq. (1.24), they derived the substrate friction dependence of the cell migration speed, which reproduced the experimental results (Fig. 1.14d). Thus, this study showed

that the friction force generated at the substrate-membrane interface is sufficient to propel the cell body forward. Note that recent studies showed that the hydrodynamic theory describing the actin flow as a Stokes flow could explain the force generation in various situations such as cell migration through zero-friction microchannel [47] and the deformation of liposome induced by polymerized actin flow [30], suggesting that the hydrodynamic description can well capture the forces generated by contracting actomyosin networks.
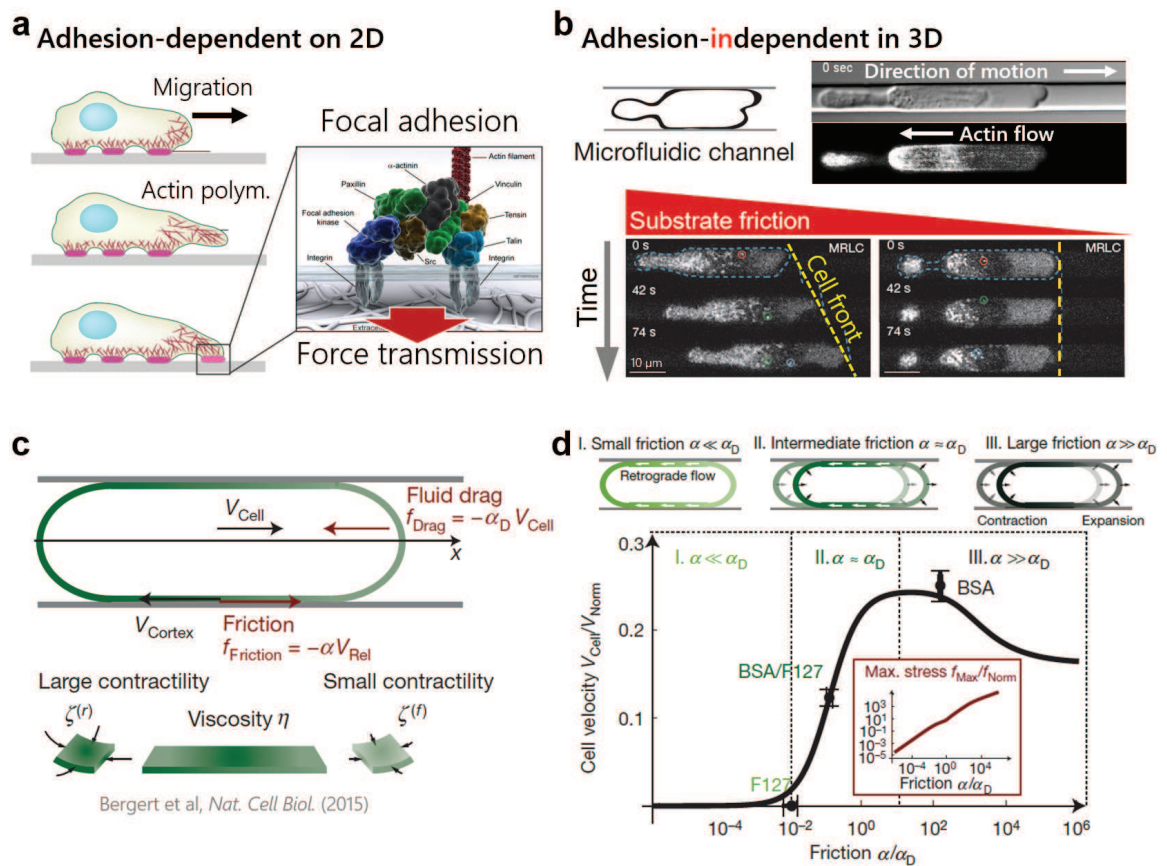
Figure 1.14: (**a**) Schematic of the adhesion-dependent migration on 2D substrates, where focal adhesion complex effectively transmits intracellular contractile forces to the external substrates. (**b**) Schematic and images of the adhesion-independent migration under the microfluidic channel. The migration slows down by decreasing the substrate friction with polymer blush. (**c**) Schematic showing the forces applied on the cell body. The friction force drives the cell migration, while the external fluid drag counteracts the cell movement. The viscous actin flow is sustained by the gradient of the contractile stress over the cell body. (**d**) The substrate friction dependence of the cell velocity. Images were adapted from [67, 68, 13].

1.4 Toward Understanding Cellular Symmetry Breaking *In Vitro*

In Chapter 1, we discussed how artificial cell systems reveal the simple physical mechanism of the self-organization of the actomyosin network, and how active gel theory can describe the dynamic behavior of the contracting actomyosin networks. However, although molecular determinants of contractile behavior have been uncovered, less is known about how the cellular symmetry breaking is driven by the mechanics of the actomyosin network. This is because the previous studies mainly focused on the biophysical properties of the actomyosin network, such as the effect of F-actin turnover on sustained actin flow [23, 29] and the effect of actin-crosslinking on contractile behavior [26]. Thus, the underlying mechanism of the cellular symmetry breaking is still poorly understood. To establish a simple physical understanding of the cellular symmetry breaking, it is necessary to develop a simplified artificial cell model that extracts the characteristic symmetry breaking of the biological phenomena. To this end, we develop artificial cells that recapitulate the positioning symmetry breaking, shape symmetry breaking, and rotational symmetry breaking, which enables us quantitative image analysis and physical analysis using active gel theory (Fig. 1.15). Combining the flexible control of experimental parameters and theoretical modeling using artificial cells, we will uncover the physical principle underlying the cellular symmetry breaking that is obscured by the rich complexity of living cells. In the following Chapters, we will show the outcomes of the research.
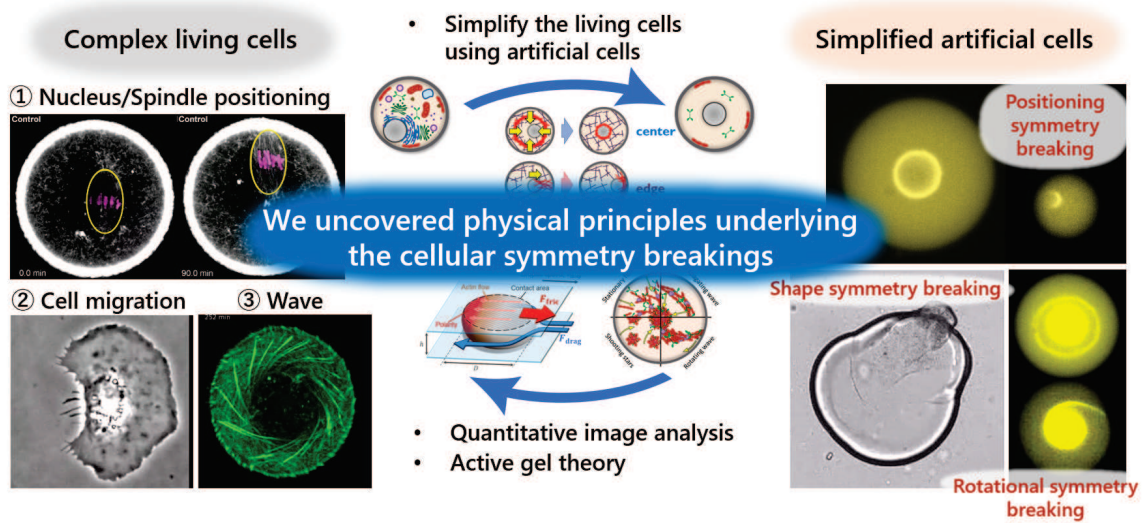
Figure 1.15: Schematic summarizing the ideas and research in this thesis. By extracting the characteristic symmetry breaking of the living cells using artificial cells, quantitative image analysis and the development of active gel theory will be enabled, which will allow us to uncover the physical principles underlying the cellular symmetry breaking. Images were adapted from [12, 7, 8].

Chapter 2

Intracellular Symmetry and Symmetry Breaking

2.1 Introduction

2.1.1 The roles of symmetry in biological systems

Intracellular symmetry and symmetry breaking play pivotal roles from cell migration to developmental processes. Cell migration onset is determined by the symmetry breaking of cell shape [7, 11] which navigates the direction of the motion, while asymmetric cell division occurs during the developmental processes that determine the head-and-tail polarity [69]. Among such symmetry breaking events, one of the most important phenomena that is mainly driven by actomyosin networks is the 'nucleus positioning' [70]. In the mouse oocyte, which is the pre-matured egg cells before reductional cell division, the cell nucleus takes the two distinct positions; either the center or the edge [4, 5, 6] (Fig. 2.1a,b). If the positioning is failed, an abnormal number of chromosomes are allocated into the daughter cells, causing birth defects disease [72, 73, 74, 71]. Therefore, the nucleus positioning is the fundamental process of development. However, the physical mechanism of the nucleus positioning is still elusive [75], because the complex biochemical signaling pathways and narrow working condition of mouse oocytes hindered us to quantitatively test the different physical hypotheses, such as cytoplasmic flow-induced positioning [76, 77] (Fig. 2.1d), actin meshwork driven contraction [5, 12] (Fig. 2.1b), and actin comet-like pushing force [78, 79] (Fig. 2.1c).

2.1.2 Artificial cell as a model of nucleus positioning

To simplify the problem, we develop an in vitro artificial cell model which shows cell-like nucleus positioning. It has been known that cytoplasmic extracts systems using *Xenopus* egg show that a single spherical aggregate is formed inside the droplet, which is initially formed by the contraction of actomyosin networks [23, 26, 24]. However, none of the previous studies have so far investigated how the position of the spherical aggregates is determined by the contractile actomyosin networks. In this study, we regard this spherical object as a model of the cell nucleus, called a cluster, and studied how the positioning of the cluster is controlled by the contractile actomyosin networks in the artificial cells (Fig. 2.2).
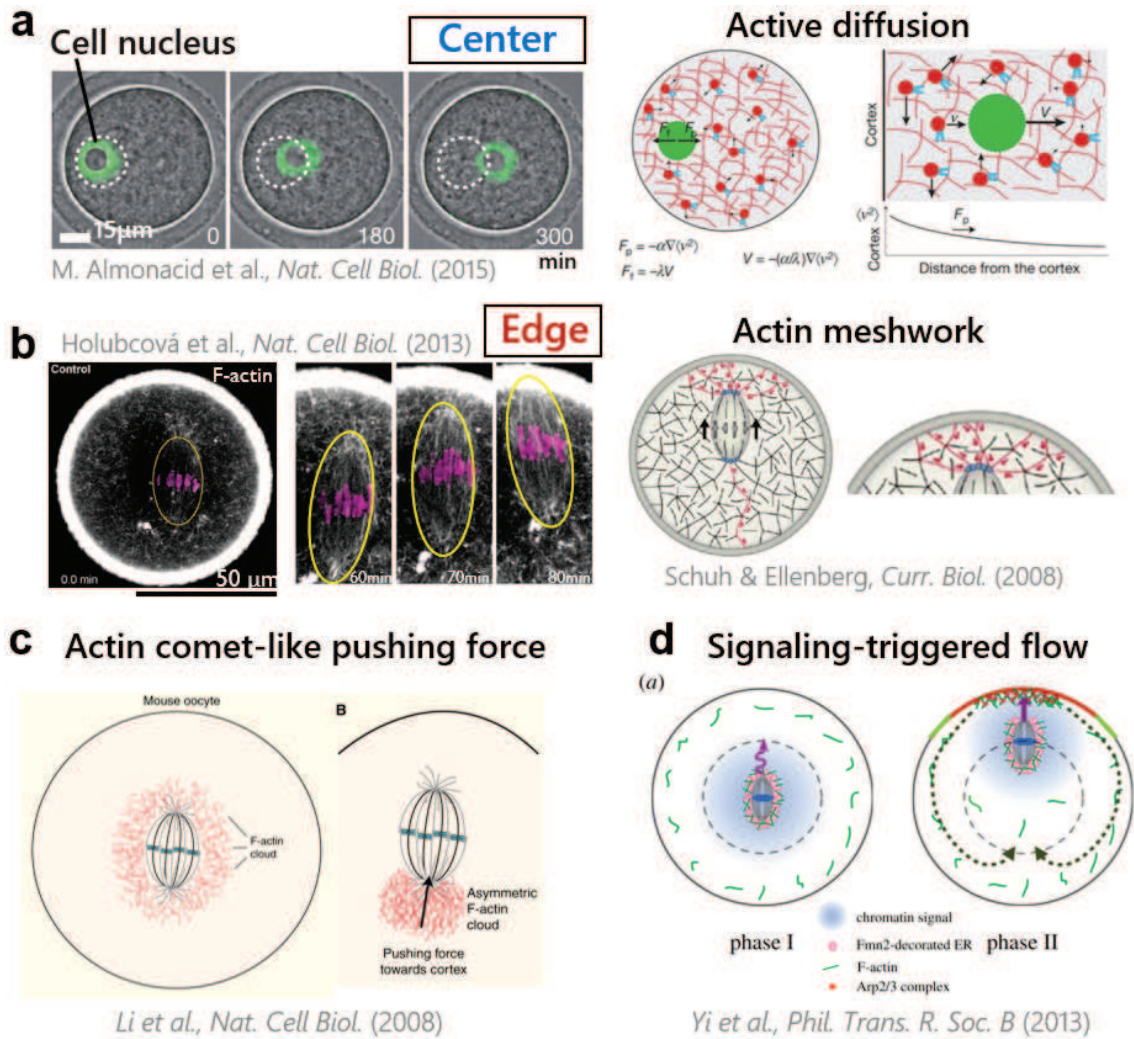
Figure 2.1: (**a**) Nucleus positioning toward the center of the mouse oocyte, which is proposed to be driven by the active diffusion induced by Myosin Vb. (**b**) Spindle positioning toward the edge, which is proposed to be driven by the contractile actin meshwork connecting the cluster and the cell membrane. (**c**) The other group proposed the mechanism of the positioning symmetry breaking driven by the actin polymerization induced pushing force. (**d**) The other group proposed that the signaling triggers Arp2/3 mediated polymerization when the spindle is approached sufficiently close to the cell membrane, by which the cytoplasmic flow pushes the cluster toward the edge. Images were adopted from [4, 12, 76, 77, 78, 79].
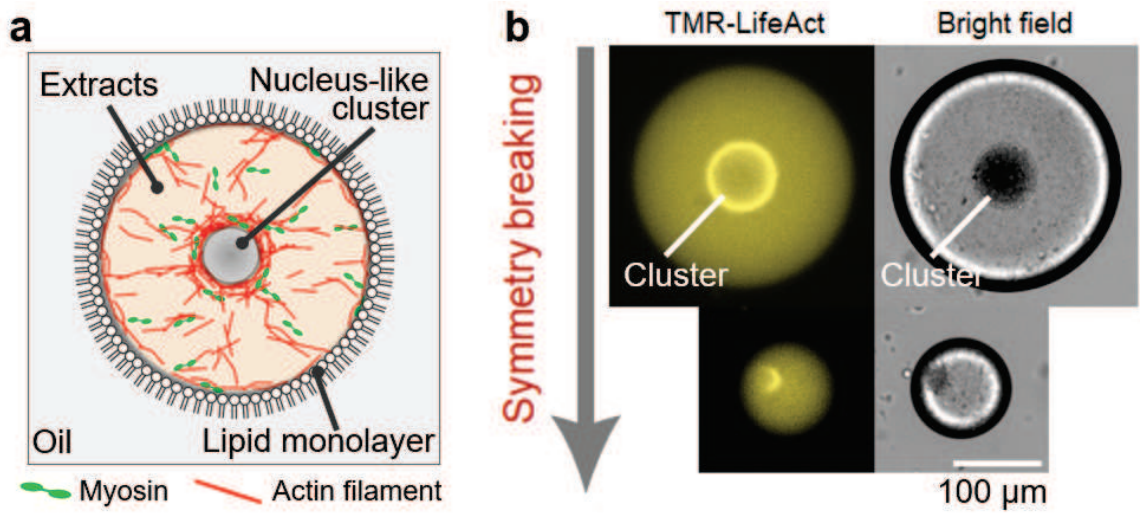
Figure 2.2: (**a**) Schematic showing the extracts-in-oil droplet. We regard the spherical aggregates of the debris of the organelles as the model of the cell nucleus. (**b**) The droplet size-dependent symmetry breaking of the cluster positioning. The cluster is located at the center in the large droplets, while it is located at the edge (close to the surface of the droplet) in the small droplets.

2.2 Materials and Methods

2.2.1 Experimental setup

Preparation of *Xenopus* egg extracts. Cytoplasmic extracts of *Xenopus* egg were prepared accordingly to the previous publication [16] (frozen extracts were gifted from Makito Miyazaki in Kyoto University and Yuta Shimamoto in National Institute of Genetics). The frozen extracts in $-80°$C are immediately thawed and incubated on ice for 1 hour, and then a microtubule polymerization inhibitor Nocodazole 0.2μL (f. 1mM) are added to the extracts and mixed by finger tapping. In addition, a marker tetramethylrhodamine(TMR)-Lifeact 0.2μL (f. 1mM) was added to the extracts. TMR-Lifeact is a small peptide only bound to the F-actin, not bound to the G-actin (monomer actin molecule), thus it is suited to the visualization of actomyosin networks. Moreover, due to its small peptide nature, it is known that the binding of TMR-Lifeact does not affect much on the dynamics of actomyosin networks [80, 81, 82].

Preparation of recombinant proteins.

- Recombinant proteins were gifted from Makito Miyazaki (Kyoto University). Briefly, the VCA domain of mouse WASP cDNA (384-501 aa) was cloned into pCold-I vector (Takara), expressed in *Escherichia coli* (*E. coli.*) (Rosetta(DE3), Merck Millipore) at 15°C for overnight in the presence of 1 mM IPTG. The ×6 histidine-tagged mutant was purified over a Ni Sepharose 6 Fast Flow column (GE healthcare), followed by dialysis against A50 buffer (50 mM HEPES-KOH pH 7.6, 50 mM KCl, 5 mM $MgCl_2$, 1 mM EGTA) containing 1 mM DTT at 4°C.

- Recombinant human α-actinin I (×6 histidine-tagged) was prepared in accordance with our previous study [111], except for digestion of the histidine-tag by

PreScission protease. Purified α-actinin was dialyzed overnight against A150 buffer (50 mM HEPES-KOH pH 7.6, 150 mM KCl, 5 mM $MgCl_2$, 1 mM EGTA) containing 1 mM 2-mercaptoethanol at 2°C.

- The severing activity of native gelsolin is regulated by Ca^{2+} [83]. In this study, we constructed a constitutively active form of gelsolin by deleting 23 amino acid residues from its C-terminus [83, 84]. Mouse gelsolin cDNA (1-779 aa) was cloned into pCold-I vector (Takara), expressed in *E. coli.* (Rosetta(DE3), Merck Millipore) at 15°C for 15 h without IPTG [85]. The gelsolin mutant ($\times$6 histidine-tagged) was purified over a Ni Sepharose 6 Fast Flow column (GE healthcare), followed by dialysis against A50 buffer containing 1 mM DTT at 4°C.

- The actin polymerization activity of native formins is regulated by the binding of Rho GTPases [86]. In this study, we constructed a constitutively active form of formin by deleting the auto-inhibitory domain [87, 88, 89]. FH1 and FH2 domains of mouse mDia2 cDNA (521-1020 aa) were cloned into pGEX-6P vector (GE Healthcare), expressed in *E. coli.* (Rosetta(DE3), Merck Millipore) at 16°C for 2.5 h in the presence of 1 mM IPTG. The GST-tagged mDia2 mutant was purified over a Glutathione Sepharose High Performance column (GSTrap HP, GE Healthcare), followed by dialysis against A50 buffer containing 1 mM DTT at 4°C.

- Protein concentrations were determined using the Protein Assay Kit (500-0006, Bio-Rad), and using molecular weights of 15,200 Da for his-tagged VCA, 105,300 Da for his-tagged α-actinin I, 80,100 Da for his-tagged gelsolin mutant, and 83,600 Da for GST-tagged mDia2 mutant. Proteins were snap-frozen in liquid nitrogen and stored at -84°C.

PDMS(polydimethylsiloxane) coating on glass cover slips   The observation chamber was made to fix the droplet to avoid its motion driven by the unexpected flow. To avoid the wetting of droplets onto the glass coverslip, the glass surfaces were coated by silicone elastomer based on polydimethylsiloxane (PDMS) (Sylgard, 184) using spin coater (MIKASA), which was cured for 1 hour at 70°C in an oven.

Preparation lipid-oil mixture.   Cytoplasmic extracts droplets must be surrounded by a lipid membrane to mimic the living cells. Here, eggPC (L-α-phosphatidylcholine from egg yolk; Nacalai Tesque) was used as a model cell membrane. The 1mM eggPC and mineral oil (M5904; Sigma Aldrich) was mixed in a 1.5 mL PCR tube, which was then sonicated (ASU-6, ASU Cleaner; AS ONE) at 60°C for 1.5 hours. The lipid-oil mixture was stored at -30°C.

Extracts-in-oil droplet preparation.   Extracts were kept on ice to avoid the progression of biochemical reactions. The pre-prepared eggPC-mineral oil mixture was also kept on ice. First, 3 μL of the extracts were added to the lipid-oil mixture, and the tube was immediately tapped by fingers to form extracts-in-oil droplets. To place the droplets onto an observation chamber, tip-cut 200 μL micropipettes were used to avoid shear stress-induced damage to the extracts. Extracts-in-oil droplets 10-35 μL were gently placed on a PDMS-coated glass coverslip, gently sealed by another glass coverslip. The chamber height was controlled by the double-sided tape ranging from 10, 30, 60, and 100 μm to obtain the droplets with aspect ratio within $0.3 < h/D < 0.6$. The observation chamber was also sealed by an epoxy-glue (Araldite) to avoid unexpected flows (Fig. 2.3).

Preparation of microfluidic chamber.   To make the microchamber with various shapes, a microfluidic device system was constructed (Fig. 2.4). All the following procedures must be performed in a clean room with efficient ventilation.
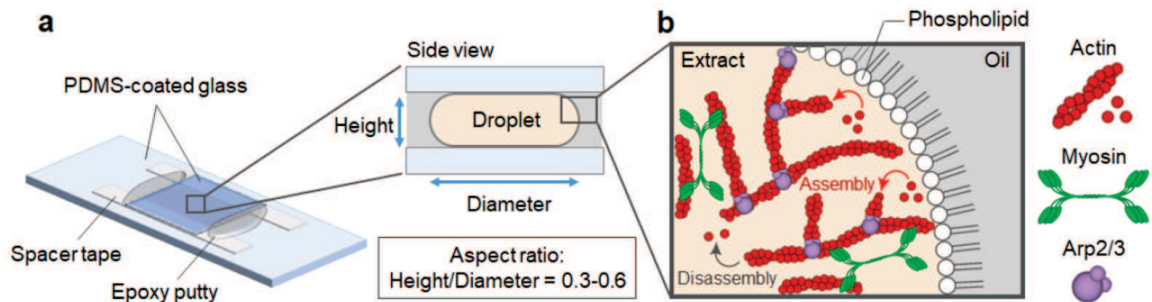
Figure 2.3: (**a**) Schematic of the experimental setup. The observation chamber was sealed by epoxy putty, and the height of the chamebr was controlled by the spacer tape, in which the droplet with aspect ratio within 0.3 < Height/Diameter < 0.6 was analyzed. (**b**) Zoom-in view showing F-actin polymerized by Arp2/3 and F-actin depolymerization. The myosin mini-filaments induce contractile forces.

Step I: Spin coating of SU-8 photoresist on a silicon wafer

1. Heat the silicon wafer at 200°C for 5 min to clean the surface

2. Place the silicon wafer on the spin coater (MIKASA)

3. Put 2mL SU-8 3025 on the center of the silicon wafer

4. The SU-8 solution is extended over the silicon wafer using spin coater at 2000 rpm for 50 s

5. Put the silicon wafer at 95°C for 5 min (This process is hereafter called 'soft bake', which will make the surface smooth)

6. Cool down the wafer at R.T. for 5 min

Step II: UV-light exposure

1. Ready for the UV-lamp (Nikon) and wait for 5 min to stabilize

2. Put the patterned chromium-photomask on the SU-8 coated silicon wafer

3. Irradiate the UV-light for 20 s

4. Remove the photomask from the silicon wafer and soft bake it at 95°C for 5 min

5. Cool down the wafer at R.T. for 5 min

6. Clean the surface of the photomask using Acetone

Step III: SU-8 development

1. Prepare the 30 mL of SU-8 developer solution in a glass vial. The glass vial must be closed during SU-8 development

2. Put the silicon wafer prepared at Step II into the SU-8 developer to dissolve the non-irradiated region of the SU-8 photoresist

3. Rotate the glass vial using a rotator for 10 min

4. When all the non-irradiated regions are dissolved, take away the silicon wafer and splay the Ethanol to the surface of the silicon wafer to remove the SU-8 developer

5. Put the silicon wafer in MilliQ to remove the ethanol

6. Heat the silicon wafer at 200°C for 15 min

7. Heat the silicon wafer at 95°C for 1 hr. This is the end of the patterned mold preparation

Step IV: Preparation of PDMS microchamber

1. Mix the PDMS elastomer with curing agent at ratio 9:1. Incubate the solution in the fridge for more than 6 hrs to remove the bubbles

2. The PDMS elastomer was poured on the mold and coated at 300 rpm for 20 sec, then cured at 75°C for 1 hr

3. Cutout the PDMS sheet from the patterned silicon wafer using a scalpel

4. The depth of the microchambers were determined by a laser scanning surface profiler (LT-9000; Keyence)

Step V: Preparation of the observation chamber

1. PDMS sheet was gently placed on a plasma-treated glass slide, heated at 75°C for 1 hr

2. Afterwards, a flow chamber was constructed on top of the PDMS sheet with a coverslip and 300 μm thick double-sided tape

3. PEG-PLL solution was supplemented to the chamber and incubated for 3 hrs in a fridge, which increases the hydrophilicity and prevents non-specific adhesion of proteins

4. PEG-PLL solution was then dried using an air duster, then the extracts were injected into the flow chamber. Subsequently, mineral oil with 0.5% Cithrol (w/v) was injected into the chamber to cover the micro-patterns with the monolayer of Cithrol

5. Finally, the flow chamber was sealed by epoxy glue to stop drift flow.

Procedures 4-5 were performed on ice to avoid actomyosin contraction.
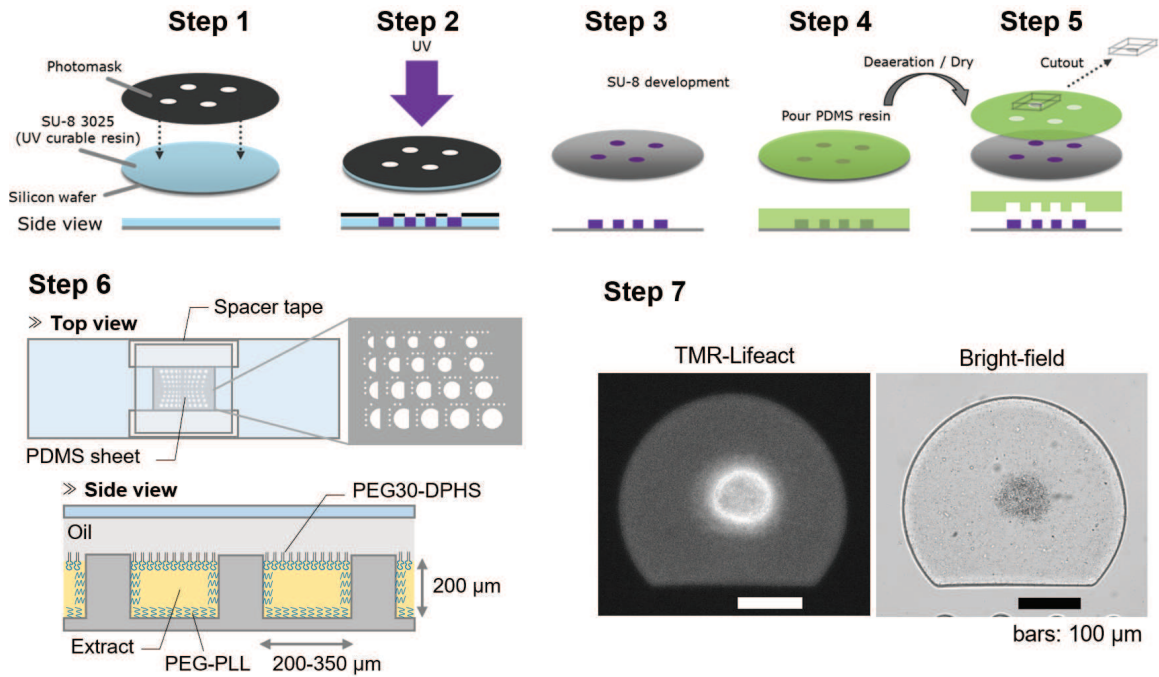
Figure 2.4: Preparation procedure of the mold and PDMS microchamber. (**Step 1**) Pour the SU-8 UV curable resin onto the silicon wafer and spread it over the surface using a spin coater. (**Step 2**) Iraddiate the UV-light through the patterned chromium-photomask. (**Step 3**) Wash out the uncured SU-8 using developer solution. (**Step 4**) Pour the PDMS elastomer solution on the mold and heat it for 1 hr for curing. (**Step 5**) Cutout the cured PDMS device from the mold. (**Step 6**) Construct a observation flow chamber. (**Step 7**) Observation of the actomyosin dynamics in a microchamber with defined shapes.

2.2.2 Image analysis

Imaging. Time-lapse images were acquired every 3s using an epi-fluorescence microscope (IX73, Olympus) equipped with ×20 objective lens (TU Plan ELWD ×20/0.40, Nikon) or ×50 objective lens (TU Plan ELWD ×50/0.60, Nikon), a cooled CMOS camera (Neo5.5, Andor Technology), and a stable excitation light source (XLED1, Lumen Dynamics). Confocal images were acquired using an inverted microscope (IX73, Olympus) equipped with ×40 objective lens (UPlanFL ×40/1.30 Oil, Olympus), a confocal scanner unit (CSU-X1, Yokogawa), 561 nm laser (50mW; OBIS, Coherent), and EM-CCD camera (iXon3, Andor Technology). The laser ablation experiments

were performed by using a UV pulse laser (Explorer One 349 nm, Spectra-Physics), equipped with the spinning-disk confocal microscope. For all microscopic examinations, the sample temperature was maintained at $20 \pm 1°$C, using a homemade heat block connected to a water bath circulator.

Quantification of droplet and cluster diameter. Quantitative image analysis was performed using a custom code written in MATLAB. The center of mass of each droplet and cluster was detected through binarization of bright field images (Fig. 2.5). To determine the radius R_{droplet} of droplets, the area of each droplet was extracted and then assumed to be equal to πR_{droplet}^2. The radius of clusters was derived in the same manner. The contraction velocity of actomyosin waves and the wave period was quantified by producing kymographs from fluorescence images along the droplet diameter.
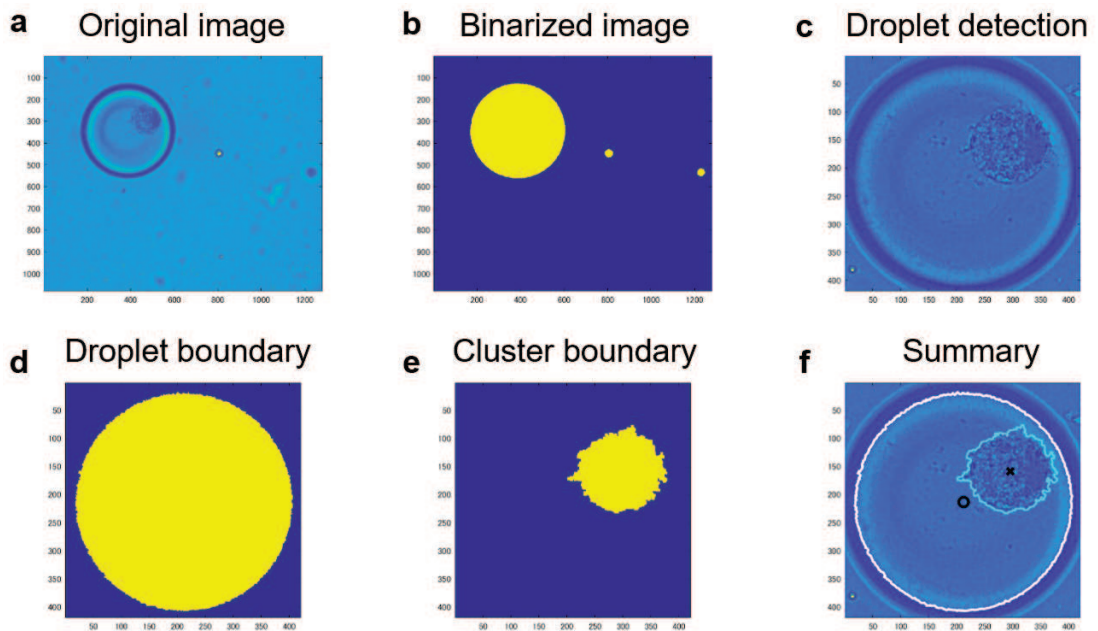
Figure 2.5: (**a**) An original image taken by bright field microscopy. (**b**) The binalized image of (a). (**c**) The droplet is automatically detected and focused. (**d**) The image (c) is binarized and the outline of the droplet is detected. (**e**) The image (c) is binarized and the outline of the cluster is detected. (**f**) Both the droplet boundary and the cluster boundary is super-imposed on the original image (a), where the 'o' and '×' represent the centroid of the droplet and the cluster, respectively.

Quantification of F-actin length distribution. The length distribution of the F-actin was also quantified through the image analysis. The extracts were incubated at 20°C for 1 hour. Then, the extracts were diluted 20× by a high salt buffer (20 mM Tris-HCl pH 7.4, 0.6 M KCl, 1 mM DTT) containing 0.5 μM rhodamine-phalloidin, to dissociate actin crosslinkers from actin bundles and stabilize the filaments53. The solution was further diluted by the high salt buffer to lower the filament density and perfused into NEM-HMM-coated flow chamber to fix actin filaments on the glass surface, then the images were taken by epifluorescence microscopy equipped with ×100 objective lens (PlanApo ×100/1.40 Oil, Olympus) and EM-CCD camera (iXon3, Andor Technology). The filament length was measured by a custom code written in MATLAB. First, the fluorescence images of F-actin were binarized. Then, only skinny and unbranched filaments (eccentricity > 0.9) and those with reasonable sizes (area < 1300 pixels) were selected. Finally, the filaments were converted into one-pixel-wide sticks, by which the area of sticks was equal to the filament length.

2.3 Results

2.3.1 Experiment I: Cluster formation

A few tens of seconds after the confinement, initially polymerized bulk actomyosin networks started to contract, forming a spherical cluster (Fig. 2.6a). We regard this cluster as a model of a cell nucleus and studied how the positioning of the cluster is determined. We confirmed that the cluster is mainly composed of the crushed organelles using lipid-binding fluorescent marker R18 (Fig. 2.6b). The cluster size was linearly scaled with the droplet size because the cluster is composed of the debris of crushed organelles during extract preparation and that amount is proportional to the size of the droplet (Fig. 2.6c). To avoid the cluster motion being interrupted by the top and bottom substrates, we only analyzed the droplets with aspect ratio within $0.3 < h/D < 0.6$.
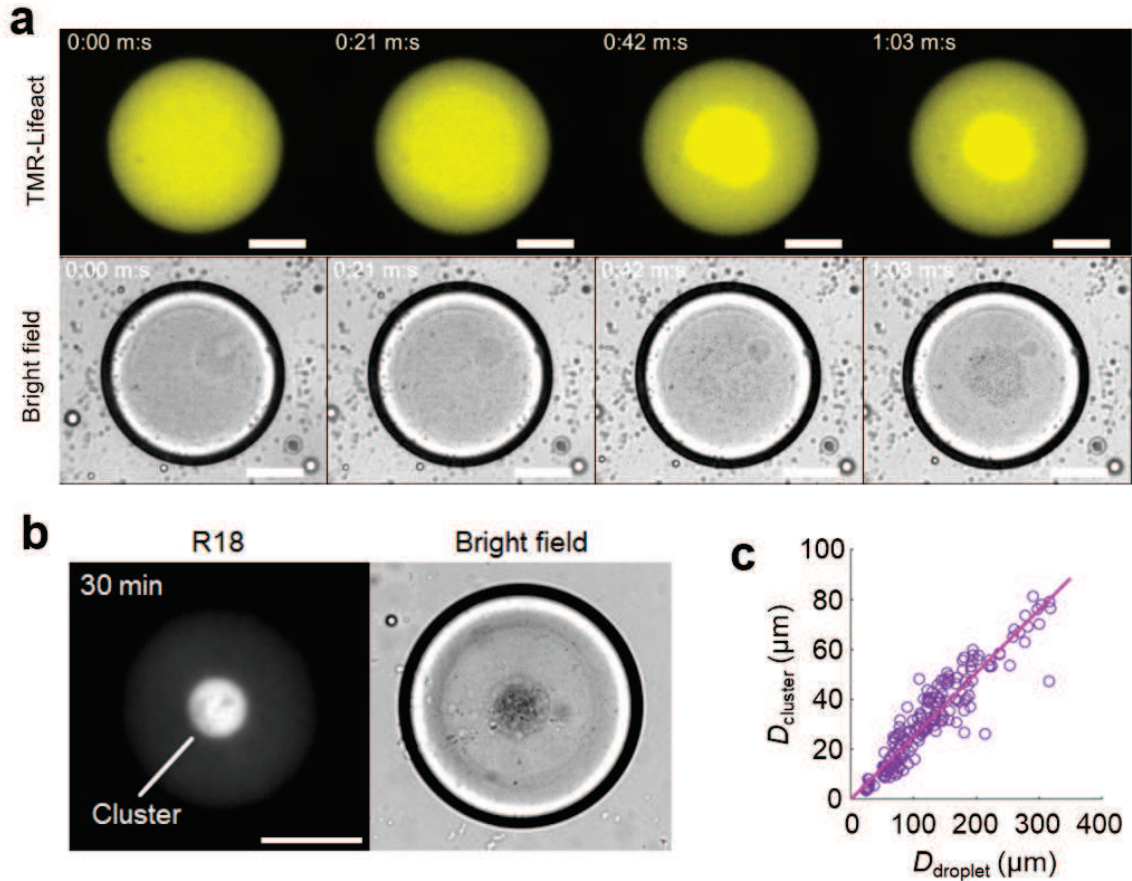
Figure 2.6: (**a**) Time-lapse images of the contracting actomyosin network. F-actin is visualized by TMR-Lifeact. The minutes and seconds are represented as 'm:s'. (**b**) The cluster is fluorecently labeled by R18 (lipid binding fluorescent marker). (**c**) The cluster diameter D_{cluster} dependence on the droplet diameter D_{droplet}. All images were taken by epi-fluorecence microscopy. Scale bars, 100 μm.

2.3.2 Experiment II: Periodic actomyosin wave

Immediately after the cluster formation, ring-shaped actomyosin networks were periodically generated from the droplet periphery, which was propagated toward the center (Fig. 2.7a). By making the kymograph from the time-lapse images (Fig. 2.7b), we found that the wave velocity was linearly scaled with the droplet diameter D_{droplet} (Fig. 2.7c), while the wave period was not strongly dependent on the droplet diameter (Fig. 2.7d).

To understand molecular determinants of the periodic wave generation, we per-
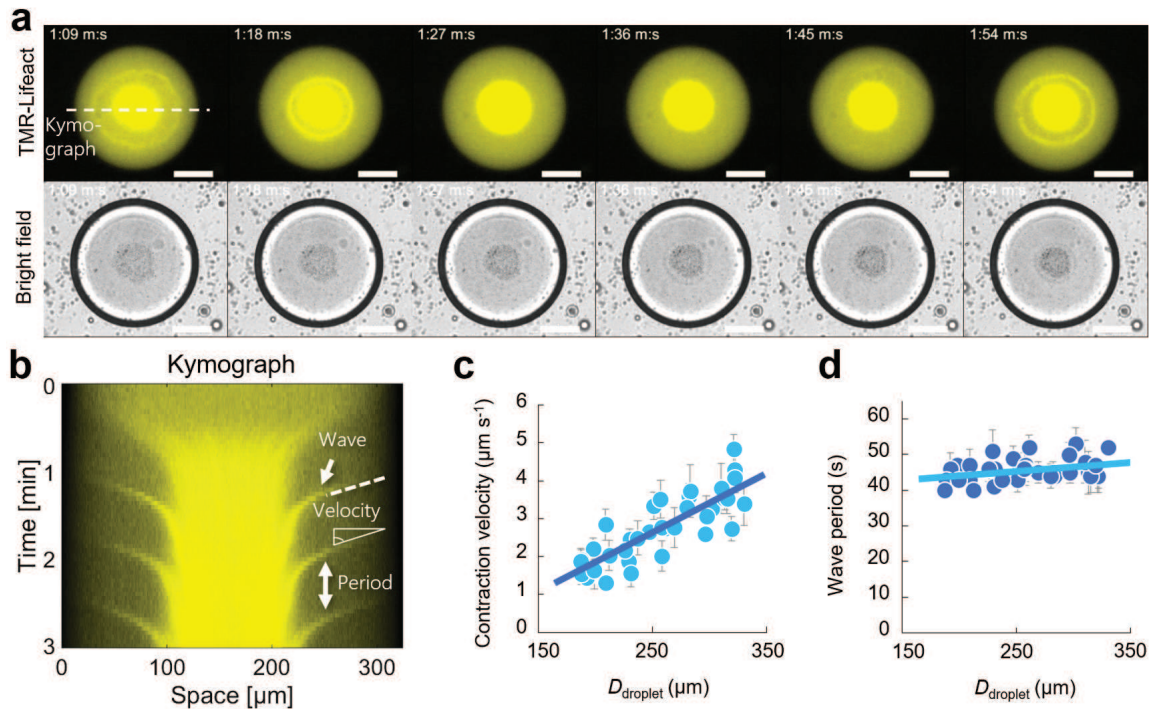
Figure 2.7: (**a**) Time-lapse images of the periodic actin wave generation. (**b**) Kymograph of the periodic actin wave measured along the white broken line spans over the droplet diameter in (a). The contraction velocity and the period were measured from the kymograph as indicated by white lines and arrows. (**c**) Contraction velocity of actin wave dependence on the droplet diameter. (**d**) Period of actin wave dependence on the droplet diameter. Error bars represent SD from the mean velocity averaged over three successive waves. All images were taken by epi-fluorescence microscopy. Scale bars, 100 μm.

formed molecular perturbation experiments. First, to see if myosin contractility is involved in the wave propagation, calyculin A (increase the number of active myosin by inhibiting the phosphatase; i.e., increasing the contractility) (Fig. 2.8b) and Y27632 (decrease the number of active myosin by inhibiting the ROCK activity; i.e., decreasing the contractility) (Fig. 2.8c) were added to the extracts. The activation of myosin contractility accelerated the contraction speed, whereas the inactivation of myosin contractility slowed down the contraction speed (Fig. 2.9c,d). Moreover, by further adding the 1 mM Y27632, the wave generation was stopped (Fig. 2.8d). These results suggest that myosin contractility is crucial for wave propagation. On the other hand, the addition of CK666 (Fig. 2.8a), which slows down the F-actin polymeriza-

tion by inhibiting the Arp2/3 complex that nucleates branched F-actin, increased the wave period (Fig. 2.9a,b). This suggests that the F-actin polymerization via Arp2/3 is involved in the periodic generation of the actomyosin wave. Indeed, complete inhibition of F-actin polymerization by the addition of cytochalasin D eliminates the wave generation (Fig. 2.10a). To further understand the role of F-actin turnover in the periodic generation of actomyosin waves, we added Phalloidin which stabilizes the F-actin and inhibits the depolymerization of F-actin into monomer G-actin, thus the G-actin pool would be used out. Indeed, the periodic wave was stopped after several waves, showing that the continuous F-actin depolymerization is also important to maintain the periodic wave generation (Fig. 2.10b).

To summarize, these results show that (i) contractility of myosin is necessary for actomyosin wave propagation, and (ii) continuous recycling of F-actin through polymerization and depolymerization (i.e., turnover) is necessary for the periodic wave generation. These features of periodic wave generation are used to construct the theoretical model of the actomyosin wave.
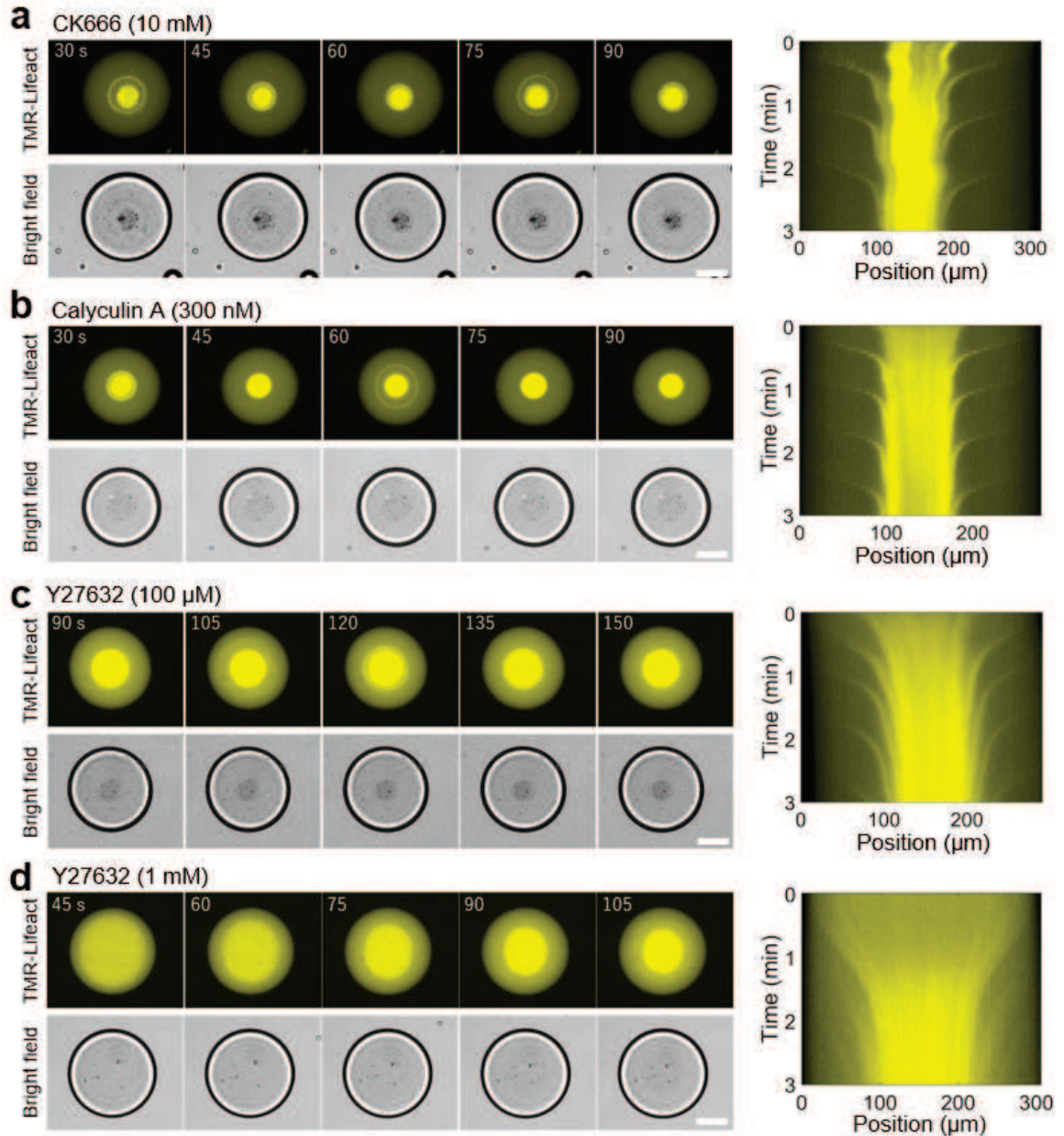
Figure 2.8: Time-lapse images (left) and kymographs (right) under several molecular perturbations. Clusters were formed at 0 s. (**a**) CK666 (10 mM) inhibits actin nucleation activity of Arp2/3 complex, thus the wave period is extented. (**b**) Calyculin A (300 nM) activates myosin motor by inhibiting the phosphatases of myosin regulatory light chain, thus the contraction velocity was increased. (**c**) Y27632 (100 μM) inhibits myosin motor activity by inhibiting phosphorylation of myosin regulatory light chain by ROCK, thus the contraction velocity was decreased. (**d**) By adding the larger amount of Y27632 (1 mM), initial cluster formation was significantly decelerated and actin wave disappeared. All images were taken by epi-fluorescene microscopy. Scale bars, 100 μm.
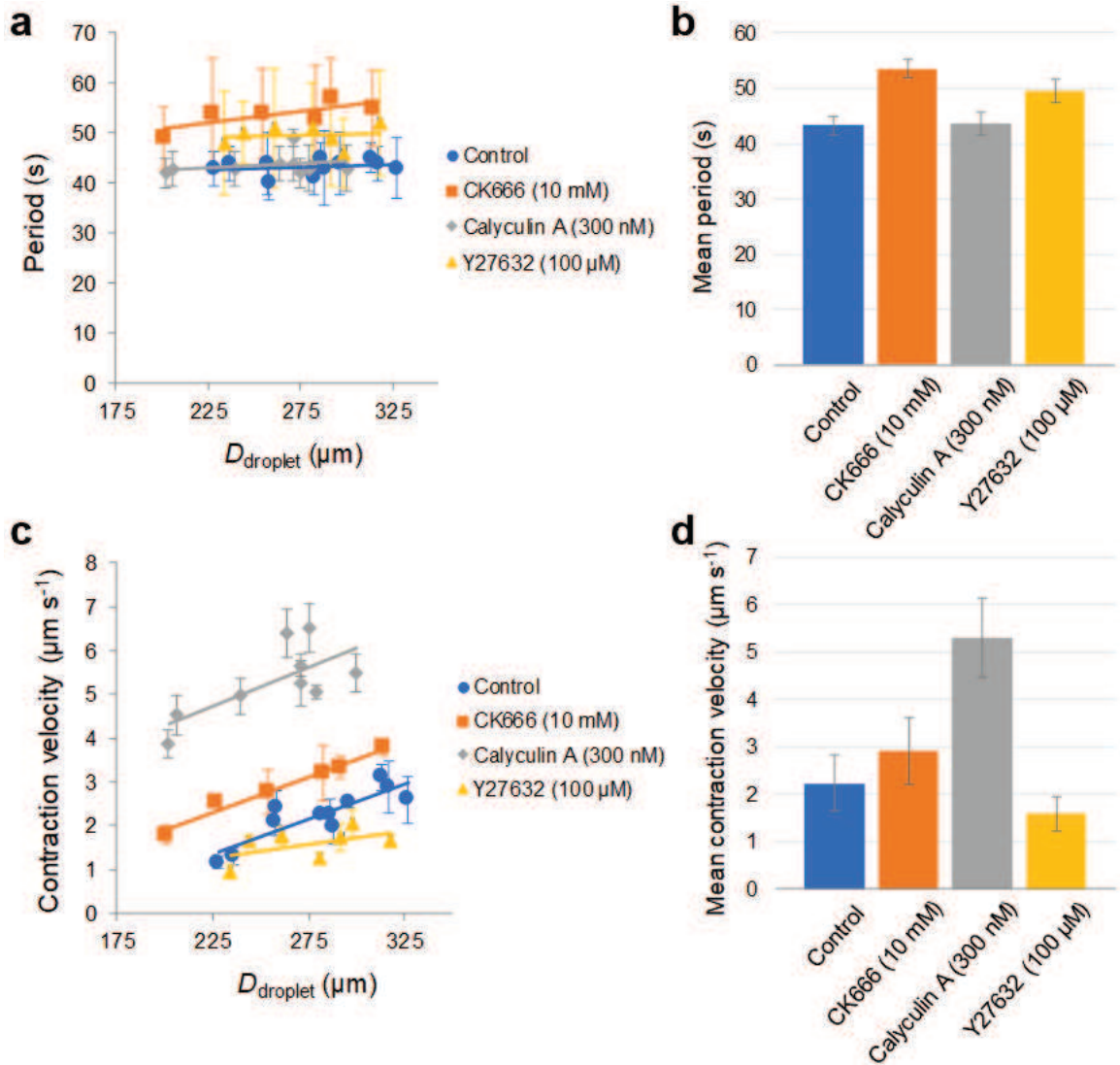
Figure 2.9: (**a**) The wave period dependence on the droplet diameter under several molecular perturbations. The wave period T was fitted by $T = 1.2 \times 10^{-2} D_{\text{droplet}} + 40$ (Control), $T = 4.7 \times 10^{-2} D_{\text{droplet}} + 41$ (CK666 10 mM), $T = 1.6 \times 10^{-2} D_{\text{droplet}} + 40$ (Calyculin A 300 nM), $T = 0.94 \times 10^{-2} D_{\text{droplet}} + 47$ (Y27632 100 μM). Error bars represent SD from the mean velocity averaged over three successive waves. (**b**) The mean wave period averaged over all data points shown in (a). Error bars represent SD. (**c**) The wave contraction velocity dependence on the droplet diameter under several molecular perturbations. The wave contraction velocity v was fitted by $v = 1.6 \times 10^{-2} D_{\text{droplet}} - 2.2$ (Control), $v = 1.6 \times 10^{-2} D_{\text{droplet}} - 1.3$ (CK666 10 mM), $v = 1.8 \times 10^{-2} D_{\text{droplet}} + 0.75$ (Calyculin A 300 nM), $v = 0.63 \times 10^{-2} D_{\text{droplet}} - 0.16$ (Y27632 100 μM). Error bars represent SD from the mean velocity averaged over three successive waves. (**d**) The mean wave contraction velocity averaged over all data points shown in (a). Error bars represent SD.

Figure 2.10: (**a**) Addition of cytochalasin D (200 μM), the actin polymerization inhibitor, eliminated cluster formation and actin wave generation. (**b**) Addition of phalloidin (10 μM), the actin depolymerization inhibitor, eliminated actin wave generation after two wave propagations. Actin polymerization was initiated at 0 s. All images were taken by epi-fluorescence microscopy. Scale bars, 100 μm.
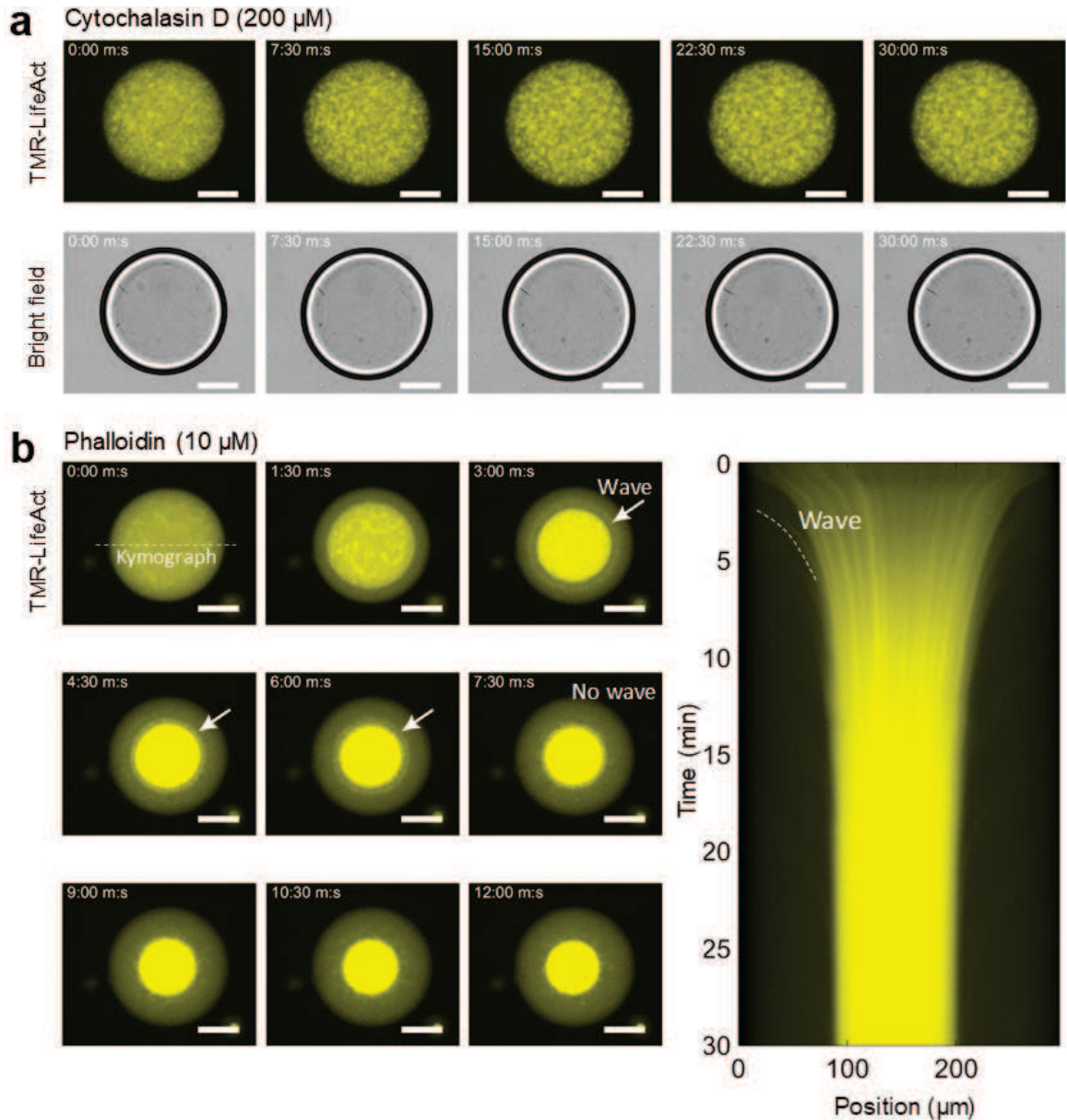
2.3.3 Theory I: Active gel model of actomyosin wave

To further understand how the actomyosin wave is generated and contract, we analyzed the theoretical model of actomyosin wave. Here, we used the two-fluid model based active gel theory [38, 39]. The contitutive equation can be written as

$$\gamma\left(\frac{\partial \mathbf{u}}{\partial t} - \mathbf{v}\right) = \nabla \cdot \boldsymbol{\sigma} + \frac{\mathbf{f}_{\text{ext}}}{d}, \tag{2.1}$$

where $\mathbf{u}$ is the displacement of the gel, $\mathbf{v}$ is the velocity of surrounding cytoplasm, γ is the friction coefficient between the cytoplasm and the gel, $\boldsymbol{\sigma}$ is the stress tensor of the gel, $\mathbf{f}_{\text{ext}}$ is the external force applied to the gel, and d is the thickness of the ring. The stress tensor is composed of the passve elastic stress σ_{ij}^{el} originated from the F-actin network and the active stress σ_{ij}^{act} originated from the myosin contractility $\sigma_{ij} = \sigma_{ij}^{\text{el}} + \sigma_{ij}^{\text{act}}$. The passive stress can be written as

$$\sigma_{ij}^{\text{el}} = \left(\lambda + \frac{2}{3}\right)\delta_{ij}\nabla \cdot \mathbf{u} + 2\mu\left(u_{ij} - \frac{1}{3}\delta_{ij}\nabla \cdot \mathbf{u}\right), \tag{2.2}$$

where λ and μ is the Lame coefficient of the linear elastic theory, δ_{ij} is the Clonecker's delta, and $u_{ij} = (\partial_i u_j + \partial_j u_i)/2$. The contribution of the viscous dissipation of the actomyosin networks are assumed to be neglected compared to the friction γ between two fluids at the scale larger than the mesh size if F-actin network ($\sim$10 nm) [38, 39]. On the other hand, active stress is given by

$$\sigma_{ij}^{\text{act}} = \zeta(c_{\text{b}})\Delta\mu\delta_{ij}, \tag{2.3}$$

where $\Delta\mu$ is the free energy difference due to the hydration of ATP (Adenosin Triphosphate) to generate myosin motor contractility, and $\zeta(c_b)$ is the proportionality coefficient, where active stress is assumed to be proportional to the concentration of myosin motor bound to the F-actin, c_b, thus $\zeta(c_b) = \zeta_0 c_{\text{b}}$ (ζ_0 is the proportionality constant).

First, we consider the period of the actomyosin wave. Let t_0 be the duration that the F-actin is polymerized and formed a ring dense enough to transmit contractility of bound myosin (Fig. 2.11a,b). By taking the center of the droplet as the origin of the circular coordinate, given that the ring with the radius r thickness d, its constitutive equation along the radial direction is written as

$$\gamma \frac{\partial u_r}{\partial t} = B \frac{\partial}{\partial r} \left[\frac{\partial u_r}{\partial r} + \frac{u_r}{r} \right] - \frac{\zeta_0 \Delta \mu c_\mathrm{b}}{r} + \frac{f_\mathrm{wall}}{d}, \tag{2.4}$$

where $B = \lambda + 2\mu$, and the flow induced by the gel's motion was assumed to be negligible when the newly polymerized F-actin network is not too dense $\mathbf{v} \simeq 0$ [38, 39]. In addition, f_wall is the the counter acting force against the contraction of the gel when the F-actin is bound to the surface of the droplet (Fig. 2.11a). Because the gel bound to the droplet surface with radius R is not moving, substituting $r = R$, $u_r = \partial_t u_r = 0$ to Eq. (2.4) and the stress acting on the wall is given by

$$f_\mathrm{wall} = \frac{\zeta_0 \Delta \mu c_\mathrm{b} d}{R}. \tag{2.5}$$

The density of myosin bound to the F-actin is assumed to linearly increase in time, $c_\mathrm{b} = \alpha(t - t_0)$ (α is the proportionality constant) [20]. Given that it takes a period T to break the bond between the ring and the droplet periphery, the wave period is given by

$$T(R) = t_0 + \frac{f_\mathrm{th}}{\zeta_0 \Delta \mu \alpha d} R. \tag{2.6}$$

where f_th is the threshold stress to break the bond between the ring and the wall (Fig. 2.11a). Note that the linear dependence of the period on the droplet diameter is observed in the experiment (Fig. 2.7d). The weak droplet size dependence of the wave period can be interpreted as the weak binding between F-actin and the membrane. In addition, numerical calculation of Eq. (2.4) well reproduces the experimentally

observed wave propagation profile (Fig. 2.11c-e). Together, these results suggest that the periodic actomyosin wave is generated at the periphery due to the polymerization of ring-like actomyosin networks, and that produces inward contractile force that transports the cluster to the center.
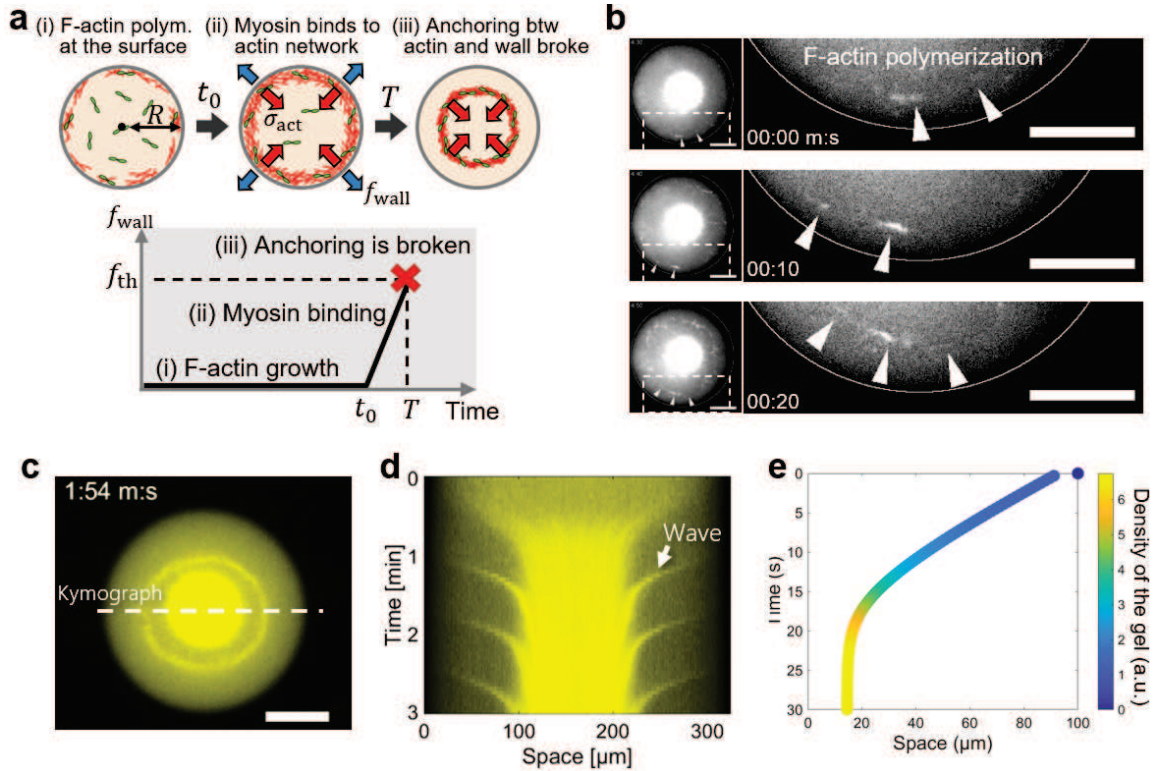
Figure 2.11: (**a**) The model of periodic actin wave generation. (i) First, F-actin is polymerized at the periphery of the droplet. (ii) The myosin motor can effectively generate contractile stress σ_{act} when the F-actin network is sufficiently grown and crosslinked each other after time t_0 passed. At the same time, due to the anchoring between F-actin network and the droplet surface, the counter-actin force f_{wall} is balanced with σ_{act}. (iii) Finally, at time T (the wave period), the grown actin wave starts to propagate when the contractile stress σ_{act} exceeds the threshold value f_{th} and broke the anchoring. (**b**) Time-lapse images of the growing F-actin network beneath the droplet surface. (**c**) A snapshot of ring-like actin wave. (**d**) The kymograph of wave propagation extracted from the white broken line in (c). (**e**) Numerically caluculated wave propagation profile of Eq. (2.4). We used the the parameters same as [64], such that $\gamma = 1.5 \times 10^{-4}$ Pa s μm^{-2}, $\lambda = 0.05$ Pa, $\mu = 0.05$ Pa, $\zeta_0 \Delta\mu = -0.18$ Pa. Images in (b) were taken by confocal microscopy, and images in (c) were taken by epi-fluorescence microscopy. Scale bars, 100 μm.

2.3.4 Experiment III: Symmetry breaking of the cluster positioning

Actomyosin waves generate inward contractile force to move the cluster to the center. On the other hand, we found that the cluster is located at the edge in the smaller droplets (Fig. 2.12a). To quantitatively examine the cluster positioning, we defined the DC-ratio, which is the distance between the droplet center and the cluster normalized by the droplet radius, thus it takes the value between $0 <$ DC-ratio < 1 (Fig. 2.12b). After the initial cluster formation, the cluster position was gradually changed from either the edge toward the center (Fig. 2.12c-e) or from the center toward the edge (Fig. 2.12f-h), thereafter cluster positions were stabilized approximately after 30 min. By plotting the final stabilized DC-ratio along the droplet size, strikingly, cluster position sharply become asymmetric around the $D_{\text{droplet}} \sim 80$ μm as the droplet size decreases (Fig. 2.13a-c). Although there is an inwardly acting force on the cluster by the periodic actomyosin waves, how can the positioning symmetry be broken?
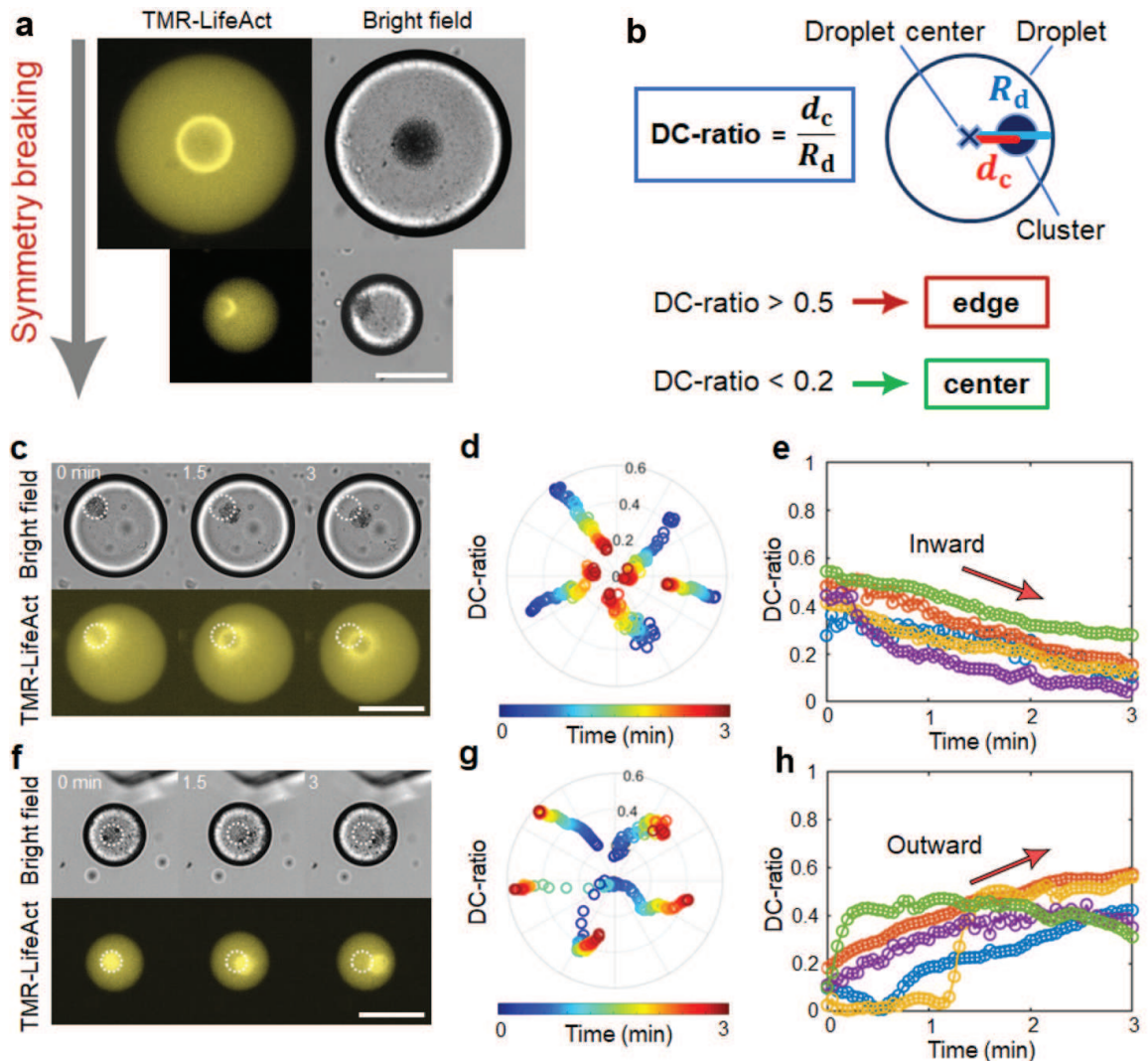
Figure 2.12: (**a**) Representative examples of the droplet size dependence of the cluster positioning. The stable position of the cluster became off-centered in small droplets. Images were acquired 1 h after encapsulation. (**b**) The polarity parameter DC-ratio is defined as the distance between the droplet center to the cluster centroid, d_c, divided by the radius of the droplet, R_d. DC-ratio is classified into two distinct regimes: larger than 0.5 is the 'edge' and smaller than 0.2 is the 'center'. (**c-e**) Typical examples of the inwardly directed motion of the clusters. (**f-h**) Typical examples of the outwardly directed motion of the clusters. The time point at which clusters started to move (typically ~1 min after the cluster formation) is defined as 0 min. All images were taken by epifluorescence microscopy. Scale bars, 100 μm.
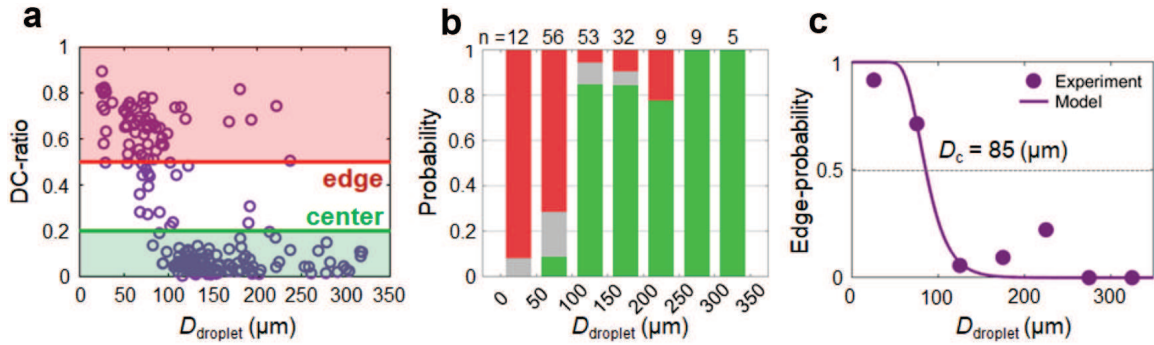
Figure 2.13: (**a**) Droplet diameter dependence of DC-ratio. We analyzed the stabilized cluster position more than 1 h after encapsulation. (**b**) Histogram of DC-ratio for each 50 μm bins calculated from (a). DC-ratio > 0.5, $0.5 \geq$ DC-ratio ≥ 0.2, and $0.2 >$ DC-ratio are colored in red, gray, and green, respectively. The top 'n=' describe the number of droplets included in each bar. (**c**) Edge-positioned probability extracted from (b) (red-colored bars). Filled circles and the solid curve represent experimental values and model fitting of Eq. (2.7), respectively. Experimental data were fitted by Eq. (2.7) using $L = 6.1$ μm and $\tau = 0.46$ s. Transition diameter $D_c = 85$ μm at which edge-probability becomes 0.5 was estimated from the fitting curve. Scale bars, 100 μm.

2.3.5 Experiment IV: F-actin bridge formation

To see how the cluster is moved to the edge, we next focused on the dynamic behavior of the actin network. Notably, we found that the bundle-like structure was connecting the cluster and the droplet when the cluster was oscillating, where the inward movement was induced by wave, thereafter the cluster was outwardly contracted (Fig. 2.14a-c). We visualized that F-actin bridge using high-resolution confocal microscopy. Here, we used laser ablation to directly evaluate the contribution of F-actin on the outward cluster motion (Fig. 2.14d). Indeed, by cutting the bridge, the cluster was slightly moved toward the center, and in turn, the bridge was reformed between the cluster and the droplet periphery, by which the cluster was contracted toward the edge again. These results indicate that the cluster is contracted toward the edge when the cluster is got connected to the droplet surface via the bridge-like actomyosin structure.
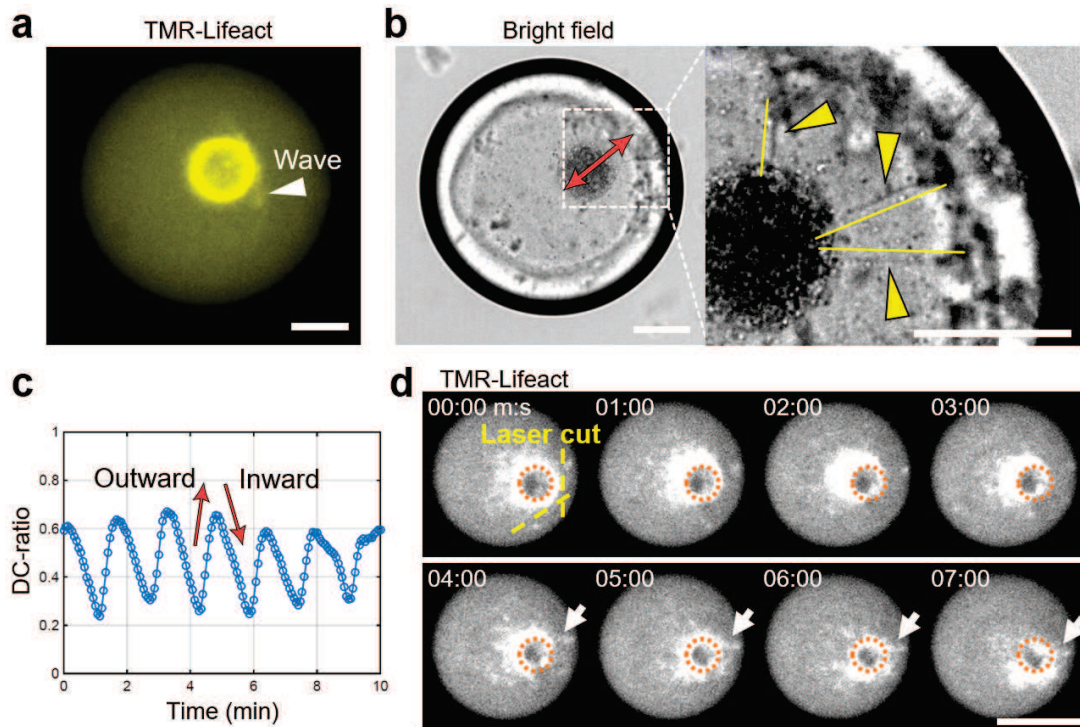
Figure 2.14: (**a**) Snapshot showing the actin wave pushing the cluster toward the center of the droplet. (**b**) The oscillating cluster is indicated by the red arrow. Zoom-in view shows the bundle-like structures connecting the cluster and the inner droplet surface. (**c**) The time dependence of the DC-ratio shows the cluster oscillation calculated from the bright-field image in (b). (**d**) Laser ablation was performed at the actin bridge connecting the cluster and the inner droplet surface. The cluster was slightly moved inward immediately after the laser-cut, whereas the cluster was contracted again toward the droplet surface when the actin bridge was reformed. The actin bridge is indicated by the white arrow. Images in (a) and (b) were taken by epi-fluorescence microscopy, and images in (d) were taken by confocal microscopy. Scale bars, 50 μm.

2.3.6 Experiment V: The physical role of droplet surface property on the cluster positioning

To give further insights into the relation between F-actin bridge formation and the cluster positioning, we changed the droplet surface property (Fig. 2.15a). We reasoned that when the cluster is contracted to the edge, the bridge must be connected to the droplet surface. If so, by decreasing the actin-membrane binding, or by increasing the actin-membrane binding, we could modulate the force generation of the actomyosin bridge, in turn, the cluster positioning would be affected. In fact, on the one hand, the larger number of clusters were located at the center when we added the PEG30-DPHS that prevents F-actin binding to the droplet surface (Fig. 2.15b, top). On the other hand, the number of edge-positioned clusters was significantly increased when we added the His-VCA+NiNTA-lipids that enhance the binding of F-actin at the droplet surface (Fig. 2.15b, bottom). Taken together, these results suggest that the cluster is transported toward the edge by the actomyosin bridge and the positioning symmetry is broken.
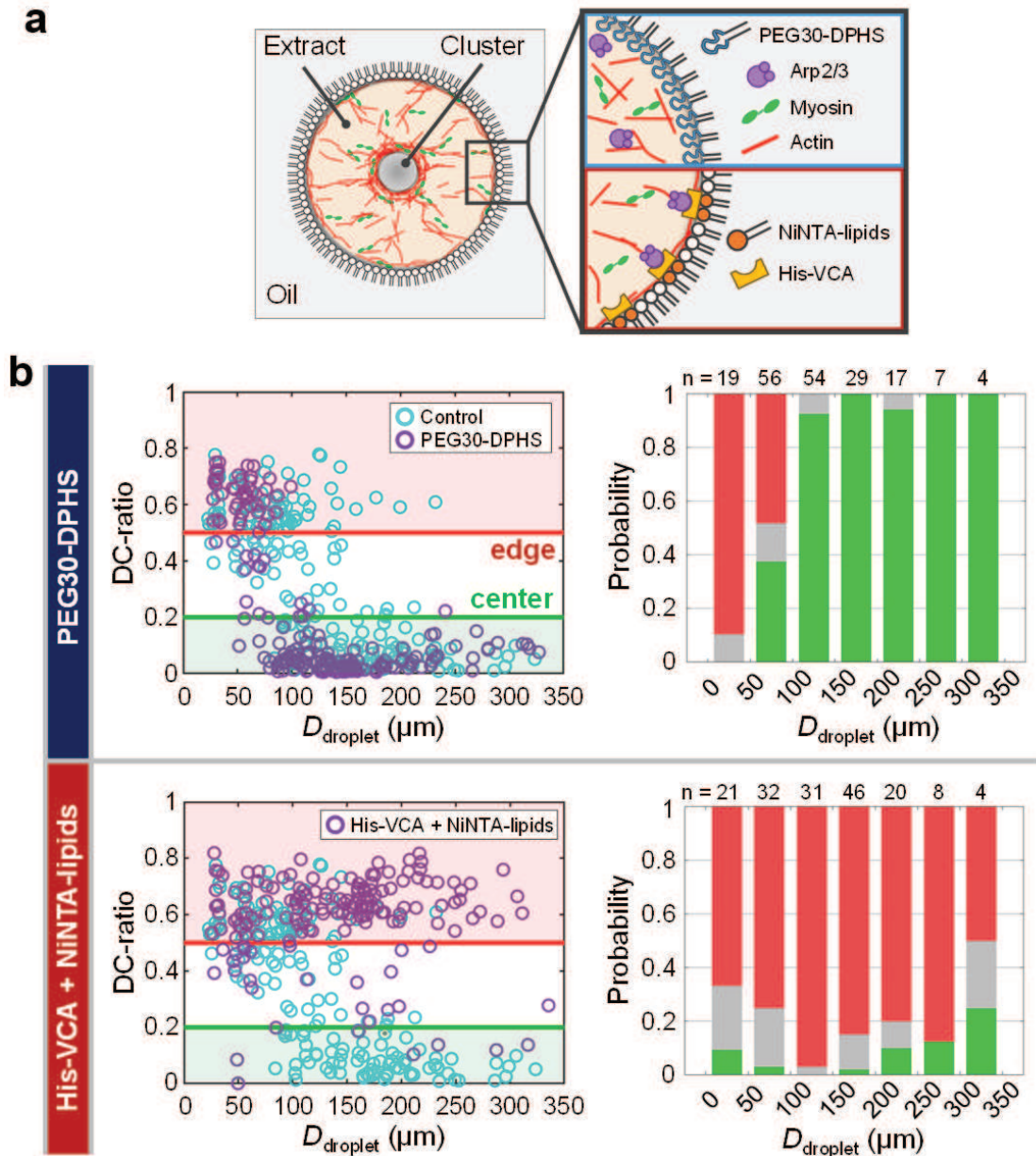
Figure 2.15: (**a**) Schematic illustration showing modulation of the surface property of the droplet. (top) PEG30-DPHS, a polyethylene glycol (PEG)-based surfactant, decreases adhesions of bulk actomyosin networks with the droplet surface. (bottom) The VCA domain of WASP conjugated with a histidine-tag was anchored to the droplet boundary via Ni-NTA conjugated lipids. VCA activates the local actin nucleation activity by recruiting Arp2/3, thereby the binding of bulk actomyosin networks with the droplet surface is enhanced. (**b**) The droplet diameter dependence of the DC-ratio. Cyan circles represent the control data (egg PC). (top) Passivated droplet surface promoted the cluster centering, whereas (bottom) activated droplet surface promoted the edge positioning. Kolmogorov-Smirnov test was applied to the scatter plots of DC-ratio between $50 < D_{\text{droplet}} < 150$ (around the transition point in the control experiment), where the distributions were significantly different from the control in both conditions ($p < 0.001$).
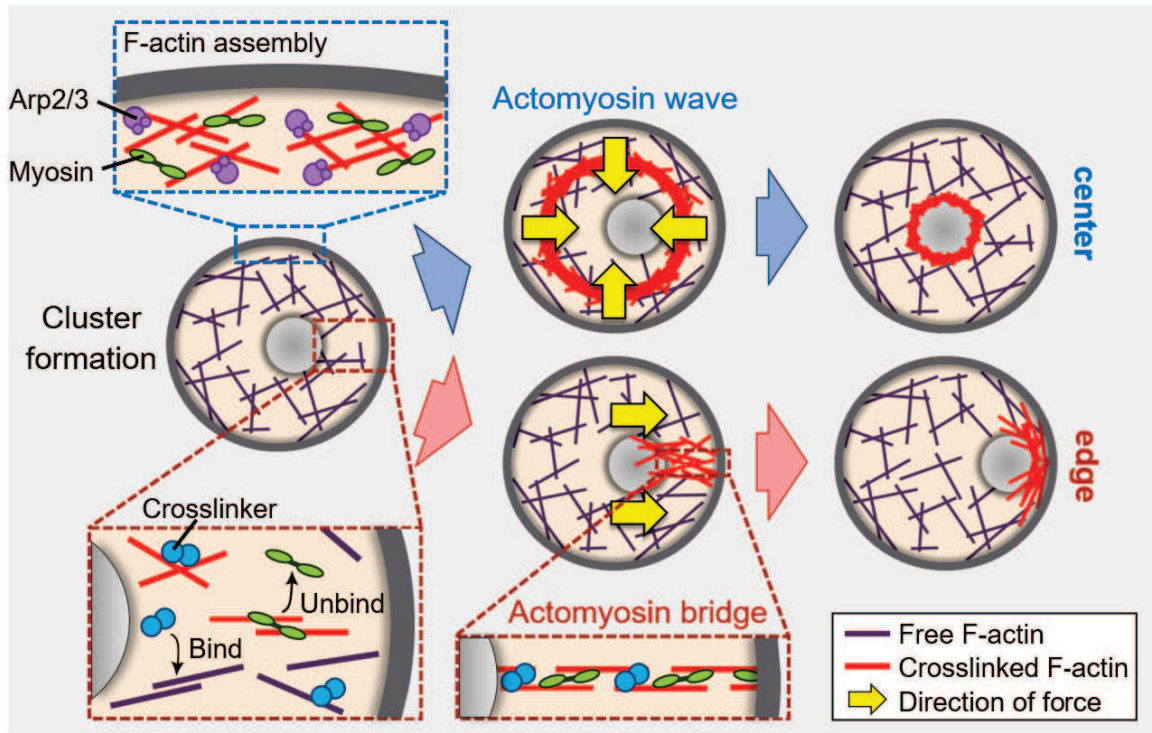
Figure 2.16: The tug-of-war model. (top) Actomyosin waves push the cluster to the droplet center in every wave period. The magnified view shows F-actin polymerized by Arp2/3 complex in the vicinity of the droplet surface. (bottom) When the actomyosin bridge is formed during the duration between successive periodic waves, the actomyosin bridge pulls the cluster to the edge. A magnified view shows the bulk dynamics of bridge formation, where actin-crosslinking proteins are bound and unbound to the F-actin. When the actomyosin bridge was sufficiently inter-connected, the bridge can generate pulling forces that move the cluster toward the edge.

2.3.7 Tug-of-war model of the cluster positioning

Here, we propose a conceptual model of cluster positioning. On the one hand, newly polymerized F-actin formed a ring-like structure at the droplet periphery, which is contracting toward the center and pushing the cluster toward the center (Fig. 2.16, top). On the other hand, in the bulk space of the droplet, actin crosslinkers and myosin probabilistically bind and unbind to the actin filaments (Fig. 2.16, bottom). When a bridge-like structure was formed between the cluster and the droplet, the bridge can generate contractile forces, and the cluster is contracted toward the edge. Taken together, the competing balance between these inwardly contracting

actomyosin waves and outwardly contracting actomyosin bridge determines the cluster positioning, which we named a 'tug-of-war' model. To experimentally test the tug-of-war model, we next asked if we can control the cluster positioning based on the model description. To answer this question, we modulated the property of the actomyosin bridge to change the balance between the wave and bridge. To this end, we added several actin-associated proteins which are expected to change the bulk F-actin properties, such as the extent of F-actin connectivity and F-actin length.

2.3.8 Experiment VI: Molecular perturbations on cluster positioning

To challenge the bridge formation hypothesis, we sought to control the cluster positioning by promoting or inhibiting the formation of actomyosin bridges. According to the actomyosin bridge model, the probability of the bridge formation could be affected by (i) the concentration of actin-crosslinking proteins and (ii) the length of individual actin filaments. Thus, we added actin-associated proteins to control the cluster positioning by changing the connectivity of the actomyosin networks.

First, when we added actin-crosslinking protein α-actinin that increases the connectivity of the network, the number of the edge-positioned cluster was increased (Fig. 2.17a-c). On the other hand, when we added F-actin cutting protein gelsolin that decreases the average length of actin filaments, the number of the center-positioned cluster was increased (Fig. 2.18a-c). Conversely, the number of the edge-positioned cluster was increased by adding F-actin elongation protein mDia2 (Fig. 2.19a-c). These results indicate that modulation of F-actin length or the extent of actin crosslinking could change the probability of the actomyosin bridge formation and, in turn, changes the cluster positioning. Confocal microscopy confirmed that the individual F-actin length was altered by the addition of gelsolin and mDia2 (Fig. 2.20). Note that the period and speed of the actomyosin wave was not affected by

this perturbation, suggesting that these perturbations were predominantly affecting the bulk actomyosin network, not for the newly formed ring-shaped actomyosin waves (Fig. 2.17d,e, Fig. 2.18d,e, and Fig. 2.19d,e). Together, these results further support the tug-of-war model in which the probabilistic actomyosin bridge formation controls the symmetry breaking of the cluster positioning.
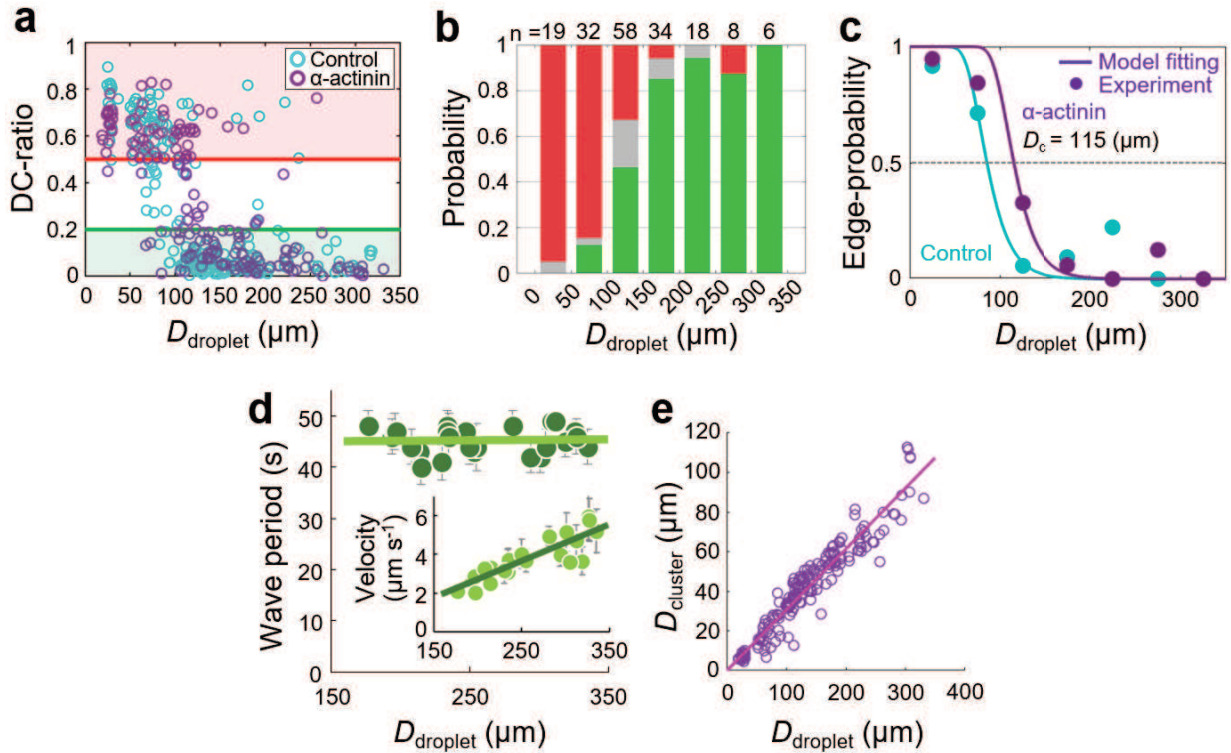
Figure 2.17: Addition of actin crosslinker, α-actinin (250 nM). (**a-c**) Droplet diameter dependence of the DC-ratio and edge-probability. Edge-positioned probability was fitted by Eq. (2.7) using $L = 6.1$ μm and $\tau = 0.09$ s. Transition diameter $D_c = 115$ μm. (**d**) Droplet diameter dependences of the wave period and contraction velocity (inset). The wave period T and contraction velocity v were fitted by $T = 1.8 \times 10^{-3} D_{\mathrm{droplet}} + 45$ and $v = 1.9 \times 10^{-2} D_{\mathrm{droplet}} - 1.1$, respectively. (**e**) Droplet diameter dependence of the cluster diameter. The scatter plot was fitted by $D_{\mathrm{cluster}} = 0.31 D_{\mathrm{droplet}}$. Kolmogorov-Smirnov test was applied to the scatter plots of DC-ratio between $50 < D_{\mathrm{droplet}} < 150$ (around the transition point in the control experiment), where the distributions were significantly different from the control ($p < 0.01$).
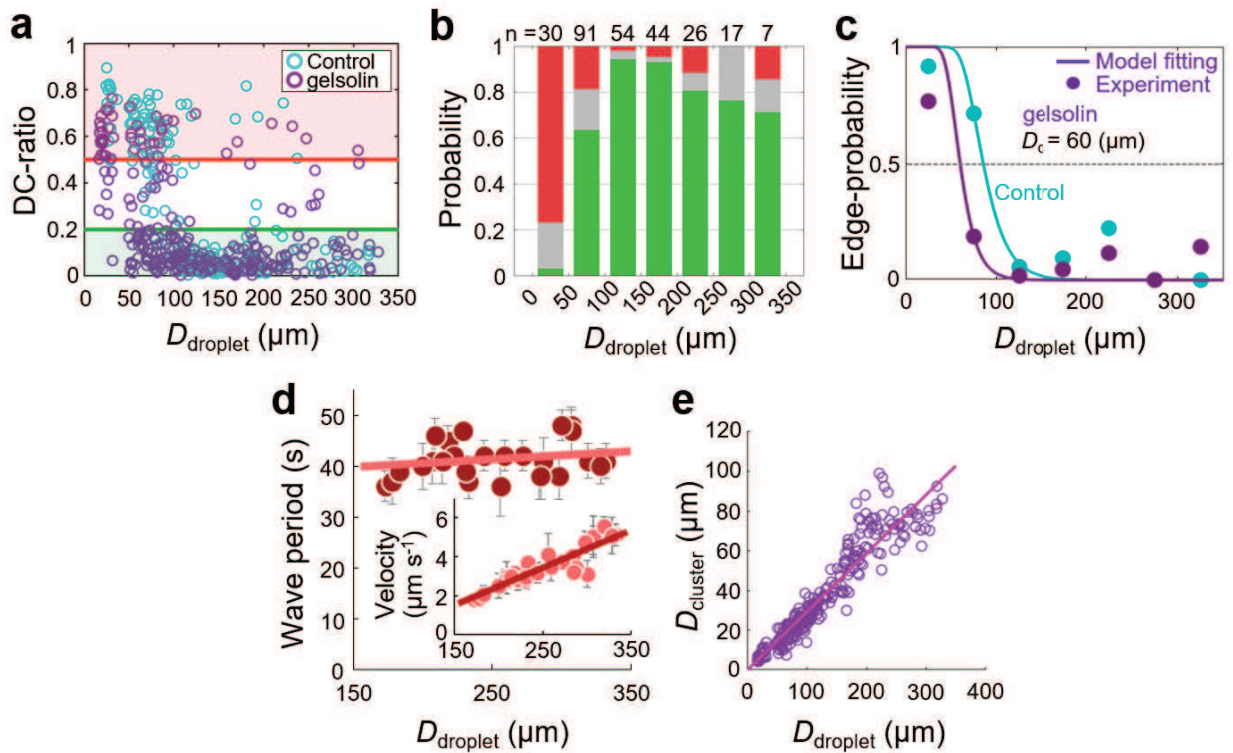
Figure 2.18: Addition of the actin severing protein, gelsolin (300 nM). (**a-c**) Droplet diameter dependence of the DC-ratio and edge-probability. Edge-positioned probability was fitted by Eq. (2.7) using $L = 4.3$ μm and $\tau = 0.46$ s. Transition diameter $D_\mathrm{c} = 60$ μm. (**d**) Droplet diameter dependences of the wave period and contraction velocity (inset). The wave period T and contraction velocity v were fitted by $T = 1.5 \times 10^{-2} D_\mathrm{droplet} + 38$ and $v = 1.9 \times 10^{-2} D_\mathrm{droplet} - 1.3$, respectively. (**e**) Droplet diameter dependence of the cluster diameter. The scatter plot was fitted by $D_\mathrm{cluster} = 0.29 D_\mathrm{droplet}$. Kolmogorov-Smirnov test was applied to the scatter plots of DC-ratio between $50 < D_\mathrm{droplet} < 150$ (around the transition point in the control experiment), where the distributions were significantly different from the control ($p < 0.01$).
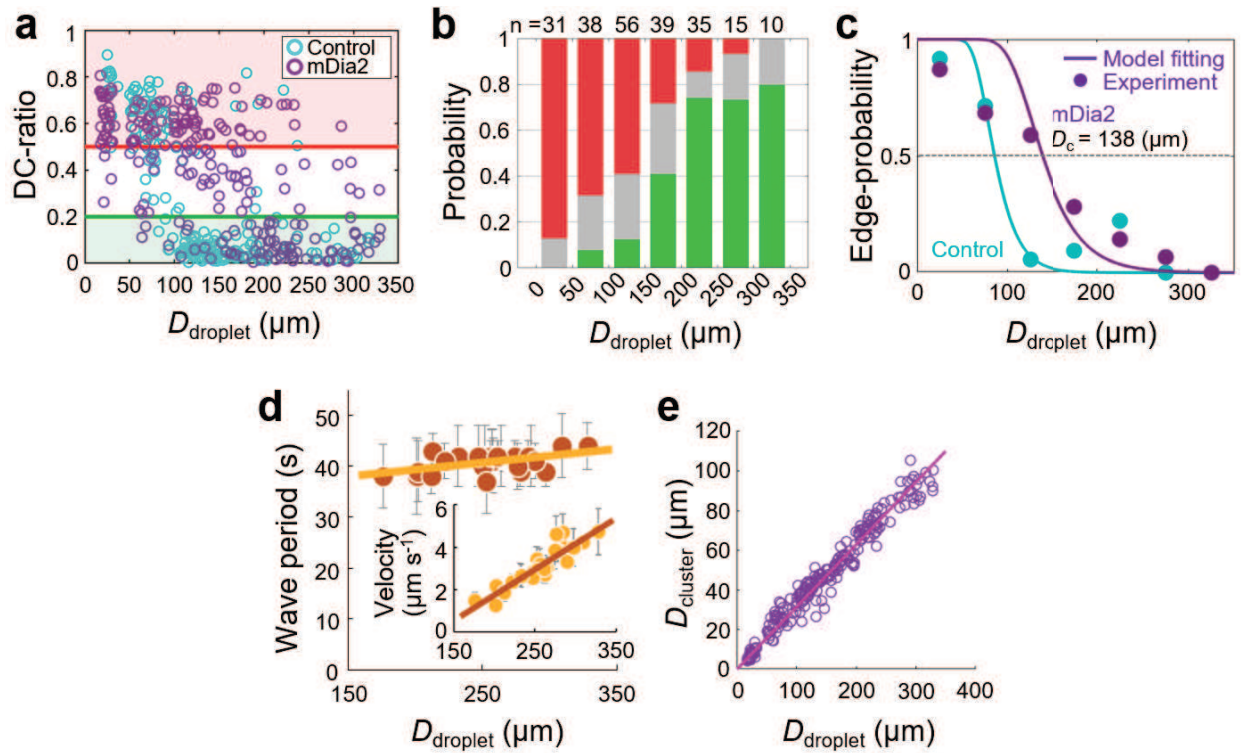
Figure 2.19: Addition of actin polymerization activator, mDia2 (30 nM). (**a-c**) Droplet diameter dependence of the DC-ratio and edge-probability. Edge-positioned probability was fitted by Eq. (2.7) using $L = 10$ μm and $\tau = 0.46$ s. Transition diameter $D_c = 138$ μm. (**d**) Droplet diameter dependences of the wave period and contraction velocity (inset). The wave period T and contraction velocity v were fitted by $T = 2.7 \times 10^{-2} D_{\text{droplet}} + 34$ and $v = 2.4 \times 10^{-2} D_{\text{droplet}} - 3.1$, respectively. (**e**) Droplet diameter dependence of the cluster diameter. The scatter plot was fitted by $D_{\text{cluster}} = 0.31 D_{\text{droplet}}$. Kolmogorov-Smirnov test was applied to the scatter plots of DC-ratio between $50 < D_{\text{droplet}} < 150$ (around the transition point in the control experiment), where the distributions were significantly different from the control ($p < 0.01$).
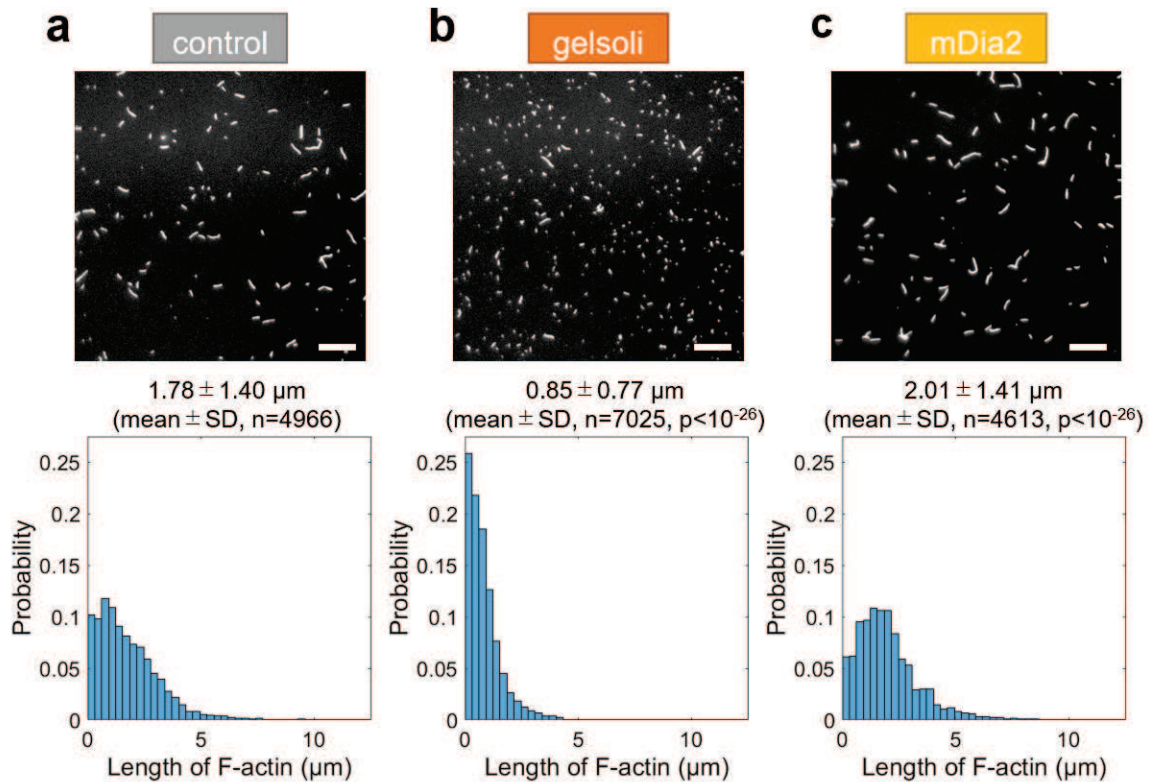
Figure 2.20: The length distribution of F-actin is measured by epi-fluorescence microscopy. F-actin was fixed and visualized by rhodamine-phalloidin. The length distribution of gelsolin and mDia2 are significantly different from the control experiment (p-values are displayed; Kolmogorov-Smirnov test). (**a**) Control experiment. Mean F-actin length: 1.78 ± 1.38 μm (sample size, n=4966). (**b**) Addition of 300 nM gelsolin. Mean F-actin length: 0.87 ± 0.76 μm (n=7025, $p < 10^{-26}$). (**c**) Addition of 30 nM mDia2. Mean F-actin length: 2.02 ± 1.40 μm (n=4613, $p < 10^{-26}$). The typical maximum lengths of F-actin (top 5 % average) in the extracts were 5.7 μm (control), 3.2 μm (gelsolin) and 6.0 μm (mDia2), respectively. All images were taken by epi-fluorescence microscopy. Scale bars, 10 μm.

2.3.9 Theory II: Force percolation description of the tug-of-war model

The tug-of-war model indicates that the periodically generated actomyosin waves push the cluster toward the center, while the probabilistically formed actomyosin bridges pull the cluster toward the edge. Based on this model, one might expect that the symmetry breaking of the cluster positioning would occur by the disruption of the balance between these forces, but how does the cluster positioning change with the droplet size?

To answer this question, we consider the balance between 'characteristic timescales' that govern the formation of these distinct actomyosin structures. We have shown that the actomyosin waves are generated with period T and push the cluster toward the center, in which the wave period is not much changed with the droplet size. In contrast, the average formation time τ_p of an actomyosin bridge would exponentially increase with the larger droplet sizes, because several actin filaments with the length of few microns must align over the droplet radius with the length of a few tens microns [1]. In this case, the crossover between the wave period T and the bridge formation time τ_p would occur as the droplet size increases, in which either one of the actomyosin structures maturate faster than the other would dominate the cluster positioning, and thus the cluster positioning would be altered depending on the droplet size (Fig. 2.21a).

The period of wave $T(R)$ generation was modeled in Theory I, while how did the bridge formation time τ_p alter with radius R? The actomyosin bridge is expected to form through probabilistic crosslinking of each actin filaments via actin crosslinker such as α-actinin. This kind of phenomenon is known to be effectively described by the

---

[1]For example, to form an actomyosin bridge with filament length $L = 1$, we need two or ten filaments in the droplet with radius $R = 2$ or $R = 10$ respectively. Given that each filament is interconnected with probability $(1/2)$, we can estimate the bridge formation probability as $(1/2)^{R/L} = (1/2)^2$ and $(1/2)^{10}$, thus it is exponentially difficult to form a bridge in the larger droplet.
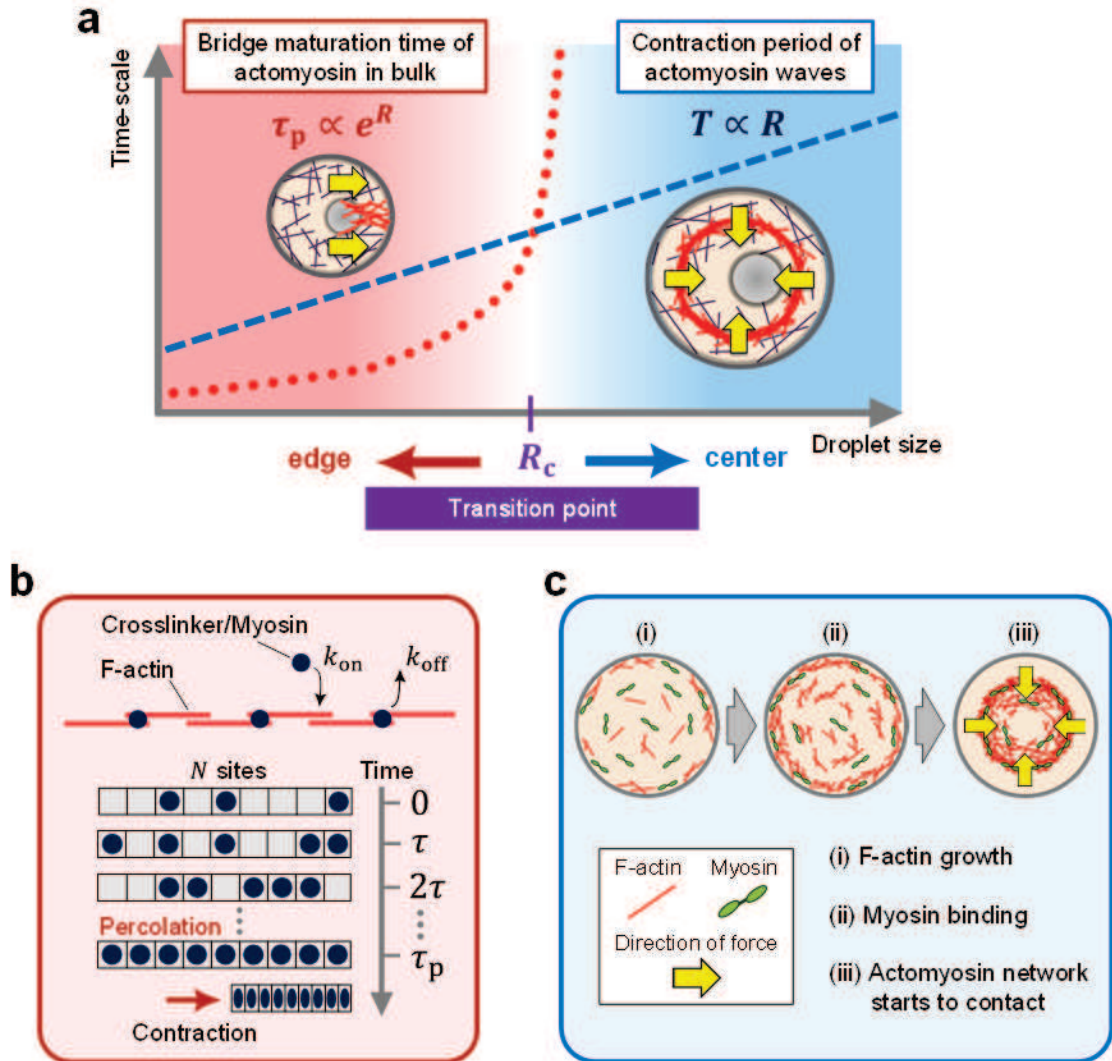
Figure 2.21: (**a**) The mechanism of the droplet size-dependent cluster positioning. Actomyosin waves transport the cluster toward the droplet center every period of $T \propto R$, while stochastically formed actomyosin bridges (mean maturation time $\tau_{\mathrm{p}} \propto e^R$) transport the cluster toward the droplet boundary. Since the characteristic time scales of the two antagonistic forces have different size dependences, the transition radius R_{c} is determined by one unique crossover point. (**b**) The percolation model of actomyosin bridge formation. We describe the stochastic binding/unbinding dynamics as the percolation process, where crosslinking sites are occupied by crosslinkers with a probability of $1/2$ in every time step τ, where k_{on} and k_{off} indicate the binding and unbinding rates of crosslinkers, respectively. When all sites (the total number N) are occupied by crosslinkers after time τ_p has passed, the actomyosin bridge can generate contractile stress, by which the cluster is transported toward the droplet edge. (**c**) An active gel model of periodic actomyosin wave formation. The wave period is determined by the sum of three sequential processes: (i) actin network formation by F-actin growth, (ii) stress generation by myosin binding, and (iii) the ring starts to contract toward the droplet center.

percolation theory in which probabilistic connection between individual elements play a crucial role [58]. Percolation theory is often used to describe the phenomena that show transition depending on the network connectivity, and percolation transition is characterized by the emergence of the interconnected network that spans the entire system [90]. Note that the actomyosin network has distinct aspects depending on the density of the network: interconnected dense actomyosin networks behave like elastic material or viscous fluid [44], while the sparse low-density individual filaments can transmit forces when it comes to crosslinked enough each other [26]. Recently, the force percolation was found in bulk purified actomyosin network or agent-based simulation of actin-myosin-crosslinker systems [58, 59, 43].

Here, we constructed the theoretical model of the tug-of-war model based on percolation theory. To obtain the analytical expression, we assumed the two-state model in which the cluster takes only either the center or the edge position for simplicity. First, the actomyosin waves contract toward the center that places the cluster on the center at every period T. On the other hand, once the number of $\sim N$ actin filaments are interconnected between the cluster and the droplet surface, the actomyosin bridge can generate contractile force and the cluster is placed at the edge (Fig. 2.21b). Given that the actin-crosslinking proteins randomly bind and unbind the actin filaments, the probability of the actomyosin bridge formation is written as $(1/2)^N$. This actomyosin bridge must be formed during the period T to place the cluster at the edge, otherwise, it will be placed at the center by periodic actomyosin waves (Fig. 2.21c). Therefore, the available trial of the actin-crosslinking events can be written as T/τ, where $\tau = 1/(k_{\mathrm{off}} + C_0 k_{\mathrm{on}})$ is the characteristic turnover time of crosslinkers [91], C_0 denotes concentration of crosslinkers, and k_{on} and k_{off} denote binding and unbinding rates of crosslinkers on actin filaments, respectively. Thus, the probability of the actomyosin bridge formation, in which the total number of N actin filaments are interconnected between the cluster and the droplet surface at least one time during the

period T can be written as $p = 1 - [1 - (1/2)^N]^{T/\tau}$. Given that the average length of actin filaments L and the radius of the droplet R, the total number of crosslinker binding sites N can be written as $N \sim R/L$. Finally, the edge-positioning probability of the cluster can be written as

$$p(R) = 1 - \left[1 - \left(\frac{1}{2}\right)^{R/L}\right]^{T(R)/\tau} \tag{2.7}$$

We use Eq. (2.7) to estimate physical quantities and transition diameter D_c at which $p(D_c) = 0.5$. Equation (2.7) is fitted to the results of control experiments with the following two parameters: the contour length of actin filaments L and the turnover rate of crosslinkers τ, and estimated $L = 6.1$ μm, $\tau = 0.46$ s, and $D_c = 85$ μm (Fig. 2.13c). The obtained value of τ is similar to the literature value $\tau = 0.54$ s, given that $k_{off} = 0.66$ s^{-1}, $k_{on} = 1.2 \times 10^6$ M^{-1} s^{-1} [92], and the concentration of actin and α-actinin in *Xenopus* egg extracts are ~ 20 μM and $C_0 \sim 1$ μM, respectively [93]. Moreover, the obtained F-actin length ($L = 6.1$ μm) is also nearly consistent with the experimentally measured value of the top 5% average of the F-actin length $L = 5.7$ μm. Here we use the top 5% average of the F-actin length distribution for comparison because the tug-of-war model predicts that long filaments predominantly contributes to the network percolation as explained in the following section.

Edge-positioning probability considering the length distribution of F-actin.
Here, we used the top 5% average length of F-actin computed from the length distribution (Fig. 2.20a). So far, we have only considered the probability of actin-crosslinking. For a more detailed description, however, we need to take into account the length distribution of F-actin. This is because the bridge formation time is basically two steps: (i) The filaments of length l taken from the length distribution $p_b(l)$ align over the distance R, and then (ii) each filaments are inter-connected by actin-crosslinking proteins in which the number of sites are $N \sim R/l$ (Fig. 2.22a,b).
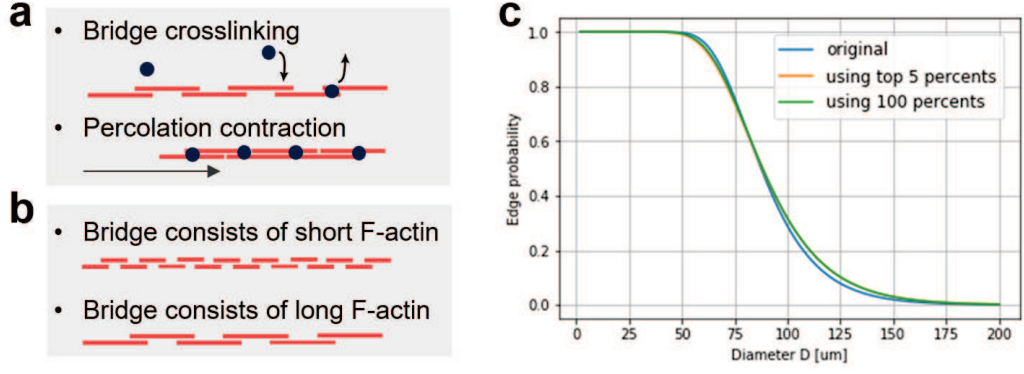
Figure 2.22: (**a**) Schematic showing the bridge crosslinking process and the subsequent contraction of the bridge after force percolation. (**b**) Schematic showing the bridge alignment with different length of individual F-actin. To derive the more presize description, here we consider the length distribution of F-actin (in Fig. 2.20) instead of mean F-actin length. (**c**) Edge-probability was plotted along the droplet diameter, compared between original model (blue solid line), the model only considering top 5% of the longest filaments (orange solid line), and the model considering all the actin filaments (green solid line).

For step (i), the probability that the filaments with length l align along the droplet radius R is written as $P_b(l) = p(l)^{R/l} / \int_0^{l_{max}} p(l')^{R/l'} dl$ where l_{max} is the longest length of F-actin in the distribution. For step (ii), as we discussed already, the probability that the all $N(= R/l)$ binding sites are not occupied by crosslinkers is written as $g(l) \equiv 1 - (1/2)^{R/l}$. Therefore, the probability that there is no bridge consisting of any F-actin length between $l_{min} < l < l_{max}$ is written as

$$g(l_{min}) \times g(l_1) \times g(l_2) \cdots g(l_{max}) = \exp\left[\sum_{l_{min}}^{l_{max}} \log\{g(l)\}\right] \qquad (2.8)$$

By taking into accout the contribution of the length distribution of F-actin $P_b(l)$, Eq. (2.8) can be written as $\exp[\int_{l_{min}}^{l_{max}} \log\{g(l)\}P_b(l)dl]$. Finally, the probability that the bridge formation occurs at least once during period T is given by

$$p(R) = 1 - \left(\exp\left[\int_{l_{min}}^{l_{max}} \log\{g(l)\}P_b(l)dl\right]\right)^{T/\tau}, \qquad (2.9)$$

which is the detailed version of the edge-positioning probability Eq. (2.7).

By using Eq. (2.9), we compare the following two cases: the edge-positioning probability calculated by using (i) 100% distribution, or (ii) only top 5% distribution of actin filaments (Fig. 2.22c). Firstly, for simplicity, we assume that the length distribution of F-actin is given by $p(l) = (1/L_A) \exp(-l/L_A)$, where the mean value of the control experiment ($\sim$1.8 μm, Fig. 2.20a) is used for L_A. Next, l_{max} is adjusted to match the curve Eq. (2.9) to the original curve of the control experiment (Fig. 2.13c) with using the same values for T. The fitting gives $l_{max} = 7.0$ μm. Then, we change only l_{min} value and compare the following two cases: (i) using 100% distribution, (ii) using only top 5% distribution. The curves calculated by using 100% distribution (green line; $l_{max} = 7.0$ μm, $l_{min} = 0$ μm) and by using top 5% distribution (orange line; $l_{max} = 7.0$ μm, $l_{min} = -L_A*\log(0.05+(1-0.05)*\exp(-l_{max}/L_A)) = 4.8$ μm) are mostly overlapped (Fig. 2.22c). Thus, we can conclude that it is reasonable to assume that the top 5% of filaments predominantly contributes to the bridge formation.

Since we found that the top 5% predominantly contributes to the bridge formation, we can approximate Eq.(2.9) by assuming that only the filaments with a typical maximum length L participate in the bridge formation. Under this approximation, we can rewrite $l \sim L$ and $P_b \sim 1/(l_{max} - l_{min})$ in Eq. (2.9), which finally corresponds to Eq. (2.7).

Numerical simulation of the cluster positioning. To further substantiate the percolation model of the cluster positioning, we performed the stochastic simulation of the cluster positioning. The basic setup and the meaning of parameters are the same as in the previous sections, but the only difference is that here we consider the spatial movement of the cluster, which was not considered so far to obtain the analytical expression (Fig. 2.23a,b). Here, we assume that the cluster is started to be contracted toward the edge when the actomyosin bridge is formed between the cluster and the droplet boundary. We implement this in our numerical simulation as
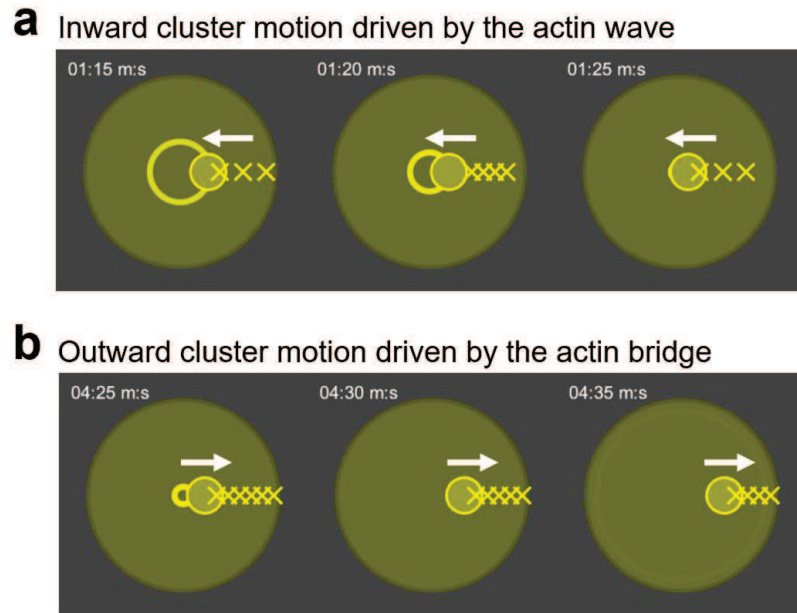
Figure 2.23: Numerical simulation of the cluster positioning. (**a**) Time-lapse images of an inwardly moving cluster contracted by the actomyosin wave. (**b**) Time-lapse images of an outwardly moving cluster contracted by the actomyosin bridge.

follows. In every time step of τ, each crosslinking site takes an "on" or "off" state with equal probabilities, $1/2$. By repeating this trial, the actomyosin bridge starts to contract the cluster toward the edge when all N sites are occupied by crosslinkers. The contraction speed is assumed to be equal to the velocity of the actomyosin wave v for simplicity. At the same time, actomyosin waves are generated from the boundary every period of T, and they propagate toward the droplet center with velocity v. We used the diameter D dependence of the T and v same as the control condition in the experiment (Fig. 2.7c,d). Contraction of the actomyosin bridge is stopped when the outwardly moving cluster collides with the inwardly propagating wave, and subsequently, the cluster is started to be transported toward the center of the droplet by the wave. If the percolation occurs during the transportation by the wave, the newly formed actomyosin bridge again starts to move the cluster toward the edge.

With this setup, the numerical simulation results and the analytical expression mostly follow the same trend using the same parameter sets, indicating that the ana-

lytical expression is a good approximation (Fig. 2.24a,b). The influence of the actin-crosslinker concentration C_0 and the individual filament length L also reproduces the qualitative trend observed in the molecular perturbation experiments. Note that the numerical simulation slightly has the larger edge probability in all conditions. This is qualitatively explained by considering the contribution of the spatial movement of the cluster. When a cluster is located at the center in the droplet with radius R, the number of actin-crosslinking sites that is necessary to be occupied is $N \sim R/L$. However, once the cluster is slightly contracted toward the edge, the distance between the cluster and the droplet periphery is decreased, for example, $R \to 0.8R$. In this location, the number of actin-crosslinking sites that are necessary to be occupied is $N \sim 0.8R/L$. Reminding that the bridge formation probability is given by $(1/2)^N$, the spatial movement of the cluster toward the edge exponentially increases the bridge formation probability. Therefore, the edge probability in numerical simulation becomes larger than the analytical expression. Together, the analysis of the numerical simulation clarifies the non-negligible influence of spatial movement on cluster positioning.
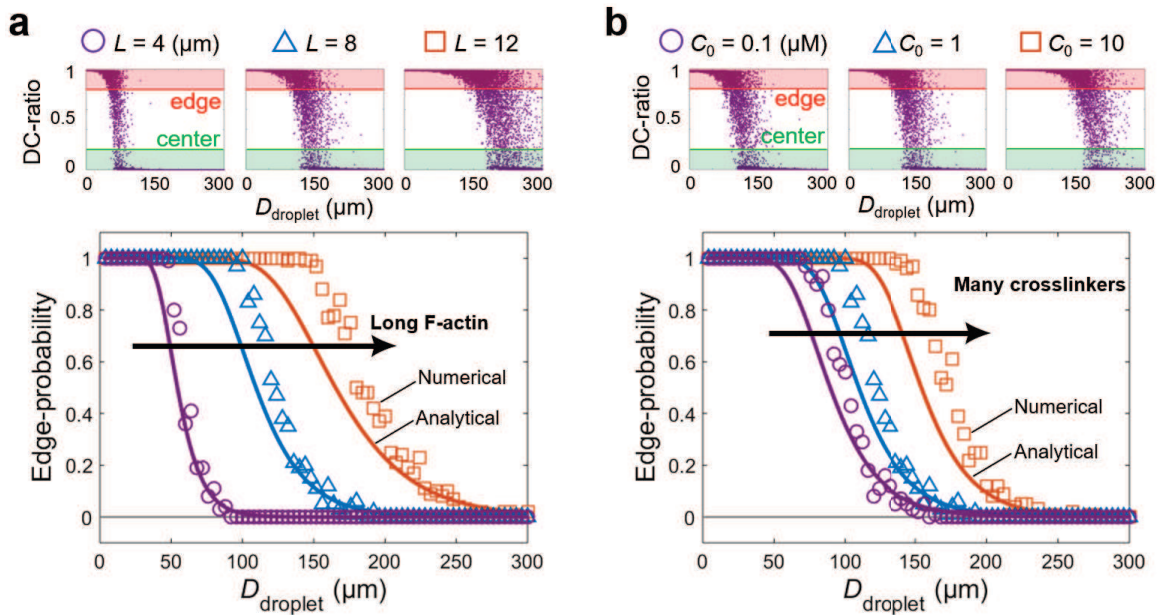
Figure 2.24: Numerical simulation of the cluster positioning. (**a**) DC-ratio of the numerical simulation (top) and the calculated edge-probability (bottom) with different F-actin length. Numerical simulation (symbols) and the analytical expression (solid curves) follows the same trend. (**b**) DC-ratio of the numerical simulation (top) and the calculated edge-probability (bottom) with different crosslinker concentration C_0, where crosslinker concentration and turnover rate are related by the expression $\tau = 1/(k_{\text{off}} + C_0 k_{\text{on}})$, where $k_{\text{off}} = 0.66$ s^{-1} and $k_{\text{on}} = 1.2 \times 10^6$ M^{-1} s^{-1}. Numerical simulation (symbols) and the analytical expression (solid curves) follows the same trend. In the numerical simulations, the time-averaged DC-ratio $(1/T_0) \int_0^{T_0} [d_c(t)/R] dt$ $(T_0 = 1800$ s) was calculated for each droplet to calculate the average position of the droplet, which is displayed as purple dots (top). Thereafter, edge probability was determined from the DC-ratio, where the DC-ratio greater than 0.8 was classified as 'center', and smaller than 0.2 was classified as 'edge', by which the edge-probability was calculated.

Transition points predicted through timescales The above detailed theoretical analysis based on the percolation model showed that the cluster positioning is determined by the tug-of-war-like balance between the two distinct actomyosin networks, that is, the periodically generated actomyosin waves and the probabilistically formed actomyosin bridges. On the other hand, we can simply predict the transition radius R_c at which the positioning symmetry breaks by considering the crossover point of the two timescales, wave period T, and bridge maturation time τ_p (Fig. 2.21a). Using the equality $T = \tau_{\mathrm{p}}$ and the radius dependence of the bridge maturation time $\tau_p = \tau 2^{R/L}$, the transition radius is given by

$$\frac{R_{\mathrm{c}}}{L} = \log_2\left(\frac{T}{\tau}\right), \tag{2.10}$$

where the radius dependence of T is assumed negligibly small according to the experimental result. Using the experimentally measured top 5% average F-actin length $L = 5.7\ \mu\mathrm{m}$ and the literature value of the crosslinker turnover time $\tau = 0.54$ s, the transition diameter is given by $D_{\mathrm{c}} = 2R_{\mathrm{c}} \sim 73\ \mu\mathrm{m}$. This is close to the experimentally measured transition point $D_{\mathrm{c}} \sim 85\ \mu\mathrm{m}$, indicating that the timescale picture captures the main feature of the symmetry breaking of the cluster positioning, which further substantiates the tug-of-war model. Together, the theoretical modeling of the tug-of-war model showed that the cluster positioning is determined by the balance between the two distinct actomyosin structures having different droplet-size dependence of their maturation timescales.

2.4   Discussion

In this study, we have investigated how the position of the cluster, a simplified model of the cell nucleus, is controlled through contractile forces of actomyosin networks. The artificial cell model allowed us to flexibly control the droplet size, which is usually difficult in living cells and dissected the entangled contribution of the two actomyosin structures; actomyosin waves and actomyoin bridges. In mouse oocytes, it has been reported that F-actin polymerization was enhanced when the nucleus is being transported to the edge [5]. Based on our findings, this result could be interpreted as the increased percolation probability of the actomyosin bridge maturation by increasing the F-actin length. Moreover, we have shown that the enhanced actin-crosslinking also increases the number of edge-positioned clusters. Using these molecular understandings on cellular mechanics will enable us to assist the proper nucleus positioning by adding these molecular components to reduce the positioning failure and avoid cell death.

In addition, we showed that the active gel behavior of contractile actomyosin networks could regulate important cellular functions as the nucleus positioning. Although it is still unclear how the actomyosin waves in living cells could be involved in the nucleus positioning, some studies reported that the actomyosin waves are generated during the symmetric cell division in which the nucleus was located in the center [117] and during cell migration in which the nucleus position become asymmetric [11]. The investigation of the detailed mechanism of wave-driven nucleus positioning will be a significant future challenge. In addition, we show that the periodic contractile wave can robustly position the cluster at the center of the asymmetric confinement, indicating that the actomyosin wave could be a useful tool to robustly control the centered nucleus positioning and microscale material transport (Fig. 2.25). Besides, this kind of periodic actomyosin wave generation has not been observed in the previously reported *Xenopus* egg extracts systems, where the activity of actomyosin networks
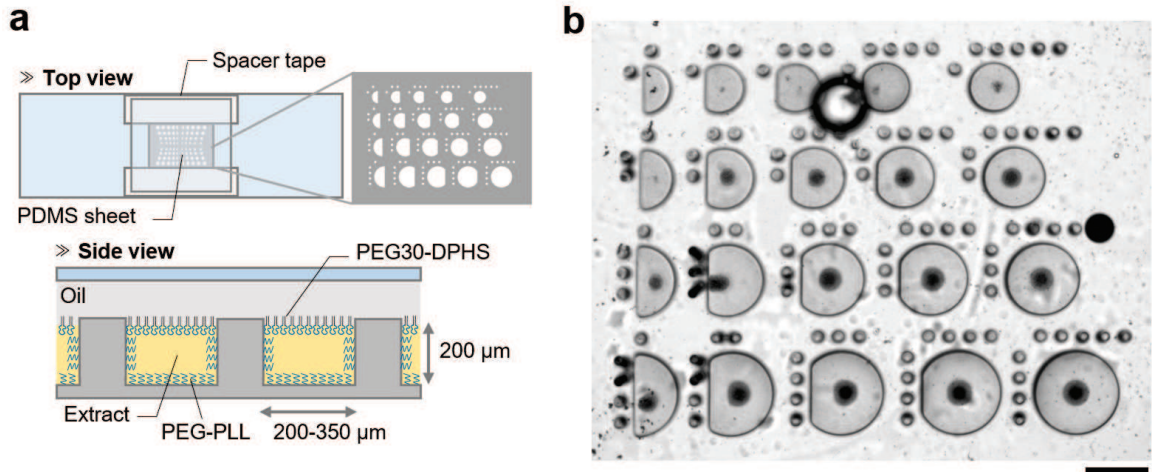
Figure 2.25: (**a**) Schematic showing the extracts confined in patterned PDMS chambers which are sealed by the oil containing PEG30-DPHS. The surface of the PDMS chamber was coated by PEG-PLL, thus both the extract-PDMS interface and the extract-oil interface were passivated with PEG, eliminating the adhesion of actin with the boundaries. (**b**) A bright-field image of the extracts confined in the asymmetric chambers. Most of the clusters were located near the center even in the highly asymmetric chamber. Scale bar, 300 μm.

might be lower than the present study [23, 24, 26]. Thus, investigation of the mechanism of the periodic actomyosin waves would give a new understanding in the field of active gel physics and non-linear systems, which will be studied in Chapter 4.

On the other hand, we have also shown that the sparse actomyosin networks could participate in the cluster positioning. Although force percolation of the actomyosin networks has been found in the bulk mm-sized purified systems [58, 59, 90], the present study reports the first evidence of the percolation-like behavior of actomyosin networks in a cell-sized system, furthermore, it could also regulate the biologically important function like nucleus positioning. We have also shown the biological advantage of the percolation through modeling of the positioning, where the spatial movement could further bias the cluster positioning toward the edge. Such feedback mechanism could facilitate the cells to place the nucleus at the edge to perform asymmetric reductional cell division. However, the detailed physical properties of the percolation in the cell-sized confinement such as finite-size scaling and how much

force is exerted by the percolated actomyosin network remain open. Further analysis using high-resolution microscopy to quantify the orientation and connectivity in the actomyosin bridge as well as the force measurement using optical tweezer would be important future works to unveil the percolation mechanism of actomyosin network in the cell-sized small active systems.

From the physical point of view, two distinct actomyosin structures having different physical properties are coexisting in the same system, in which dense actomyosin networks form gel-like properties while the sparse actomyosin networks exhibit a gas-like percolation behavior. Interestingly, such coexistence of distinct actomyosin structures is often observed in living systems. For example, in migrating cells, newly formed sparse filaments at the cell front are accumulated toward the cell rear by retrograde flow and gradually forms a gel-like structure [11]. Such coexistence of the distinct actomyosin structures with different physical properties may play a significant role to realize flexible biological function and susceptibility to response environmental changes, thus realizing such coexisting actomyosin networks in a better-controlled manner in artificial cells will be an important future challenge.

2.5   Conclusion

Here, we have shown that the cluster positioning is determined by the balance between the two antagonistic forces produced by the distinct actomyosin structures; actomyosin waves and actomyosin bridges. We found that such distinct structures play a significant role in controlling the precise cluster positioning. The simple theoretical description of the tug-of-war model allows us to predict the transition point based on the crossover between the different maturation time scales of wave and bridge, providing a simple physical understanding of the cellular positioning symmetry breaking.

Chapter 3

Shape Symmetry Breaking-induced Droplet Migration

3.1 Introduction

3.1.1 Cell migration under confined environments

Cell migration plays pivotal roles in biological phenomena, ranging from immune cell response to pathogens [94], cancer cell migration through collagen network in our body [13] (Fig. 3.1a,b), and even in the migration through living embryo [11]. The key player driving the migration is the actin cytoskeleton, where actin flow propagating from the cell front to the rear part of the cell propels the cell body forward, in which the contractile force of myosin molecular motor sustains the continuous actin flow [95] (Fig. 3.1c).
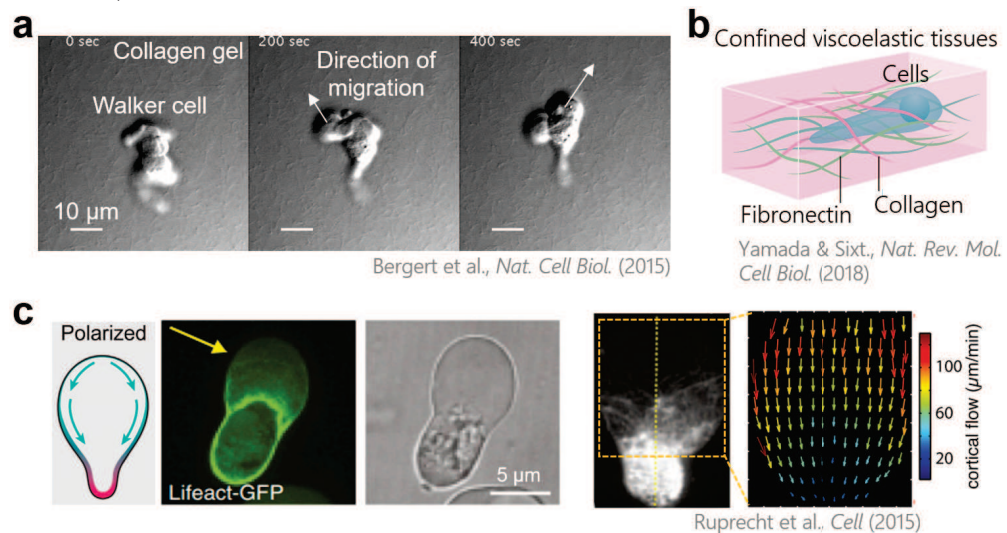
Figure 3.1: (**a**) Time-lapse images of the cancer cell (Walker cell) migrating through the collagen gel. (**b**) Schematic showing the cell migrating through collagen and fibronectin network. (**c**) The polarized actin distribution which sustains the actin flow. Images were adopted from [13, 97, 11]
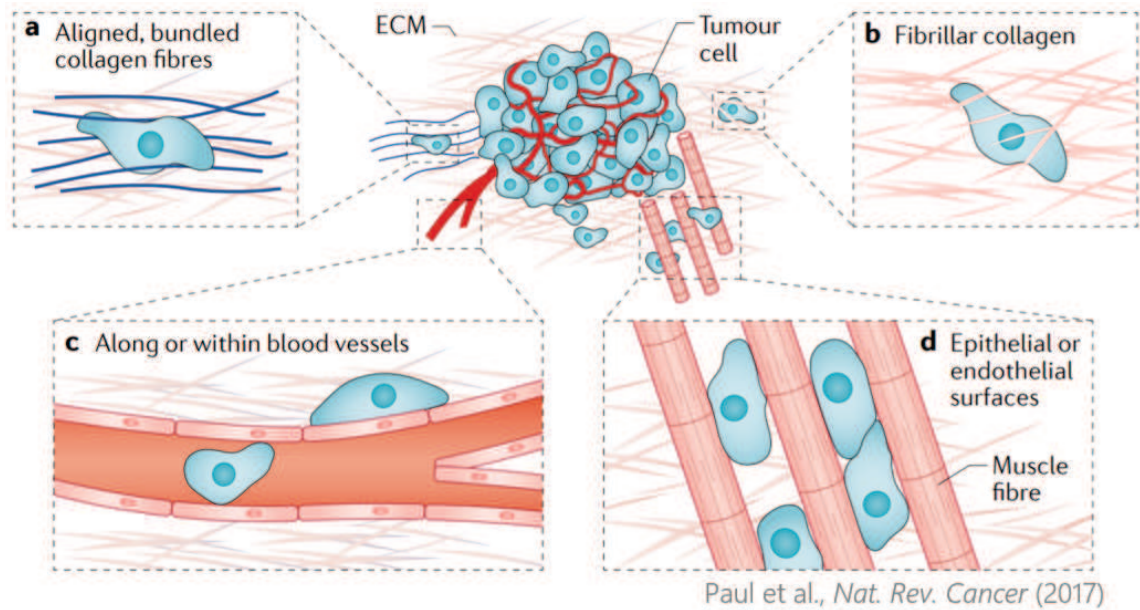
Figure 3.2: Microenvironments for confined migration in vivo. The extratumoural microenvironment offers numerous paths for confined cell migration. (**a**) Alignment and bundling of collagen fibres at the tumour periphery provide cues for directed migration. (**b**) Cells may also migrate through unbundled extracellular matrices (ECMs), such as fibrillar collagen, which present pore-like migration spaces. (**c**) Microtracks also occur both intravascularly and perivascularly. (**d**) Cells can also migrate between epithelial or endothelial surfaces, such as those found between muscle and nerve fibres Figures and Captions were adopted from [98].

Importantly, for cells to migrate, cells must transmit intracellularly generated contractile forces to the external substrate under confined microenvironments (Fig. 3.2) [97, 98]. A classic example is the cell migration on a 2D substrate, where cells form focal adhesions strongly bound to the extracellular matrices or patterned substrates (Fig. 3.3a,c). Thus, cells can efficiently transmit intracellular forces to the substrate, by which cells migrate [65]. On the other hand, recent studies have shown that even without focal adhesions, cells can migrate in 3D confinement such as in collagen network and microchannels, where friction force was proposed as a propulsion force of the migration [96] (Fig. 3.3b,c). Although a previous study showed that the migration speed slows down by reducing the friction of the external substrate, how intracellularly generated contractile forces can be transmitted to the external environment in the
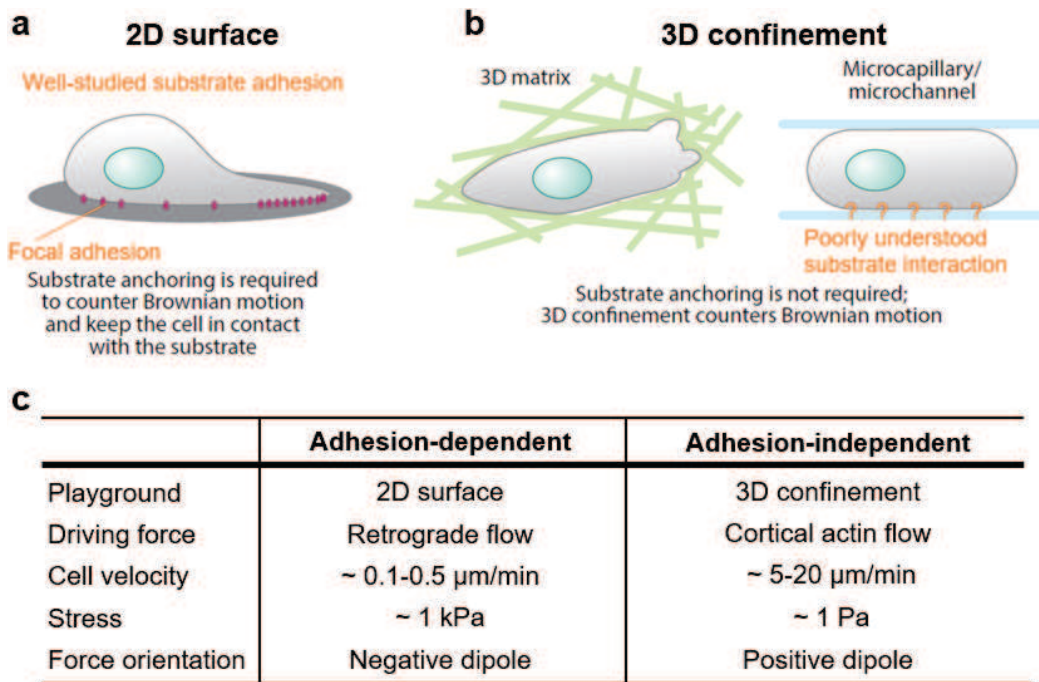
Figure 3.3: (**a**) Schematic showing the adhesion-dependent migration on 2D substrate, where the focal adhesion complex efficiently transmits the intracellularly generated contractile forces of actomyosin. (**b**) Schematic showing the adhesion-independent migration through the 3D confined environments such as extracellular matrix and the microchannels. (**c**) Table summarizing the characteristic properties of the adhesion-dependent and -independent migration. Figures were adopted from [96]

absence of focal adhesion is still poorly understood. This is because the multiple lipid components of the cell membrane and complex signaling pathways regulating actomyosin contractility hindered us to study how the physical interaction between the actin flow and the lipid membrane leads to propulsion force generation in confined environments.

To solve this bottleneck of the living cell experiments, here we develop a migratory cell model to investigate how actin-membrane binding can transmit the intracellular

forces to the external substrate and enable spontaneous migration. Note that previous artificial cell studies only focused on intracellular structure formation, such as a contractile ring in water-in-oil droplet [111] and spindle positioning in Chapter 2 [28, 29] (Fig. 3.4a). These studies focused on the inside of the cells, so the droplets were used as a passive cell wall. On the other hand, cell migration is accompanied by dynamic shape changes, thus we need to implement such active functional interface. To do so, we focused on the two kinds of characteristic symmetry breaking of the migratory cells: symmetry breaking of the nucleus positioning and the symmetry breaking of the cell shape (Fig. 3.4b). We reasoned that, if we can implement such shape symmetry breaking, droplets could migrate. Indeed, with this strategy, we successfully realized the cell-like actomyosin droplet migration and then asked what is the mechanics behind the migration (Fig. 3.4c,d).
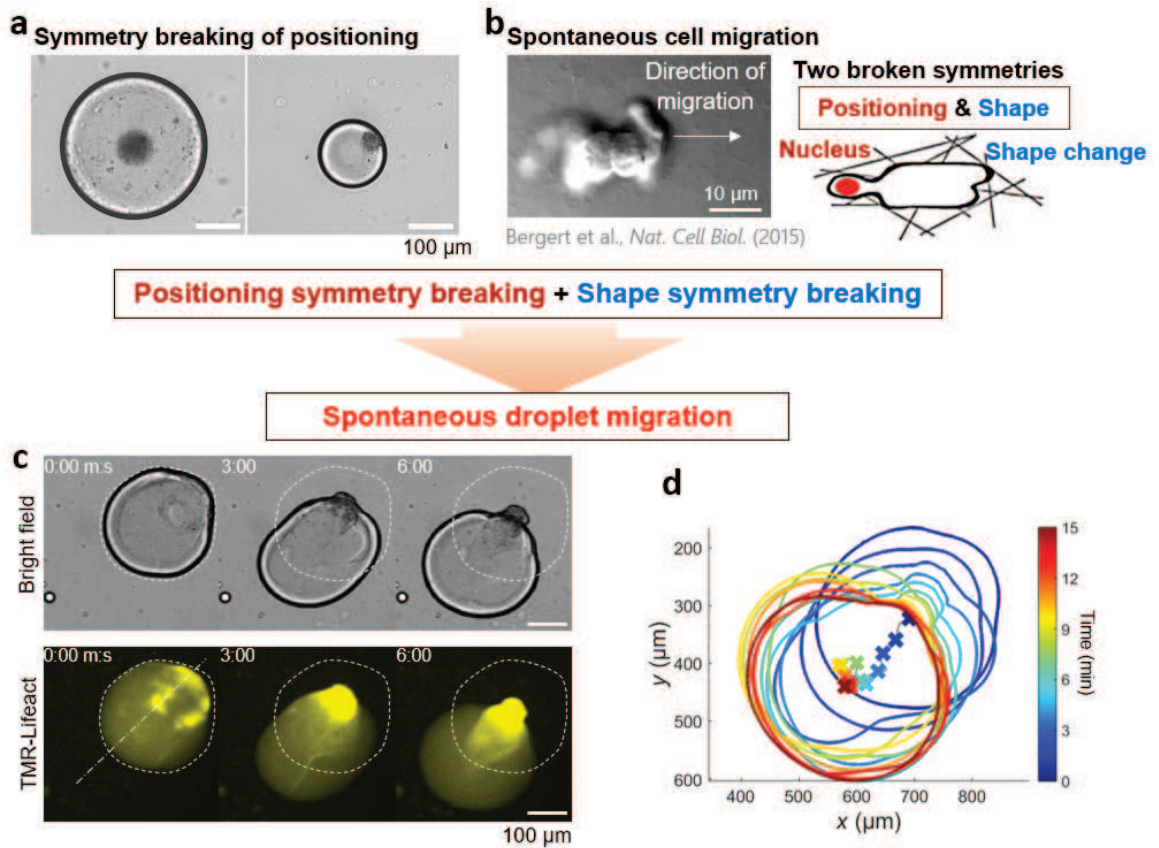
Figure 3.4: (**a**) Symmetry breaking of the positioning studied in Chapter 2. (**b**) Representative image of the spontaneous cell migration through 3D confined spaces (collagen gel). The migrating cell has the two kinds of broken symmetries, nucleus positioning and the shape changes. (**c**) Time-lapse images showing the spontaneous droplet migration in which both the positioning symmetry breaking and the shape symmetry breaking were implemented. (**d**) The droplet outline was superimposed. Time is color-coded. Images were adopted from [13].

3.2 Materials & Methods

3.2.1 Experimental setup

Encapsulation of extracts in droplets. Droplets were generated using the method described in Chapter 2. Here, 0.4 μL of the extracts were injected into 20 μL of a lipid-oil mixture: 1 mM L-α-phosphatidylcholine from egg yolk (eggPC) (27554-01; Nacalai Tesque) in mineral oil (M5904; Sigma-Aldrich) for control, and 14% L-α-Phosphatidyl-D-myo-inositol-4,5-bisphosphate (PIP$_2$) (524644; Merck) in 1 mM eggPC in mineral oil for actin-membrane binding. The DGS-NTA(Ni) (790404; Avanti Polar Lipids) was mixed with 1 mM eggPC in mineral oil with a mole fraction of 7.6% for experiments using 200 nM His-α-actinin and 10% for experiments using 10 nM His-VVCA. Before injecting the extracts, the lipid-oil mixtures were incubated on ice for more than 5 min. By tapping the sample tube with a finger, we obtained extracts-in-oil droplets of various sizes. Immediately after emulsification, 3-7 μL of the emulsion was placed on a PDMS-coated glass slide and gently covered with a PDMS-coated coverslip on top. The chamber height was controlled by the spacer thickness.

Preparation of the lipid-oil mixture

1. Mix PIP$_2$ 25 μL with eggPC 25 μL at mole fraction of 14% PIP$_2$ in a 1.5 mL PCR tube.

2. Incubate the PIP$_2$-eggPC mixture in vacuum overnight.

3. Add 160 μL mineral oil (M5904; Sigma-Aldrich) to prepare f. 1mM PIP$_2$-eggPC-oil mixture.

4. Incubate the tube on a heat block at 80°C for 10 min.

5. Shake the tube using Vortex-Genei2 for more than 5 s.

6. Repeat the procedure 4-5 once again.

7. Sonicate the tube more than 2hrs (ASU-6 ASU CLEANER; AS ONE).

8. Store the tube at $-30°$C.

Measurement of the viscosity of oil   The viscosity of M5904 $\eta_{\text{oil}} = 24.2$ mPa s and low-viscosity oil of $\eta_{\text{oil}} = 14.8$ mPa s prepared by mixing 200 μL of M5904 and 41 μL of hexadecane (080-03685; Nacalai Tesque) were measured using an Ostwald viscometer (ϕ 0.75 mm) (2-8190-02; AS ONE) at 20°C in a heat bath.

Magnetic manipulation of actomyosin network.   First, 300 μL of magnetic beads (S1420S, Streptavidin Magnetic Beads; BioLabs) (diameter $=1$ μm, 4 mg mL^{-1}) were added to a 1.5-mL tube, and the supernatants were removed while pulling the magnetic beads using a neodymium magnet. The remaining magnetic beads were washed with 300 μL of A50 buffer (50 mM HEPES-KOH pH 7.6, 50 mM KCl, 5 mM MgCl$_2$, and 1 mM EGTA) containing 1 mM DTT, and the supernatants were removed while pulling the magnetic beads using a neodymium magnet. The A50 buffer did not affect actomyosin activity [111]. The washing process was repeated three times. After removing the supernatants, 50 μL of A50 buffer was added (f. 24 mg mL^{-1}). Before emulsification, 0.4 μL of the magnetic beads were added to the extracts, which was in turn accumulated by the contracted actomyosin gel. The position of the actomyosin gel entangled with magnetic beads was controlled by an external magnetic field by placing the neodymium magnet next to the observation chamber. For image acquisition to compare the migration speed of polarized actomyosin droplets with and without actin-membrane binding, polarization was initially built by a magnetic force in the actomyosin droplet. Thereafter, the magnet was removed, and time-lapse images were acquired. For image acquisition of the actomyosin droplet recovering the migration capacity by magnetic force-induced polarization, the magnet was kept next

to the observation chamber. The chamber height was 100 μm for all the data.

Force transmission microscopy. First, 2 μL of fluorescently-labeled silica beads (silicastar-greenF, 42-00-103; Corefront) (diameter =1 μm, 50 mg mL^{-1}) were mixed with 98 μL of DI water (Fig. 3.5). The solution was centrifuged at 15,000 rpm for 5 min. The supernatant was removed by pipette aspiration, and the residual bead suspension was dried to evaporate the residual DI water on a heat block at 37°C for 20 min. After completely drying the beads, 100 μL of mineral oil (M5904; Sigma-Aldrich) was added to the beads, and the resulting 1 mg mL^{-1} beads-oil mixture was sonicated for 20 min for resuspension. Next, a flow cell with a height of 100 μm was constructed using PDMS-coated glass slides and non-coated coverslips. The chamber height was controlled using double-sided spacer tapes. To place the beads on the bottom PDMS-coated glass surface, a 15 μL bead-oil mixture was injected into the flow cell. The flow cell was incubated for 30 min to allow sedimentation of the beads. After incubation, the top coverslips were gently removed. The excess amount of the bead-oil mixture was absorbed by a paper. Finally, actomyosin droplets were placed on the bead-covered PDMS-coated glass slides and gently sealed with a PDMS-coated coverslip on top. The chamber height was 100 μm for all the data.

Encapsulation of the extracts in annulus 1D microchannel. The PDMS microchamber was prepared as explained in Chapter 2. Briefly, chromium masks (MITANI micronics) were used to print patterns on SU-8 3025 photoresist (MicroChem) spin-coated on a silicon wafer using a mask aligner (MA-100; MIKASA). The molds of the PDMS microwells were constructed on the surface of the silicon wafers. The PDMS elastomer was poured onto the mold and cured at 75°C for 1 h. The patterned PDMS chamber was gently removed from the mold. The depth of the microwells was measured using a laser scanning surface profiler (LT-9000; Keyence). The chamber was stored in DI water overnight in a fridge to hydrate. After placing 3-7 μL of the
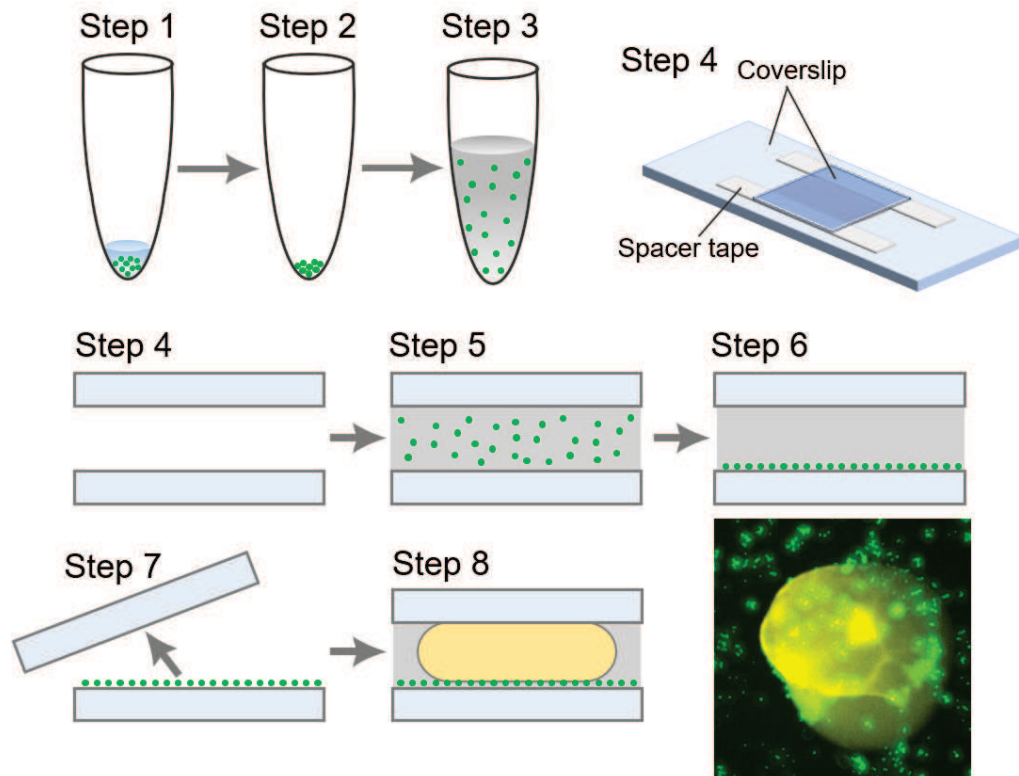
Figure 3.5: Preparation procedure of the force transmission microscopy. (**Step 1**) Centrifuge the fluorescent beads. (**Step 2**) Evaporate the residual solution. (**Step 3**) Add mineral oil and sonicate the tube to disperse the beads. (**Step 4**) Construct a flow cell chamber, where the side view of the flow cell is shown. (**Step 5**) Inject the beads-oil mixture into the flow cell. (**Step 6**) Incubate the chamber at R.T. for 10 min for beads to sediment. (**Step 7**) Remove the top coverslip and absorb the excess oil. (**Step 8**) Put the extracts-in-oil droplets on the beads carpet and gently cover the flow cell by the PDMS-coated coverslip. The right image is taken by the epi-fluorescence microscopy.

emulsion on a PDMS-coated glass slide, the PDMS chamber was gently placed on top of the emulsion droplets. We chose this quasi-1D geometry of the annulus microchannel because the straight 1D channel with inlet and outlet disturbed the initial polarization and induced unexpected drift flows.

3.2.2 Image analysis

Microscopy. Time-lapse images were acquired every 6 s using an epifluorescence microscope (IX73; Olympus) equipped with ×10 objective lens (U Plan WD 10×/0.25;

Meiji Techno Japan) or ×20 objective lens (TU Plan ELWD 20×/0.40; Nikon), a cooled CMOS camera (Neo5.5; Andor Technology), and a stable excitation light source (XLED1; Lumen Dynamics). The contact area between the droplet and substrate was recorded using a confocal microscope (IX73; Olympus) and a confocal scanning unit (CSU-X1; Yokogawa Electric Cor. Ltd.) equipped with iXon-Ultra EM-CCD camera (Andor Technologies) under a 488 nm fluorescence channel. For all microscopic examinations, the sample temperature was maintained at $20\pm1°$C, using a custom-made heat block connected to a water bath circulator and controlling the room temperature.

Image analysis. Quantitative image analysis was performed using a custom code written in MATLAB as explained in Chapter 2. The center of mass of each droplet was detected through the binarization of bright-field images. To determine the radius R and diameter $D = 2R$ of the droplets, the area of each droplet S was extracted and then calculated from $R = \sqrt{S/\pi}$. The aspect ratio of the droplet with $h > D$ was set to $h/D = 1$. The droplet speed was calculated from the straight displacement of the droplet centroid from the initial position to the final position divided by the track duration. The migration speed of the droplets under 2D confinement was calculated from the displacement within 10 min. The migration speed of the droplets under the 1D microchannel was calculated from the displacement within 5 min. The contact angle used for the calculation of $f(\theta)$ was estimated from the droplets confined under 1D annulus microchannels by linear fitting of the binarized image at the contact point (Fig. 3.19). Quantification of the speed of actin flow was performed by producing kymographs of the fluorescence images. To extract the position of the beads in force transmission microscopy, particle tracking analysis was performed using the Fiji plugin TrackMate [99] (https://imagej.net/TrackMate).

3.3   Results

3.3.1   Experiment I: Effects of actin-membrane binding

Extracts-in-oil droplets were prepared on ice and immediately confined between PDMS-coated glass slides in the same way as in Chapter 2 (Fig. 3.6a). Here, to mimic the living migratory cells, we used the actin-binding lipids, PIP2, which is known to recruit F-actin crosslinker α-actinin and Arp2/3 activating VCA domain [100, 101, 102]. Notably, F-actin is localized at the droplet periphery using PIP2, forming a cell-like cortex (Fig. 3.6b,c).

A few seconds later, the initially polymerized actin network started to contract toward the center of the droplet without actin-membrane binding, consistent with the result in Chapter 2 (Fig. 3.7a). In contrast, with actin-membrane binding, a part of the actin-membrane binding is broken and subsequently, the entire actomyosin networks were contracted toward the facing periphery, leading to the formation of cell-like polarity (Fig. 3.7b). To quantify the extent of the polarity, we calculated the asymmetry parameter Φ_{asym} which is defined as the distance between the droplet centroid and the center-of-mass of the distributed F-actin, normalized by the length of the long-axis of the droplet (Fig. 3.7c). Without actin-membrane binding, asymmetry parameter remained close to $\Phi_{asym} \simeq 0$, while with actin-membrane binding, asymmetry parameter sharply rose to $\Phi_{asym} \simeq 0.5$ and reached a plateau (Fig. 3.7d).
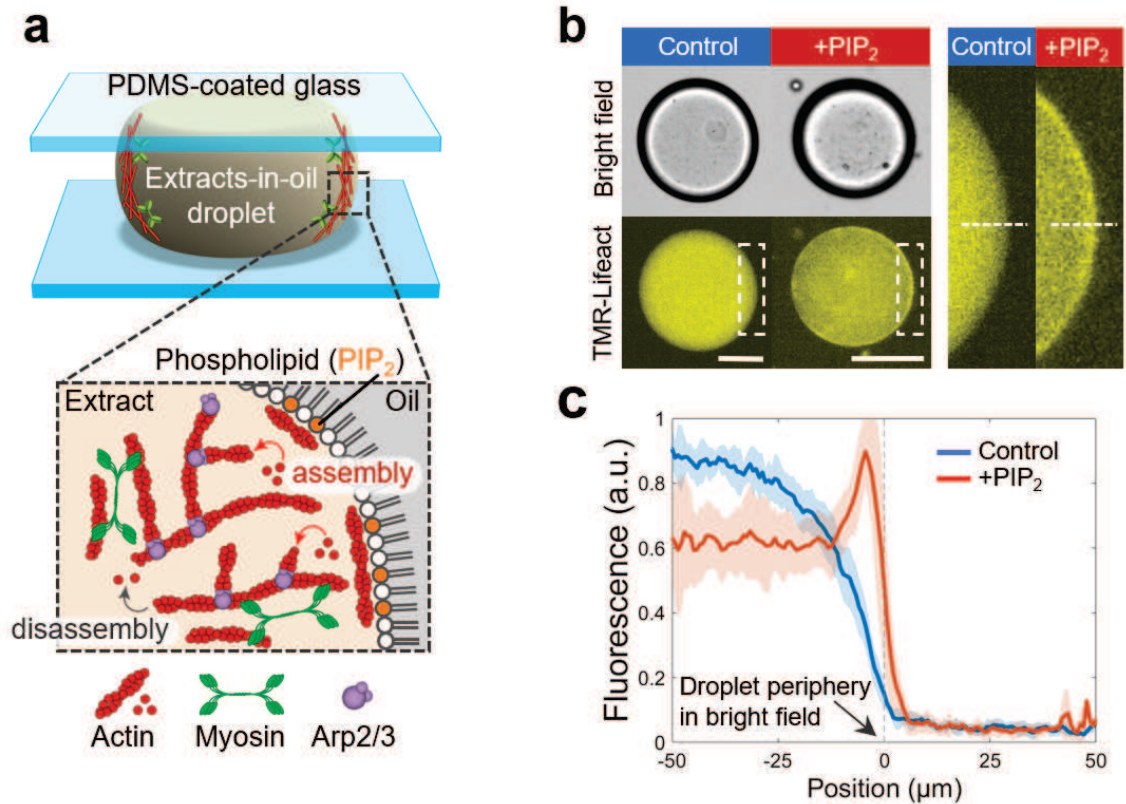
Figure 3.6: (**a**) Schematic of the experimental setup. Extracts-in-oil droplets were confined between PDMS-coated glass slides. F-actin is bound to the lipid monolayer interface depending on the composition of the phospholipids (i.e., PIP_2). (**b**) Snapshots of extracts-in-oil droplets showing PIP_2 dependent localization of F-actin at the droplet surface. (Right) Membrane interface within white dashed boxes is magnified. (**c**) Spatial profiles of F-actin fluorescence across the membrane interface along the dashed lines in (b) in control (blue) and with PIP_2 (red). Data are mean $\pm$ SD. All images were taken by epi-fluorescence microscopy. Scale bars, 100 μm.
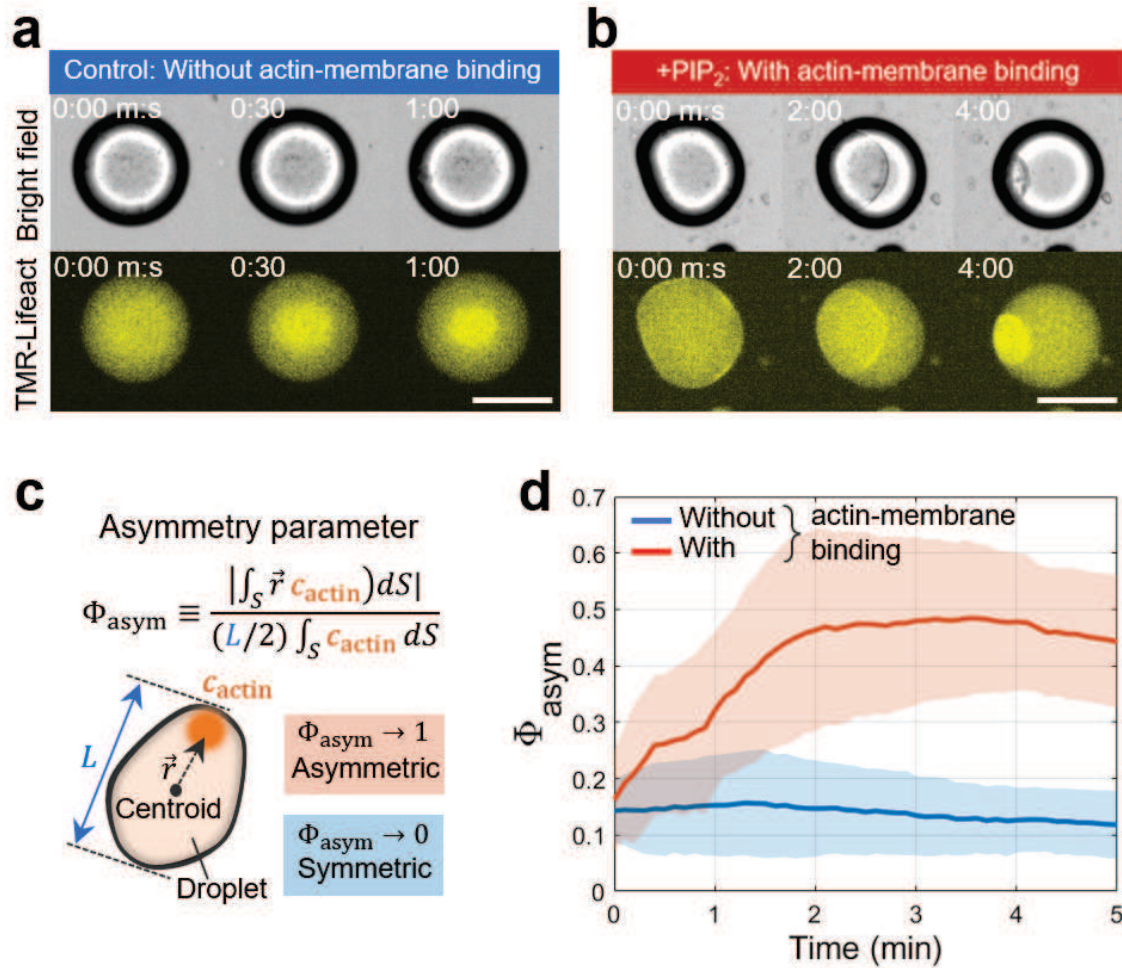
Figure 3.7: (**a** and **b**) Time sequence of actomyosin contraction. (**a**) Actomyosin contraction without actin-membrane binding (control). (**b**) Actomyosin contraction with actin-membrane binding (+PIP$_2$). (**c**) Asymmetry parameter Φ_{asym} is defined as the center of mass of the F-actin distribution inside the droplet S, normalized by the length of the droplet long-axis L. (**g**) Time evolution of Φ_{asym} without actin-membrane binding (blue) and with actin-membrane binding (red). Data are mean $\pm$ SD. All images were taken by epi-fluorescence microscopy. Scale bars, 100 μm.

Surprisingly, immediately after the polarization of the actomyosin networks, the droplet started to migrate in the direction of the polarity, accompanied by the dynamic shape changes (Fig. 3.8a,b). The actin flow was propagating from the front to the rear part of the migrating droplet, suggesting that the actin flow is key to droplet migration (Fig. 3.8c). The F-actin was highly accumulated in the rear part of the droplet, where the droplet was significantly deformed, suggesting that there is

a contractile force gradient that sustains the polarized actin flow. We confirmed that either the localization of actin-crosslinking protein α-actinin (Fig. 3.9a) or Arp2/3 activating VVCA domain of human N-WASP (Fig. 3.9b) also enabled the droplet migration, indicating that the physical interaction between the actin flow and the lipid membrane is the key factor to generate the propulsion force.
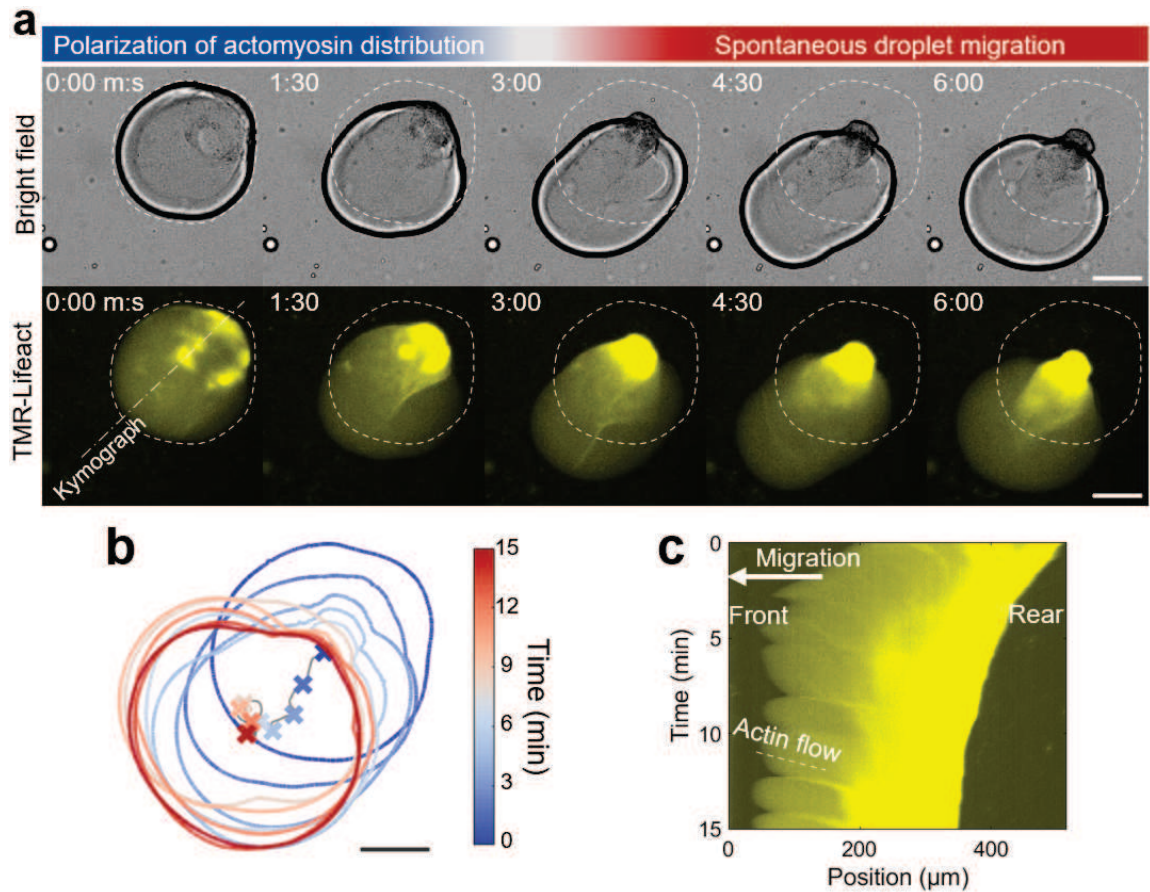
Figure 3.8: (**a**) Time sequence of the polarization of actomyosin distribution and the following droplet migration under the height of 60 μm chamber. The white dashed lines represent the initial droplet outlines. (**b**) Droplet boundary analyzed from (a). Time is color-coded. (**c**) Kymograph measured along the dotted broken line in (a). All images were taken by epi-fluorescence microscopy. Scale bars, 100 μm.
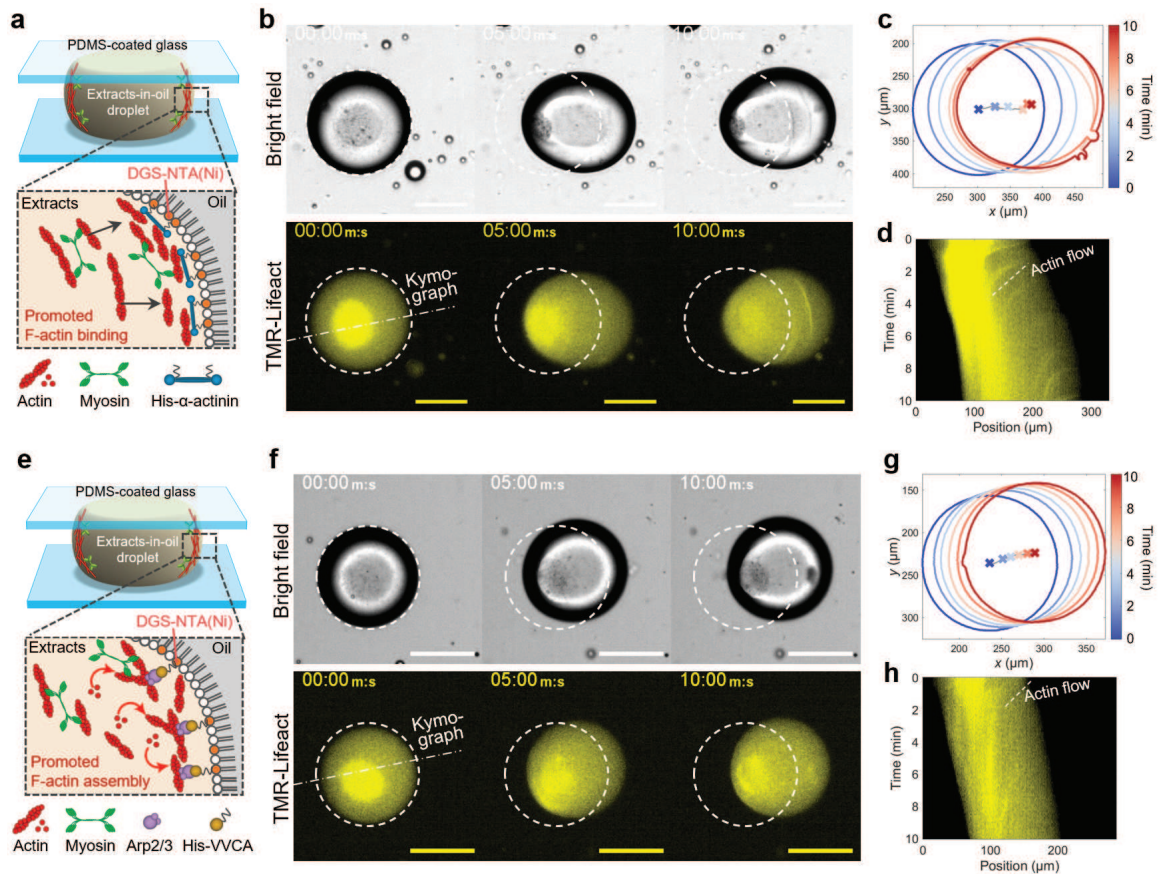
Figure 3.9: To mimic the local increase in F-actin density at the droplet interface, either the F-actin crosslinker His-α-actinin or Arp2/3 activating domain His-VVCA was localized at the droplet interface via DGS-NTA(Ni) lipids. (**a**) Schematic of the recruitment of His-α-actinin at the droplet interface via DGS-NTA(Ni). (**b**) Time sequence of the droplet migration under the height of 100 μm chamber. The white dashed lines represent the initial outline of the droplet. (**c**) Droplet boundary analyzed from (b). (**d**) Kymograph measured along the broken line in (b). (**e**) Schematic of the recruitment of His-VVCA at the droplet interface via DGS-NTA(Ni). (**f**) Time sequence of a droplet migration under the height of 100 μm chamber. The white dashed lines represent the initial outline of the droplet. (**g**) Droplet boundary analyzed from (f). (**h**) Kymograph measured along the broken line in (f). All images were taken by epi-fluorescence microscopy. Scale bars, 100 μm
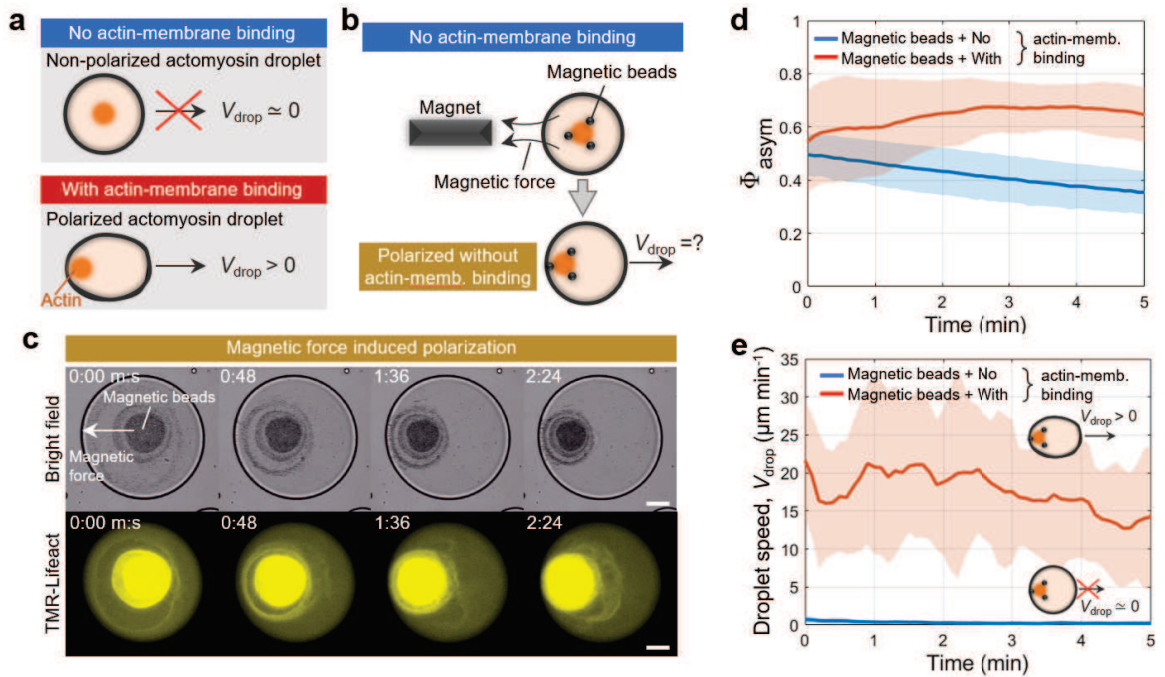
Figure 3.10: (**a**) Schematic summarizing the effect of actin-membrane binding on polarity and migration speed V_{drop}. (**b**) Schematic of the magnetic force-induced polarization. Polarization is induced by applying the magnetic force on magnetic beads entangled with the actomyosin networks. (**c**) Time sequence of magnetic force-induced polarization. (**d**) The asymmetry parameter without actin-membrane binding (blue) and with actin-membrane binding (red). Data are mean $\pm$ SD. (**e**) Droplet speed after polarity induction without actin membrane binding (blue) and with actin-membrane binding (red). Data are mean $\pm$ SD. All images were taken by epi-fluorescence microscopy. Scale bars, 100 μm.

3.3.2 Experiment II: The role of polarization

We showed that the polarized droplets with actin-membrane binding could migrate, while the non-polarized droplet without actin-membrane binding could not migrate (Fig. 3.10a). Because the polarization is coupled with the actin-membrane binding, it is unclear whether the polarization is a sufficient condition for the droplet migration. To dissect the physical role of the polarization of the actomyosin network from the actin-membrane binding, here we used the magnetic manipulation of the polarization of the actomyosin network (Fig. 3.10b). Dispersed magnetic beads in the extracts were initially accumulated by the contracting actomyosin network, and the position of such gel-like structure containing magnetic beads was manipulated by the external
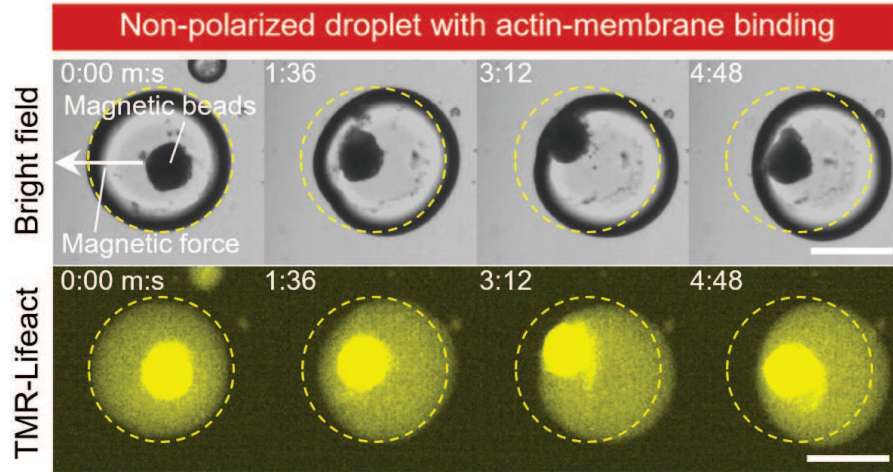
Figure 3.11: Time-lapse images showing the droplet with actin-membrane binding that initially had no polarity started to migrate after magnetic force-induced polarization. The white dashed lines represent the initial droplet outlines. All images were taken by epi-fluorescence microscopy. Scale bars, 100 μm.

magnetic force (Fig. 3.10c). The polarization of the actomyosin network was initially built, then the magnetic force was turned off and the time-lapse images were started to be taken. On the one hand, initially built polarization was comparable between droplets with and without actin-membrane binding ($\Phi_{\text{asym}} \simeq 0.53$ for with actin-membrane binding, $\Phi_{\text{asym}} \simeq 0.53$ for without actin-membrane binding) (Fig. 3.10d). On the other hand, only the polarized droplets with actin-membrane binding showed a clear migratory behavior ($V_{\text{drop}} \simeq 1.15$ μm min^{-1} with actin-membrane binding, where droplet speed V_{drop} were averaged for 5 min) (Fig. 3.10e). Moreover, non-polarized droplets recovered their migration capacity after the magnetic force-induced polarization (Fig. 3.11). These results indicate that the polarization of the actomyosin network alone is not sufficient to drive the droplet migration, but the actin-membrane binding plays a crucial role in propulsion force generation.
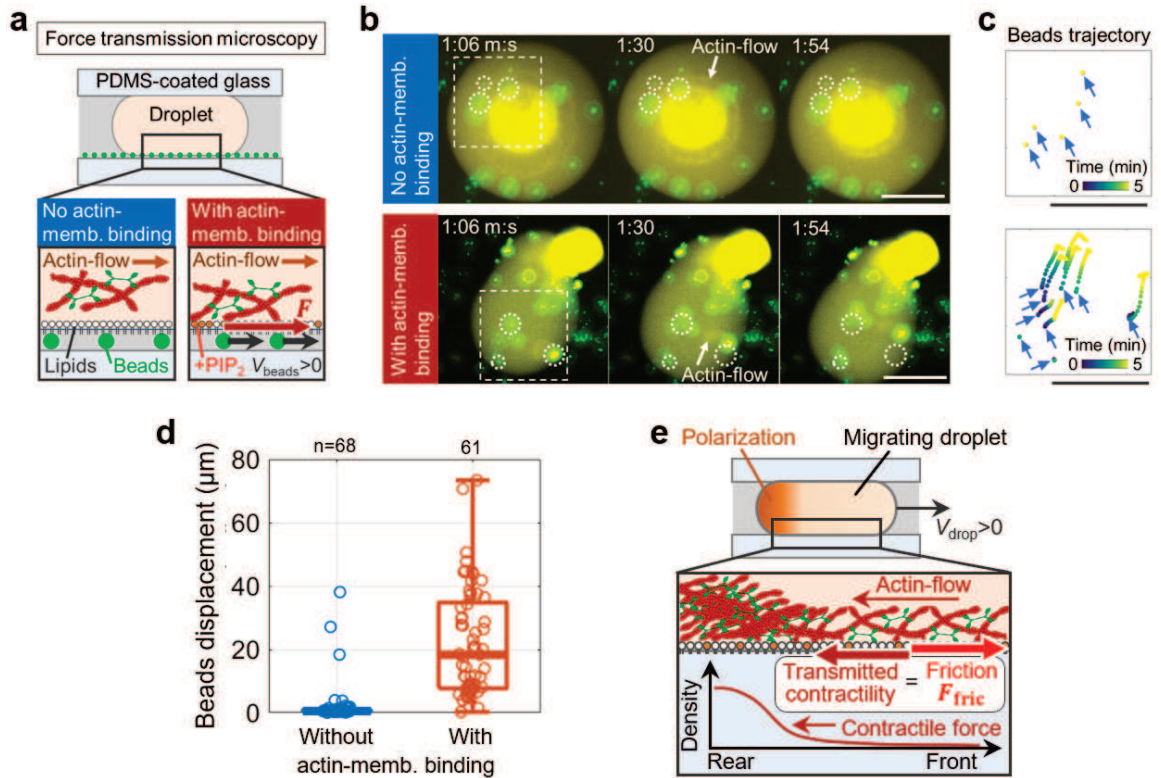
Figure 3.12: (**a**) Schematic of the force transmission microscopy. Beads are displaced by the actin flow when the contractile force of actin flow $\boldsymbol{F}$ is transmitted to the bottom substrate. (**b**) Time sequence of beads transport by actin flow without actin-membrane binding (top) and with actin-membrane binding (bottom). The white dotted circles represent the initial position of the beads. (**c**) Beads within the white dashed boxes in (b) were tracked. Initial beads positions are indicated by blue arrows. The chamber height was 100 μm. (**d**) Beads displacement for 5 min without actin-membrane binding (n=68 beads under 6 droplets, in blue) and with actin-membrane binding (n=61 beads under 10 droplets, in red) (Mann-Whitney U-test, $p < 0.001$). (**e**) Schematic showing the droplet migration mechanism. Polarized actomyosin sustains the rearward actin flow, where the contractile force of the actin flow is transmitted to the substrate via actin-membrane binding, by which the counteracting friction force is generated. All images were taken by epifluorescence microscopy. Scale bars, 100 μm.

3.3.3 Experiment III: The role of actin-membrane binding

To understand the physical role of actin-membrane binding in propulsion force generation, we performed friction force microscopy inspired by Abercrombie's seminal study on cell migration [103]. First, fluorescent tracer beads were placed on the bot-

tom substrate, thereafter droplets were placed on this beads carpet (Fig. 3.12a). We reasoned that if the contractile force of actin flow is transmitted from the droplets to the external substrate, the external beads in contact with the droplets can be moved with the actin flow. In fact, without actin-membrane binding, we found that the beads were not moved with the actin flow, while the beads were moved with the actin flow in the presence of actin-membrane binding (Fig. 3.12b,c). Beads displacement for 5 min shows the clear difference (Fig. 3.12d). This result indicates that physical interaction between the actin flow and the lipid membrane can generate friction force at the membrane-substrate contact area, by which the propulsion force is generated, showing the key physical role of actin-membrane binding on the force transmission (Fig. 3.12e).

3.3.4 Experiment IV: The role of confinement on droplet migration

Force transmission microscopy suggested that the friction force is key to driving the droplet migration, indicating that the physical contact of the droplet with the substrate could modulate the droplet speed. To test this hypothesis, we compared the migration speed with and without the substrate confinement (Fig. 3.13a). On the one hand, without actin-membrane binding, both the confined and unconfined droplets did not migrate as expected (Fig. 3.13b, left). On the other hand, with actin-membrane binding, the confined droplets migrated ~4 times faster than the unconfined droplets (Fig. 3.13b, right).

To further characterize the migration behavior, we calculated the mean-square displacement (MSD) of the droplets with actin-membrane binding. Notably, confined droplets showed ballistic motion, while the unconfined droplets showed diffusive motion (Fig. 3.13c). To understand the origin of the distinct migration behavior, we compared the angle distribution of the trajectory of the droplet centroid and
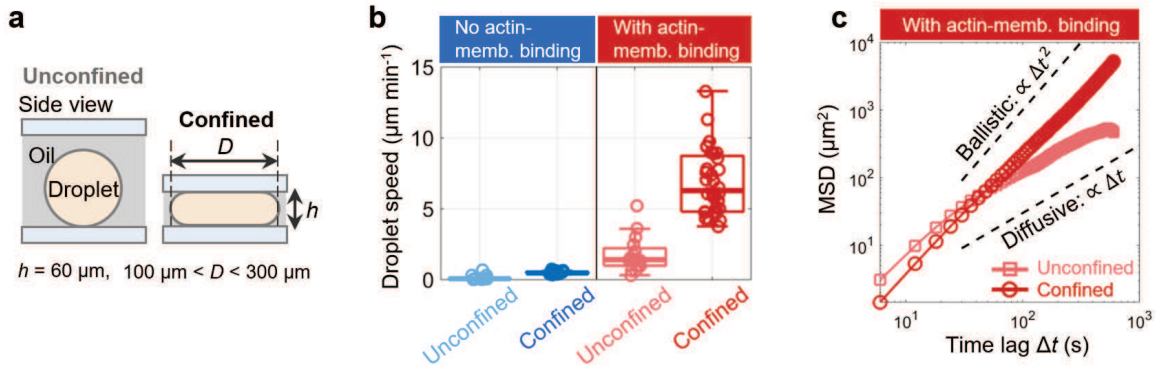
Figure 3.13: (**a**) Schematic showing unconfined and confined droplets. Droplets of diameter within $100 < D < 300$ μm were analyzed at the chamber height of $h = 60$ μm. (**b**) Average droplet speed for 10 min without actin-membrane binding for unconfined (n=22, in light blue) and confined droplets (n=17, in blue), and with actin-membrane binding for unconfined (n=16, in light red) and confined droplets (n=32, in red). (**c**) Mean-square displacement (MSD) of droplet centroids with actin-membrane binding for unconfined (n=16, in light red) and confined droplets (n=32, in red).

the droplet polarity. Here, the droplet polarity is defined as the direction from the center-of-mass of the F-actin distribution to the droplet centroid (Fig. 3.14a). On the one hand, the angle of the droplet trajectory was randomly distributed for unconfined droplets, while that of confined droplets were much less fluctuated (Fig. 3.14b). Auto-correlation of the angle of the trajectory showed the correlation time of $\tau = 40$ s for unconfined droplets and $\tau = 400$ s for confined droplets, consistent with the MSD (Fig. 3.14c). On the other hand, the angle fluctuation of the droplet polarity was not significant in both cases for confined and unconfined droplets (Fig. 3.14b), where auto-correlation time was comparable in both cases: $\tau = 400$ s for unconfined and $\tau = 500$ for confined droplets (Fig. 3.14d). Moreover, the cross-correlation between droplet trajectory angle and the droplet polarity angle showed that the droplet polarity was decoupled from the droplet trajectory for unconfined droplets (cross-correlation ~ 0), while the droplet polarity was coupled with the droplet trajectory for confined droplets (cross-correlation ~ 0.5) (Fig. 3.14e). These results suggested that the substrate confinement not only transmits the contractile force of actin flow

to the substrate but also plays an important role to guide the migration direction along with the droplet polarity.
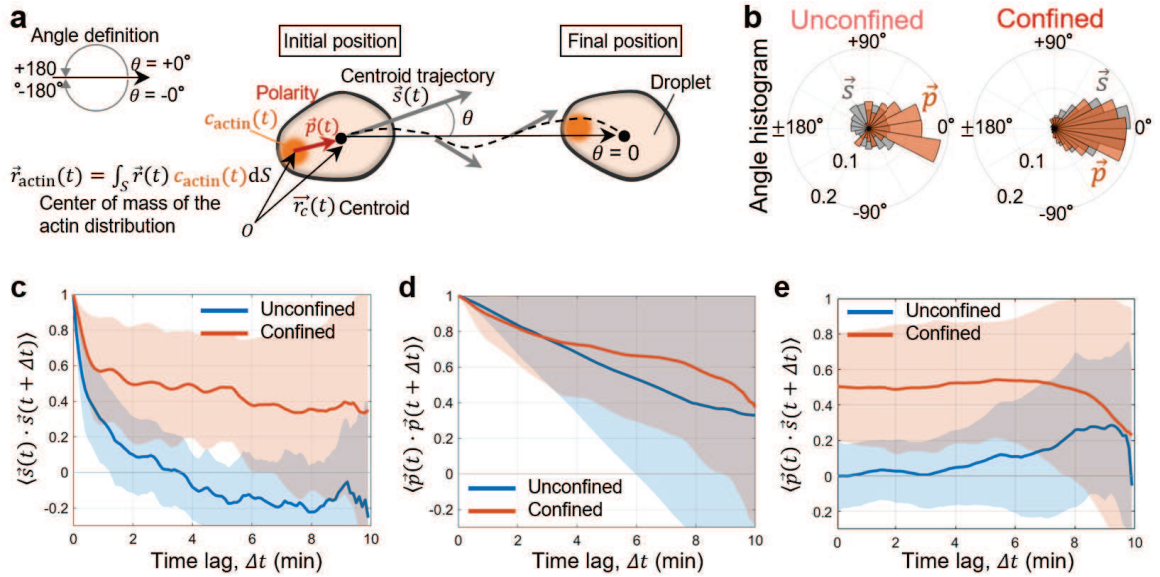
Figure 3.14: (**a**) The definition of the centroid tragectory $\vec{s}$ and the polarity of the droplet $\vec{p}$, where the vectors are normalized to unity. Polarity of the droplet is defined as the direction from the center of mass of F-actin to the droplet centroid. The angle of the trajectory vector and the angle of the polarity vector were measured from the straight line drawn from the initial to the final droplet position. (**b**) Angle probability of the trajectory ($\vec{s}$, in gray) and polarity ($\vec{p}$, in orange) for unconfined (n=16, left) and confined droplets (n=32, right). (**c**) Autocorrelation of the trajectory vector. Least-square fitting was performed by an exponential function $\exp(-\Delta t/\tau_c)$, where τ_c is the correlation time. This yielded $\tau_c = 51$ s for unconfined droplets and $\tau_c = 432$ s for confined droplets. (**d**) Autocorrelation of the polarity vector. Least-square fitting yielded $\tau_c = 547$ s for unconfined droplets and $\tau_c = 818$ s for confined droplets. (**e**) Cross-correlation between the trajectory vector and the polarity vector.

3.3.5 Conceptual model: Force balance between active friction and passive fluid drag

Based on the above results, here we provide the model of droplet migration. Considering a droplet confined between the substrates migrating along with its polarity axis (Fig. 3.15a). With actin-membrane binding, polymerized actomyosin network forms a gel beneath the lipid membrane. Because of the contractile force gradient from the front to the rear part of the droplet, the actomyosin network is contracted toward the rear part of the droplet, during which the physical interaction between the actin flow and the membrane exerts shear stress on the external substrate. Because of the force balance across this interface, the external friction force was applied to the droplet $F_{\text{fric}}^{\text{contact}}$ in the opposite direction to the actin flow. In contrast, friction force was not generated at the lateral extracts-oil interface due to the much large viscosity of the actomyosin gel than the viscous oil ($\eta_{\text{oil}}/\eta_{\text{act}} \ll 1$ [13, 104]). Therefore, the droplet migration is driven by the active friction force generated at the top and bottom contact area, while the droplet experiences the passive fluid drag F_{drag} from the surrounding viscous oil. Thus, force balance across the droplet surface can be written as

$$F_{\text{fric}}^{\text{contact}} + F_{\text{drag}} = 0, \tag{3.1}$$

by which the droplet migration speed is determined.

In the first place, one might expect that the droplets migrate faster under the stronger confinement, because the larger contact area would increase the active friction $F_{\text{fric}}^{\text{contact}} \propto \pi R_{\text{c}}^2$. However, Stokes' hydrodynamics dictates that the viscous drag is increased under stronger confinement as $F_{\text{drag}} \propto \eta_{\text{oil}} \nabla v_{\text{oil}}$. Therefore, examining such confinement geometry dependence of the droplet migration speed is key to understanding the mechanism of the actomyosin-based migration in confined spaces.
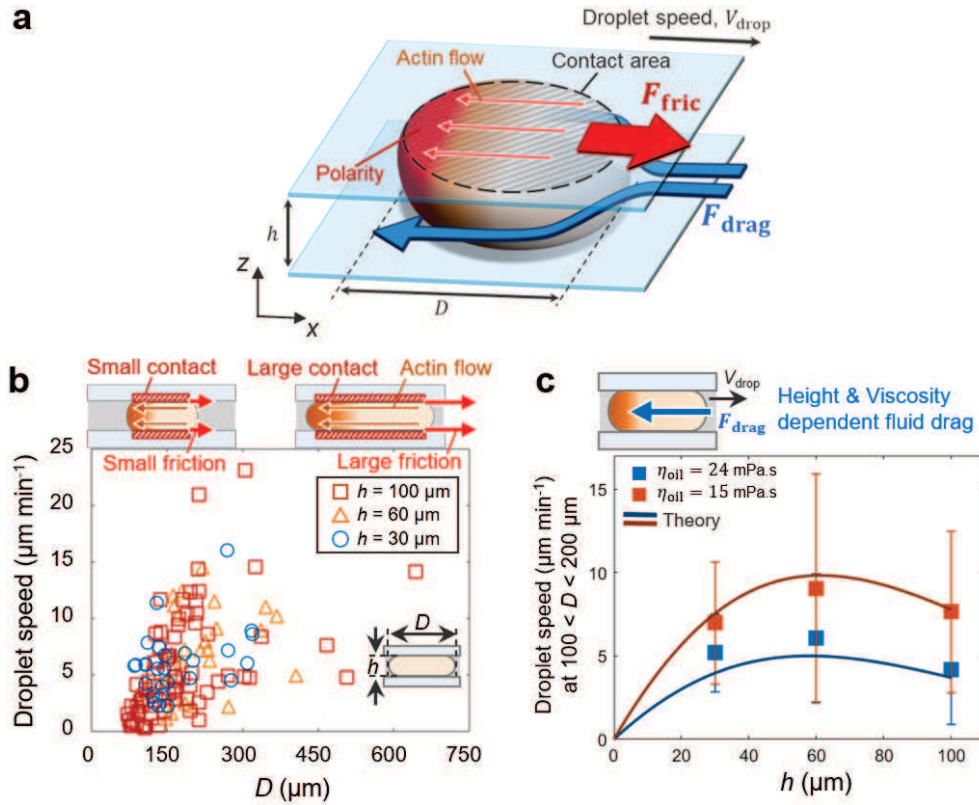
Figure 3.15: (**a**) Schematic summarizing the forces applied to the droplet during migration. Given that a droplet of diameter D with migration speed V_{drop} is confined under 2D confinement of height h, which is propelled by the active friction F_{fric} induced by actin flow and the droplet experiences passive drag force F_{drag} from the surrounding oil. (**b**) Droplet size dependence of the migration speed under $h = 30$ μm (blue circles), $h = 60$ μm (yellow triangles), and $h = 100$ μm (red squares). (**c**) Height dependence of the averaged droplet speed between $100 \leq D \leq 200$ μm under high viscosity oil ($\eta_{\mathrm{oil}} = 24$ mPa s, in blue) and low viscosity oil ($\eta_{\mathrm{oil}} = 15$ mPa s, in orange). Data are mean $\pm$ SD. Solid lines correspond to the theoretical model Eq. (3.2) plotted with using averaged droplet diameter $D \simeq 140$ μm for $\eta_{\mathrm{oil}} = 24$ mPa s and $D \simeq 148$ μm for $\eta_{\mathrm{oil}} = 15$ mPa s.

3.3.6 Experiment V: Effect of geometry on migration speed

To examine how confinement geometry influences the migration speed, we first changed the droplet diameter D in the range of $80 < D < 350$ μm. We found that the droplet speed is increased with the larger droplet diameter in any chamber height at $h = 30, 60, 100$ μm, consistent with the theoretical prediction (Fig. 3.15b). Next, we examined the confinement height dependence of the droplet speed by averaging the droplet speed within diameter $100 \leq D \leq 200$. Notably, droplet speed had a
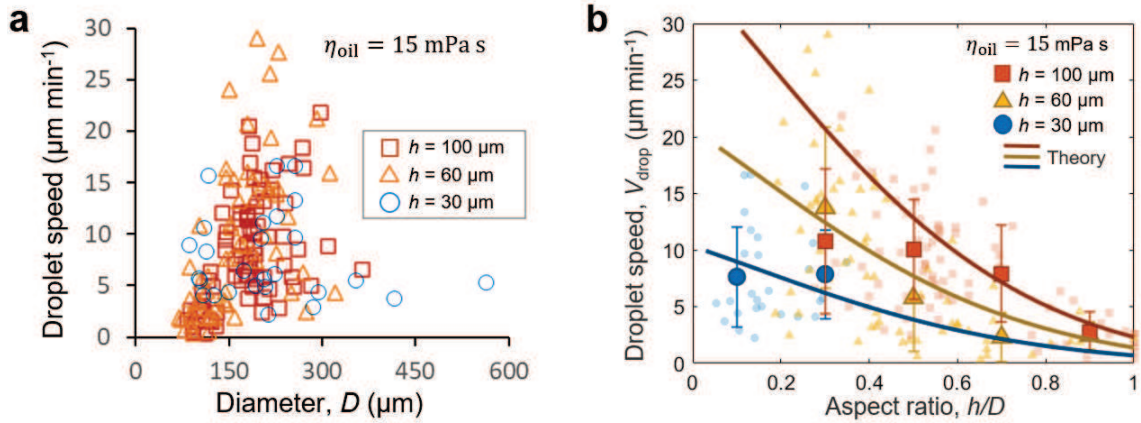
Figure 3.16: (**a**) Scatter plot of the droplet migration speed versus its diameter D in $h = 30$ μm (n=27, blue circles), $h = 60$ μm (n=65, yellow triangles), and $h = 100$ μm (n=78, red squares) under low viscosity oil ($\eta_{\mathrm{oil}} = 15$ mPa s). (**b**) Aspect ratio h/D dependence of the migration speed under low viscosity oil ($\eta_{\mathrm{oil}} = 15$ mPa s). The scatter plot shows individual data for $h = 30$ μm (n=27, blue circles), $h = 60$ μm (n=65, yellow triangles), and $h = 100$ μm (n=78, red squares), and larger symbols show binned averaged data with mean $\pm$ SD. Solid lines correspond to the theoretical model Eq. (3.2).

peak at $h = 60$ μm, indicating that there is a geometric competition between active friction and fluid drag (Fig. 3.15c). We confirmed the influence of the fluid drag by decreasing the surrounding oil viscosity from $\eta_{\mathrm{oil}} = 24$ mPa s to $\eta_{\mathrm{oil}} = 15$ mPa s, which was resulted in the faster droplet migration (Fig. 3.15c and Fig. 3.16). Note that the geometry dependence of the actin flow speed was not significant, and it was not correlated with the droplet speed (Fig. 3.17), suggesting that the geometry dependence of the droplet speed is originated from the change in the substrate contact, not from the variation of the actin flow speed.
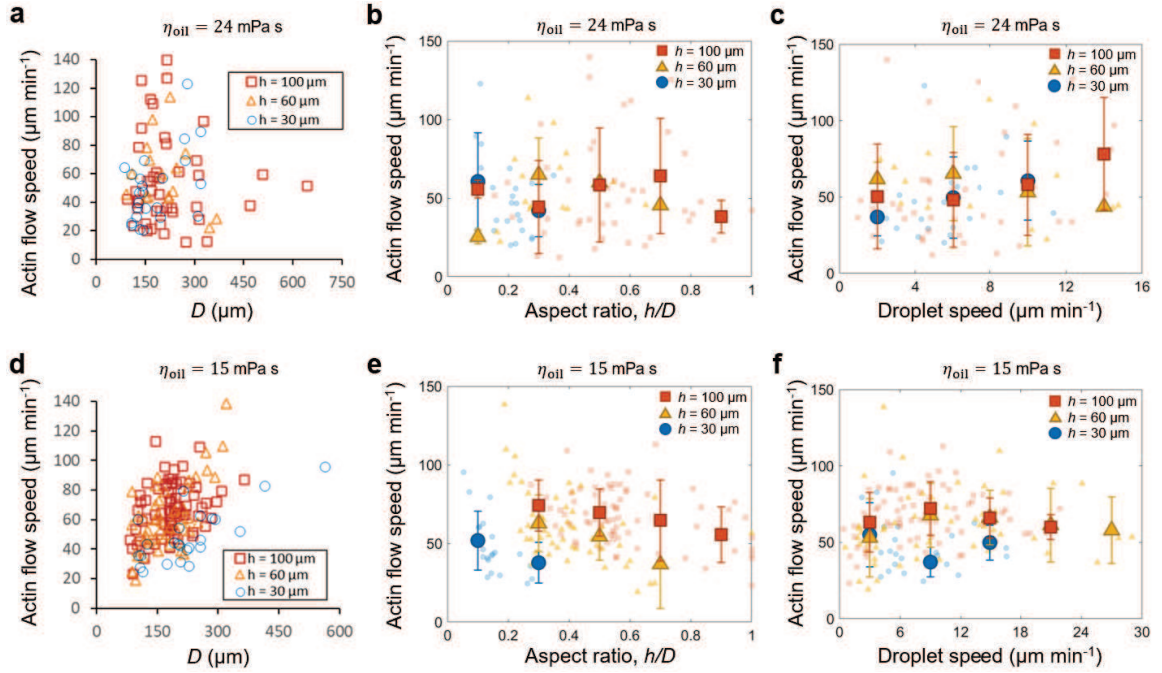
Figure 3.17: (**a-c**) Scatter plots of actin flow speed with surrounding oil viscosity $\eta_{\text{oil}} = 24$ mPa s. (**a**) Scatter plot of actin flow speed versus diameter D of actomyosin droplets in $h = 30$ μm (n=24, blue circles), $h = 60$ μm (n=16, yellow triangles), and $h = 100$ μm (n=42, red squares). (**b**) Scatter plot of actin flow speed versus aspect ratio of the droplet h/D. (**c**) Scatter plot of actin flow speed versus droplet speed. The larger symbols represent binned averaged data with mean $\pm$ SD. (**d-f**) Scatter plots of actin flow speed with surrounding oil viscosity $\eta_{\text{oil}} = 15$ mPa s. (**d**) Scatter plot of actin flow speed versus diameter D of actomyosin droplets in $h = 30$ μm (n=24, blue circles), $h = 60$ μm (n=53, yellow triangles), and $h = 100$ μm (n=74, red squares). (**e**) Scatter plot of actin flow speed versus aspect ratio of the droplet h/D. (**f**) Scatter plot of actin flow speed versus droplet speed. The larger symbols represent binned averaged data with mean $\pm$ SD.
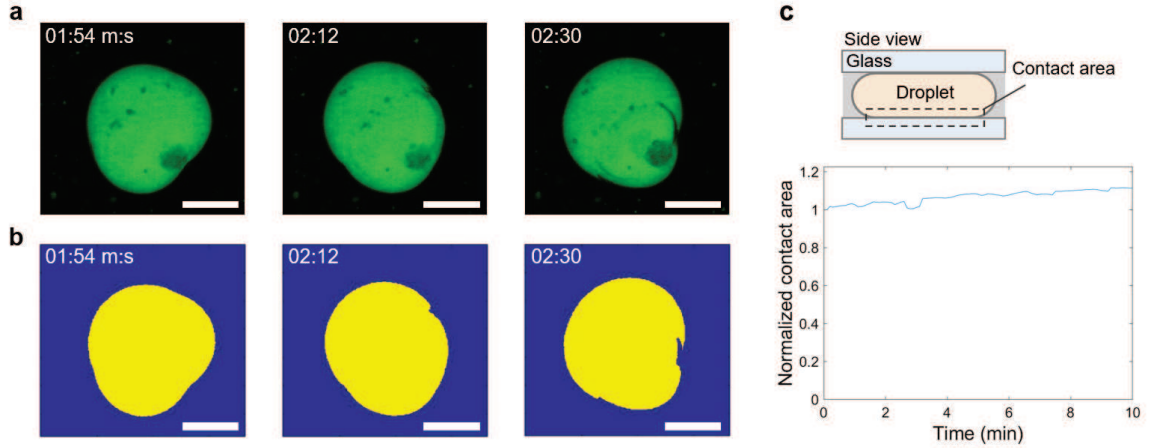
Figure 3.18: (**a**) Time sequence of the actomyosin droplet containing purified GFP as a volume marker. Confocal microscopy was performed to focus on the contact area between the droplet and substrate. The height of the chamber was 60 μm. (**b**) The contact area (yellow colored area) was analyzed from the confocal images after binarization. (**c**) The time evolution of the contact area between the droplet and the substrate, normalized by its value at 0 min. The contact area of the droplet remained mostly constant over 10 min. Scale bars, 100 μm.

3.3.7 Theory I: Geometry dependent migration model

To understand the physical mechanism of such geometry dependence of the migration speed, we devised a theoretical model. We consider a droplet migrating in the direction of the polarity (Fig. 3.15a). For simplicity, the droplet shape is assumed to be a circle, while the result was not significantly affected by the asymmetry of the droplet shape because the ratio of the droplet long-axis to short-axis was ~0.87 (Fig. 3.22). We assumed that the droplet shape is unchanged over the migration, which was confirmed by confocal microscopy (Fig. 3.18).

In the presence of actin-membrane binding, the physical interaction between the contracting actomyosin network and the lipid membrane creates shear stress $\sigma_{\mathrm{act}} = \alpha v_{\mathrm{act}}$ at the droplet-substrate interface, where α is friction coefficient and v_{act} is the speed of the actin flow. As a result, the counter-acting active friction force $F_{\mathrm{act}}^{\mathrm{contact}}$ was exerted on the droplet, by which the droplet migrate forward by balancing with the passive fluid drag F_{drag}.
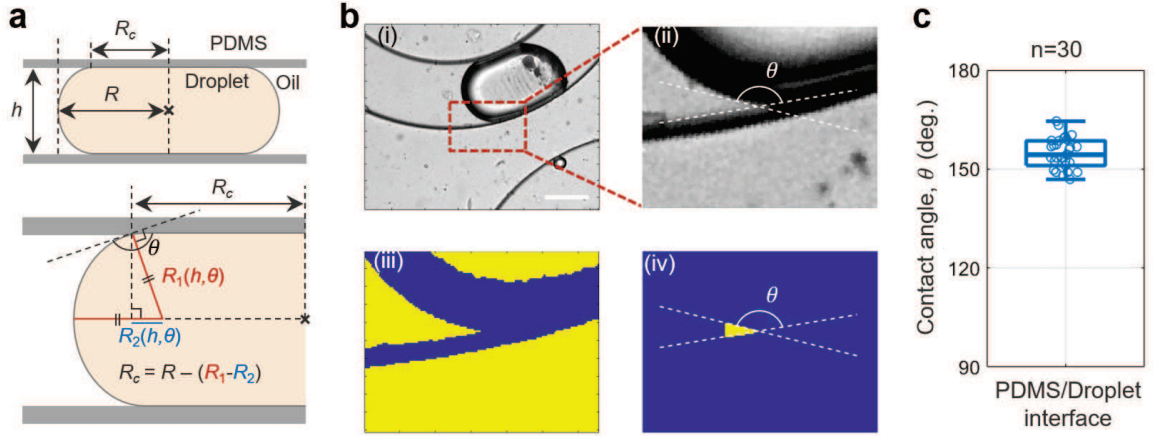
Figure 3.19: (**a**) Schematic of a confined droplet, where contact angle θ was used to calculate contact radius $R_{\rm c} = R - (h/2)f(\theta)$, $f(\theta) = -(|\tan\theta| + 1/\cos\theta)$. (**b**) Procedure of contact angle measurement. Using the droplet confined in PDMS microchannels, contact angle between PDMS and droplet interface was analyzed. (i, ii): The contact point is cropped from the front side of the droplet to avoid the local deformation at the rear induced by actomyosin contractility. (iii) The image was binarized and the tip of the contact angle was cropped. (iv) Contact angle was measured from the angle between two lines that were drawn by performing a linear fitting for the sides of the triangle. (**c**) Boxplot showing the contact angle between PDMS and droplet interface (n=30 contact points, $\theta = 154.7 \pm 4.5$ deg., mean $\pm$ SD). All images were taken by epifluorescence microscopy. Scale bar, 100 μm.

In this situation, we calculated the confinement geometry dependence of the droplet speed $V_{\rm drop}$ using the force balance Eq. (3.1). The total active friction is given by integrating the $\sigma_{\rm act}$ over the contact area, thus $F_{\rm fric}^{\rm contact} = -2\int_{\pi R_{\rm c}^2}(\alpha v_{\rm act}){\rm d}S \simeq -2(\alpha v_{\rm act})\pi R_{\rm c}^2$, where $R_{\rm c} \equiv R - (h/2)f(\theta)$ is the contact radius, R is the droplet radius, $f(\theta) = -(|\tan\theta| + (1/\cos\theta))$ is the geometric constant, and the $\theta = 154.7°$ is the contact angle at the droplet-substrate interface. To calculate the contact area, the contact angle was measured by confining the droplet in PDMS microchannels (Fig. 3.19). The fluid drag is given by $F_{\rm drag} \simeq \eta_{\rm oil}\nabla^2 v_{\rm oil}(\pi R^2 h) \sim \eta_{\rm oil}[(D/2)^{-2} + (h/2)^{-2}]V_{\rm drop}[\pi(D/2)^2 h]$, this is because the velocity gradient of the surrounding fluid across both the radial direction of the droplet and the vertical direction of the chamber height controbute to viscous dissipation [105]. Thus, using the force balance Eq.
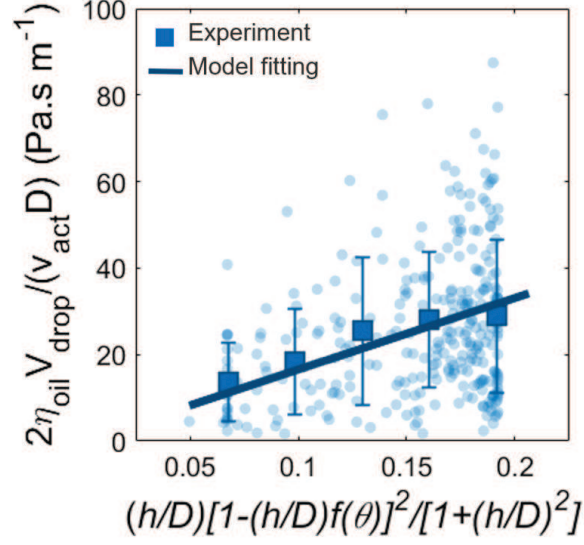
Figure 3.20: Geometric scaling of Eq. (3.2). The scatter plot shows individual data (n=305), and squares show binned averaged data with mean $\pm$ SD. The solid lines show the linear fitting to the experimental data, which yielded $\alpha = 1.7 \times 10^2$ Pa s m^{-1}.

(3.1), the migration speed is given by

$$V_{\text{drop}} = \frac{\alpha v_{\text{act}}}{2\eta_{\text{oil}}} h \left(1 + \left(\frac{h}{D}\right)^2\right)^{-1} \left(1 - \frac{h}{D} f(\theta)\right)^2. \tag{3.2}$$

To obtain the geometry-independent friction coefficient α, we scaled the droplet speed to $2\eta_{\text{oil}} V_{\text{drop}}/(v_{\text{act}} D)$ using $\eta_{\text{oil}} = 24$ mPa s with $v_{\text{act}} \simeq 54$ μm min^{-1} and $\eta_{\text{oil}} = 15$ mPa s with $v_{\text{act}} \simeq 62$ μm min^{-1} (Fig. 3.17). This geometric scaling was observed in the experimental data and the linear fitting yielded $\alpha = 1.7 \times 10^2$ Pa s m^{-1} (Fig. 3.20). We estimated the friction stress $F_{\text{fric}}^{\text{contact}}/(2\pi R_c^2) \simeq \alpha v_{\text{act}} \simeq 0.16$ mPa, which is several times smaller than the friction stress $\gtrsim 1$ mPa of migrating cells in confined spaces [13]. This might be because of the weaker actin-membrane binding than the living cells, or lower F-actin density compared to the actomyosin cortex of living cells. Notably, using only one obtained parameter α, this model reproduced the geometric dependence of the droplet speed well (Fig. 3.15c, Fig. 3.16b, and Fig. 3.21).

We can now explain how the migration speed is determined by the confinement
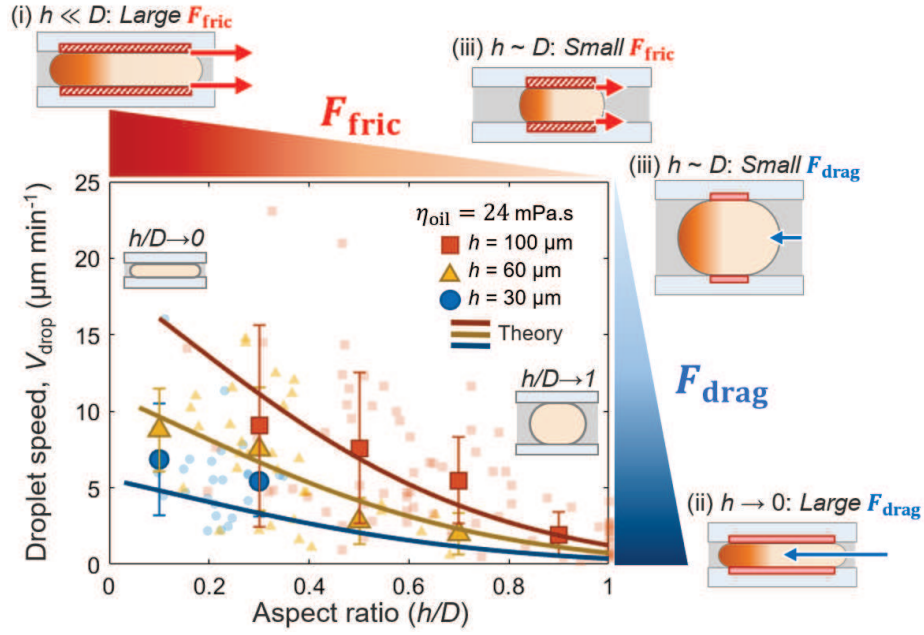
Figure 3.21: Aspect ratio h/D dependence of the migration speed under high viscosity oil ($\eta_{\text{oil}} = 24$ mPa s). The scatter plot shows individual data for $h = 30$ μm (n=27, blue circles), $h = 60$ μm (n=32, yellow triangles), and $h = 100$ μm (n=77, red squares), and larger symbols show binned averaged data with mean $\pm$ SD. Solid lines correspond to the theoretical model Eq. (3.2).

geometry, namely the aspect ratio h/D of the droplet (Fig. 3.21). The droplet shape is close to a pancake for the small aspect ratio close to 0, while the droplet shape is close to a sphere for the aspect ratio close to 1. On the one hand, with a fixed chamber height, the larger droplet has a larger contact area, thus the larger friction outweighs the increase in the fluid drag, leading to the faster droplet migration ((i) $h \ll D$). On the other hand, given that a droplet with a fixed volume $\pi R^2 h = $ const., active friction scales as $F_{\text{fric}}^{\text{contact}} \sim h^{-1}$, while the fluid drag scales as $F_{\text{drag}} \sim h^{-2}$. Thus, as the chamber height becomes smaller, the increase in the fluid drag outweighs the active friction, leading to the slower droplet migration ((ii) $h \to 0$). Conversely, as the aspect ratio approaches 1, although the fluid drag decreases, the active friction is inevitably decreased due to the smaller contact area between the droplet and the substrate, leading to the smaller droplet migration ((iii) $h \sim D$). Together, these results provide physical constraints on the actomyosin-based motility under confined

environments, which is governed by the geometric trade-off between the active friction and the fluid drag.

3.3.8 Theory II: The influence of the asymmetric shape on migration speed

Here, we examine the contribution of the asymmetric droplet shape to migration. We assume that the asymmetric droplet shape is an ellipse with a minor axis length D_1 and major axis length D_2, which is a reasonable approximation according to the experiment (Fig. 3.22a). For the analytical calculation, the droplet shape is assumed to be constant over time, in other words, the symmetricity $\beta \equiv D_1/D_2$ is a constant. We also assume that the symmetricity is constant for droplets of any size, $\beta \sim 0.87$ (Fig. 3.22b). The main difference from the symmetric case of the droplet with diameter D is that the larger the droplet deformation, the smaller drag force is exerted from the surrounding oil. This is qualitatively expected from the geometric dependence of the drag force, $F_{\text{drag}}^{\text{symm}} \sim \eta_{\text{oil}} \nabla^2 v_{\text{oil}} (\pi R^2 h) \sim \eta_{\text{oil}}[(D/2)^{-2} + (h/2)^{-2}]V_{\text{drop}}[\pi(D/2)^2 h] = \eta_{\text{oil}}[1 + (D/h)^2]V_{\text{drop}}(\pi h)$. In an extreme case in which the long axis D_2 is much larger than the short axis D_1, the viscous dissipation is dominated by the front and rear side of the droplet, thus $F_{\text{drag}}^{\text{symm}}$ is rewritten as $F_{\text{drag}}^{\text{asym}} \sim \eta_{\text{oil}} \nabla^2 v_{\text{oil}}[\pi(D_1/2)^2 h] \sim \eta_{\text{oil}}[(D_1/2)^{-2} + (h/2)^{-2}]V_{\text{drop}}[\pi(D_1/2)^2 h] = \eta_{\text{oil}}[1 + (D_1/h)^2] \times V_{\text{drop}}(\pi h)$, where the minor axis length is smaller than the symmetric droplet radius, $D_1 < D$ [105].

By using the force balance across the droplet interface, Eq. (3.1), the migration speed of the asymmetric droplet is given by

$$V_{\text{drop}} = \frac{\alpha v_{\text{act}}}{\beta \eta_{\text{oil}}} h \left(1 + \left(\frac{h}{\beta D_2}\right)^2\right)^{-1} \left(1 - \frac{h}{\beta D_2} f(\theta)\right) \left(1 - \frac{h}{D_2} f(\theta)\right), \qquad (3.3)$$

where the definitions of the parameters are the same as in the symmetric droplet case.
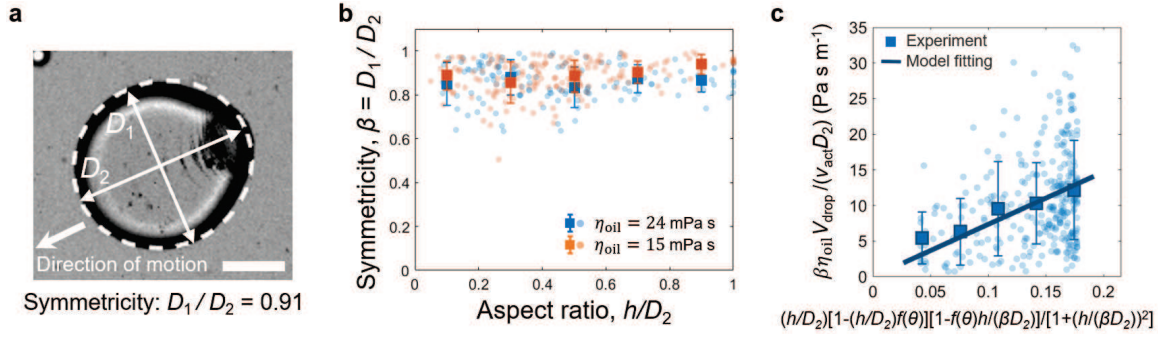
Figure 3.22: (**a**) The droplet shape is not a perfect circle because accumulated acto-myosin at the trailing edge exerts surface tension on the droplet interface. The ellipse approximates well the droplet shape, so we performed ellipsoidal fitting to the droplet shape with the minor axis length D_1 and the major axis length D_2. We quantified the symmetricity of the droplet, defined as the ratio of the minor axis length over the major axis length, $\beta = D_1/D_2$. The symmetricity of the droplet displayed in the image is 0.91. (**b**) Aspect ratio h/D_2 dependence of the symmetricity, where h is the chamber height. The symmetricity averaged over all the droplets is $D_1/D_2 \simeq 0.87$, showing that the droplet shape is close to a circle. (**c**) Geometric scaling of Eq. (3.3). The scatter plot shows individual data (n=305), and squares show binned averaged data with mean $\pm$ SD. The solid line shows the linear fitting to the experimental data, which yielded $\alpha = 0.7 \times 10^2$ Pa s m^{-1}. The image was taken by epifluorescence microscopy. Scale bar, 100 μm.

This geometric scaling relation can be observed in the experiments, where a linear fitting yielded $\alpha = 0.7 \times 10^2$ Pa s m^{-1} (Fig. 3.22c). By using the averaged actin flow velocity $v_{\text{act}} \simeq 58$ μm min^{-1}, we find the friction stress $\alpha v_{\text{act}} \simeq 0.07$ mPa, which is comparable to the symmetric case.

3.3.9   Experiment VI: Migration in 1D channel

Finally, we confined the droplets in a 1D microchannel to dissect the effect of active friction from the fluid drag, where we can increase the contact area without changing the channel width (Fig. 3.23a). We designed the quasi-1D PDMS microchannel which was put on the extracts-in-oil droplets, where the shape change of the droplet was suppressed due to the complete contact with the channel wall. Notably, actomyosin droplets can migrate through such a 1D microchannel, suggesting that the active friction is an effective way to enable actomyosin-based migration in strongly confined spaces (Fig. 3.23b,c). To see the geometry dependence of the migration speed, we varied the channel width at $w = 100$ μm and $w = 150$ μm with a fixed channel height of $h = 60$ μm, and the major axis length of the droplets L from 125 μm to 520 μm, by which the migration speed varied from 2.6 μm min^{-1} to 12.9 μm min^{-1} (Fig. 3.23d,e). We confirmed that the droplet speed did not significantly correlate with either the confinement geometry or the actin flow speed (Fig. 3.24). The theoretical fitting of the geometric scaling yielded the friction stress $\alpha v_{\mathrm{act}} \simeq 0.26$ mPa (Fig. 3.25a). Thus, active friction-driven migration provides the same extent of propulsion force in both 1D and 2D confinement. The migration speed was ~1.8 times larger for longer droplets at a smaller aspect ratio, suggesting that the larger contact area contributes to a larger total active friction (Fig. 3.25b).
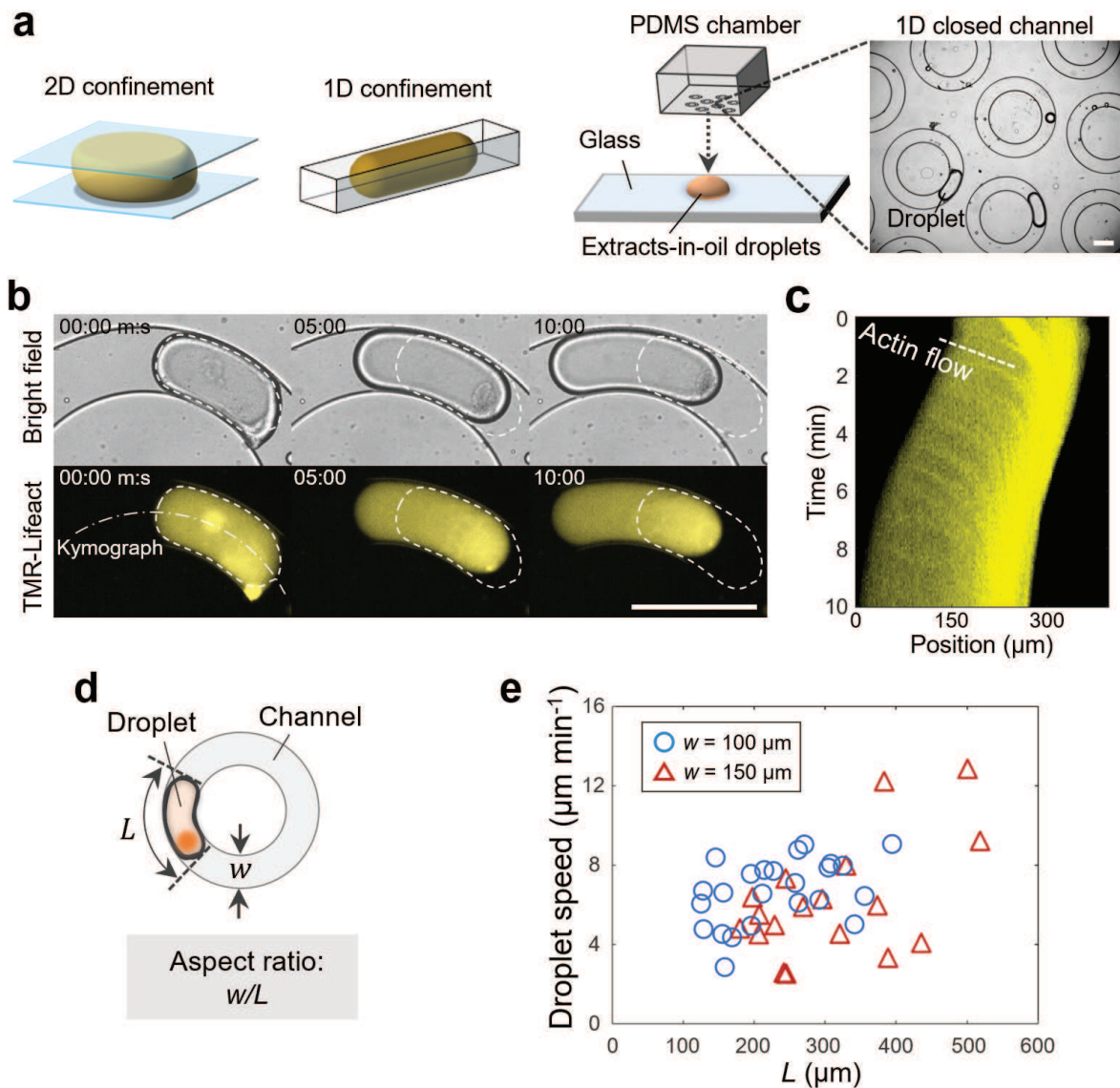
Figure 3.23: (**a**) Schematic showing 2D and 1D confinement with experimental setup. The 1D closed channel patterns are designed at the PDMS chamber (Methods), which is placed onto extracts-in-oil droplets. The zoom-in view shows a representative image of droplets confined in 1D closed channels. (**b**) Time sequence of a droplet migration under 1D confinement with channel width of 100 μm and height of 60 μm. The white dashed lines represent the initial outlines of the droplet. (**c**) Kymograph of the actin flow extracted from the white dotted broken line in (b). (**d**) Schematic showing the channel geometry defined by the width w, and the major axis length of the droplet is L. Channel height is fixed as 60 μm. (**e**) Droplet length dependence of the droplet speed under $w = 100$ μm (n=24, blue circles), $w = 150$ μm (n=18, red triangles). All images were taken by epifluorescence microscopy. Scale bars, 200 μm.

3.3.10 Theory III: Physical model of droplet migration in a 1D closed chamber

Here, we provide a simple description of droplet migration under the 1D closed mi-crochannel. In the experiment, we used the annulus microchannel of height h, width w, where the migrating droplet of length L was fully confined in contact with the channel wall. To derive an analytical expression, we assume that the shape of the chamber is cylindrical with radius a and calculate the fluid flow under 1D geome-try for the sake of simplicity because the scope of our interest is geometric scaling with L. First, because of the incompressibility of fluids, droplet motion with speed V_{drop} induces the oil flow with mean velocity $\bar{v}_{\mathrm{oil}} \sim V_{\mathrm{drop}}$ around the droplet. Given the cylindrical channel shape, the motion of the droplet creates a Hagen-Poiseuille flow of the oil in the chamber with the velocity averaged over the cross-section $\bar{v}_{\mathrm{oil}} = (a^2/8\eta_{\mathrm{oil}})|\partial p/\partial x|$, where p is the pressure driving the fluid flow, and the x-axis is the direction of the flow. Because of the continuity of the pressure across the droplet interface, the fluid around the droplet has a pressure same as the inside the droplet, which is driven by the friction force averaged over the cross-sectional area, $f_{\mathrm{fric}} = F_{\mathrm{fric}}/(\pi a^2)$. Thus, the pressure gradient that drives the fluid flow is approxi-mated as $|\partial p/\partial x| \sim f_{\mathrm{fric}}/L$. The active friction force is calculated by integration over the contact area, $f_{\mathrm{fric}} = -\alpha v_{\mathrm{act}}(2L/a)(1 - 2af(\theta)/L)$. The force balance condition on the droplet can be written as $F_{\mathrm{fric}} + F_{\mathrm{drag}} = 0$, which is obtained from the Hagen-Poiseuille law by defining the passive drag force in the channel as $F_{\mathrm{drag}} \equiv -\xi V_{\mathrm{drop}}$, where $\xi = 8\pi\eta_{\mathrm{oil}}L$ is the effective drag coefficient in the 1D closed microchannel. Therefore, the droplet speed under the 1D microchannel can be written as:

$$V_{\mathrm{drop}} = \frac{\alpha v_{\mathrm{act}}}{8\eta_{\mathrm{oil}}} 2a \left(1 - \frac{2a}{L} f(\theta) \right). \tag{3.4}$$

To compare the theoretical model with the experiment, we approximately assumed
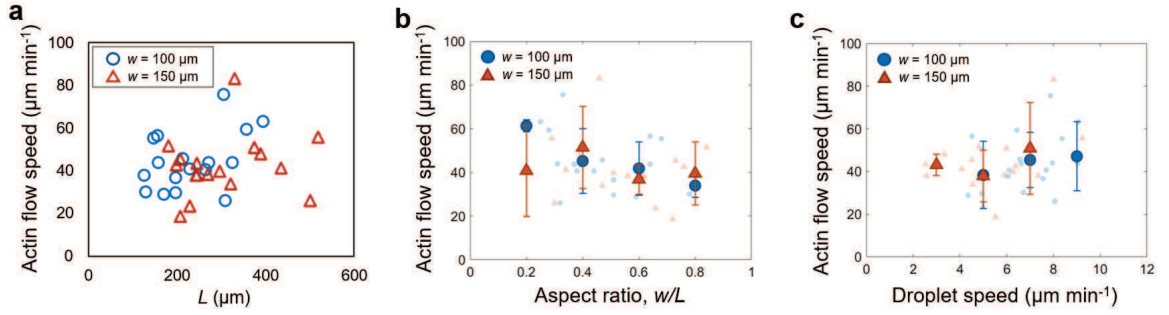
Figure 3.24: (**a**) The droplet length dependence of actin flow speed in $w = 100$ μm (n=17, blue circles) and $w = 100$ μm (n=17, red triangles). (**b**) Actin flow speed in droplets of various aspect ratio under 1D closed channel. The scatter plot shows individual data for $w = 100$ μm (n=17, blue circles) and $w = 150$ μm (n=17, red triangles), and larger symbols show binned averaged data with mean $\pm$ SD. (**c**) Actin flow speed in droplets with various migration speed under 1D closed channel. The scatter plot shows individual data for $w = 100$ μm (n=17, blue circles) and $w = 150$ μm (n=17, red triangles), and larger symbols show binned averaged data with mean $\pm$ SD.

$2a \sim w$. The droplet speed was scaled to $8\eta_{\mathrm{oil}}V_{\mathrm{drop}}/(v_{\mathrm{act}}L)$ using $\eta_{\mathrm{oil}} = 24$ mPa s with $v_{\mathrm{act}} \simeq 43$ μm min^{-1} (Fig. 3.24a). The least-squares fitting of the experimental data (Fig. 3.25a) yields $\alpha = 3.6 \times 10^2$ Pa s m^{-1}, and the aspect ratio dependence of the droplet speed was reproduced by the theoretical model (Fig. 3.25b). By using the actin flow speed $v_{\mathrm{act}} \sim 43$ μm min^{-1} (Fig. 3.24a), we find the friction stress $\alpha v_{\mathrm{act}} \simeq 0.26$ mPa, which is comparable to the 2D migration.
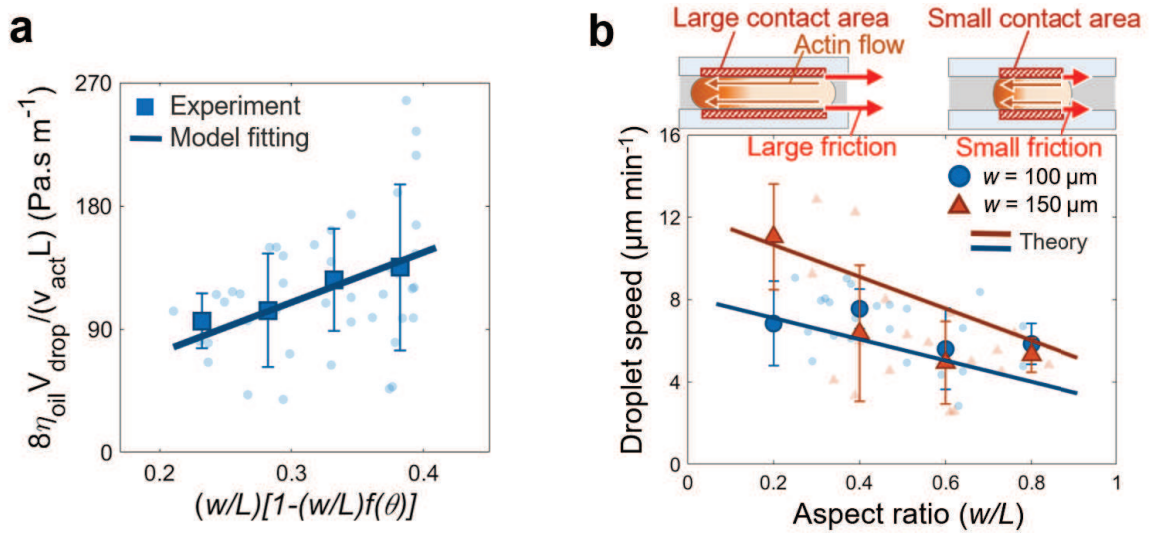
Figure 3.25: (**a**) Geometric scaling of Eq. (3.4). The scatter plot shows individual data (n=42), and squares show binned averaged data with mean $\pm$ SD. The solid lines show the linear fitting to the experimental data, which yielded $\alpha = 3.6 \times 10^2$ Pa s m^{-1}. (**b**) The aspect ratio w/L dependence of droplet speed in 1D closed channel. The scatter plot shows individual data for $w = 100$ μm (n=24, blue circles) and $w = 150$ μm (n=18, red triangles), and larger symbols show binned averaged data with mean $\pm$ SD. Solid lines correspond to the theoretical model. The top schematic illustrates that the larger the contact length, the larger active friction induces a faster droplet speed.

3.4 Discussion

In Chapter 3, we developed the migratory actomyosin droplet by implementing the shape symmetry breaking which expands the positioning symmetry breaking in Chapter 2. The key was the physical interaction between contracting actomyosin networks and the lipid membrane, which realizes both polarization of actomyosin networks and efficient force transmission to the external substrates. Note that previous studies mostly focused on the intracellular self-organization of actomyosin networks, while the present study is the first experimental demonstration of actomyosin-based motility of artificial cells. Therefore, the physical roles of the compartmentalization are expanded from the passive wall to the active functional interface generating the propulsive force.

In living cells, migration onset is triggered by the polarization of the actomyosin network that sustains polarized actin flow, thereafter the friction force generated by the actin flow propels the cell body forward [11, 13]. Notably, we showed that such polarization and force transmission can be achieved by the self-organization of membrane-bound actomyosin networks alone, without the help of biochemical signaling nor specific adhesive proteins [65]. The mechanical interaction between the actin flow and the membrane interface was crucial to establish polarized actomyosin networks as well as generating active friction, by which actomyosin droplets can migrate in a wide range of confined environments from 2D to 1D systems.

Recent studies have shown that substrate friction tunes cell migration speed [13]. However, how the friction force is originated from the actin-membrane interaction and transmitted to the substrates has been poorly understood, because of the complexity of membrane composition, actin-membrane interaction, and transmembrane proteins. Here, by developing an in vitro migratory cell model, we can specify the actin-membrane interaction and the membrane-substrate interaction. Strikingly, our results showed that (i) actin-membrane binding and (ii) substrate contact are sufficient to transmit intracellular contractile forces to the external environments, un-

covering the essential physical factors for efficient force transmission. Note that the strong actin-membrane binding is inherently equipped as dense cortical actomyosin networks in living cells [9], while the cellular environments such as tissues and extracellular matrix are generally confined environments [95, 96], providing sufficient contact with the cell membrane. Thus, the proposed model emphasizes the importance of both intracellular active gel dynamics and physical contact with the substrates that enable efficient force transmission to the external environments.

In addition, the cellular polarity of membrane-associated actomyosin networks is also important for avoiding random cell motility and building persistent directionality [106]. We showed that such directional migration can be achieved by sufficient contact with the substrate. Correlation analysis between the polarity and the trajectory revealed that the migration trajectory was significantly more directed in parallel to the polarity under confined environments. This result suggests that physical contact can transmit intracellular polarity to guide the directed migration. Note that a spontaneous random motion of active droplets using microtubule-kinesin systems was previously reported [107]. Our actomyosin-based migratory droplets will expand such in vitro random motility into directional one, providing a way to extract effective mechanical work from active cytoskeletal systems.

Moreover, we found that the migration speed of actomyosin droplets can be controlled through confinement geometry, namely, it was slower under stronger confinement. The theoretical model suggested that the geometry-dependent balance between active friction and passive fluid drag determines the migration speed. Understanding such fundamental physical limitations in confined spaces will allow us to set the founding ground to control actomyosin-based motility from in vitro models to in vivo situations.

Recent studies have shown that mechanical stress on the nucleus imposed by confinement triggers mechanotransduction and, in turn, contractility was increased

in confined cells [108, 109, 110]. This might be an adaptation strategy of living cells to overcome the large viscous resistance in strongly confined environments. To shed further light on the mechanical roles and self-organization principles of active gels obscured by a rich complexity of living cells, the development of artificial cells that organizes chemo-mechanical coupling would be significant future research.

3.5 Conclusion

Here, we made migratory artificial cells to study how contractile forces are efficiently transmitted to the external substrates under 3D confinement. We found that physical interaction between the actin flow and lipid membrane is key to generating propulsion force, which we called active friction. We uncovered that the geometric balance between active friction and passive fluid drag determines the migration speed regardless of the complexity of the confinement geometry from 1D to 2D environments. Together, not only do these results provide a physical basis of the actomyosin-based motility in cell-sized confined spaces but also this actomyosin droplet opens a new avenue for designing bottom-up strategies to control self-propelled motility in confined spaces ranging from microfluidic engineering to cell biology.

Chapter 4

Rotational Symmetry Breaking of Actin Waves

4.1 Introduction

4.1.1 Pattern formation and symmetry breaking

The symmetry breaking is the basis of the pattern formation in biological systems from fish skin pattern [112] to the oscillatory pattern of Min system observed in bacteria [113, 114]. Such spatial pattern formation via translational symmetry breaking is often observed in reaction-diffusion systems. In reaction-diffusion systems of two species composed of activator and inhibitor system, the symmetry breaking arises from the Turing instability, where the faster inhibitor diffusion stabilizes the initial small fluctuation in spatial pattern [115]. On the other hand, the physical mechanism of the symmetry breaking induced by the active force generation of the actin cytoskeleton is still poorly understood. Such contractile force-driven symmetry breaking is underlying various biological phenomena, ranging from the revolving wave in epithelial cells [116] (Fig. 4.1a), chiral symmetry breaking of radial actin flow in fibroblasts [8] (Fig. 1.1c), rotational surface wave in dividing cells [117] (Fig. 4.1c), to circus movement of bleb in *Xenopus* blastomere [118] (Fig. 4.1b). Although recent theoretical studies proposed that translational symmetry breaking could be achieved by the competition between active stress and diffusive relaxation [40, 41, 42], the biological relevance of such mechanism is still unclear. This is because it is difficult to control the physical parameters in living cells, such as polymerization rate and
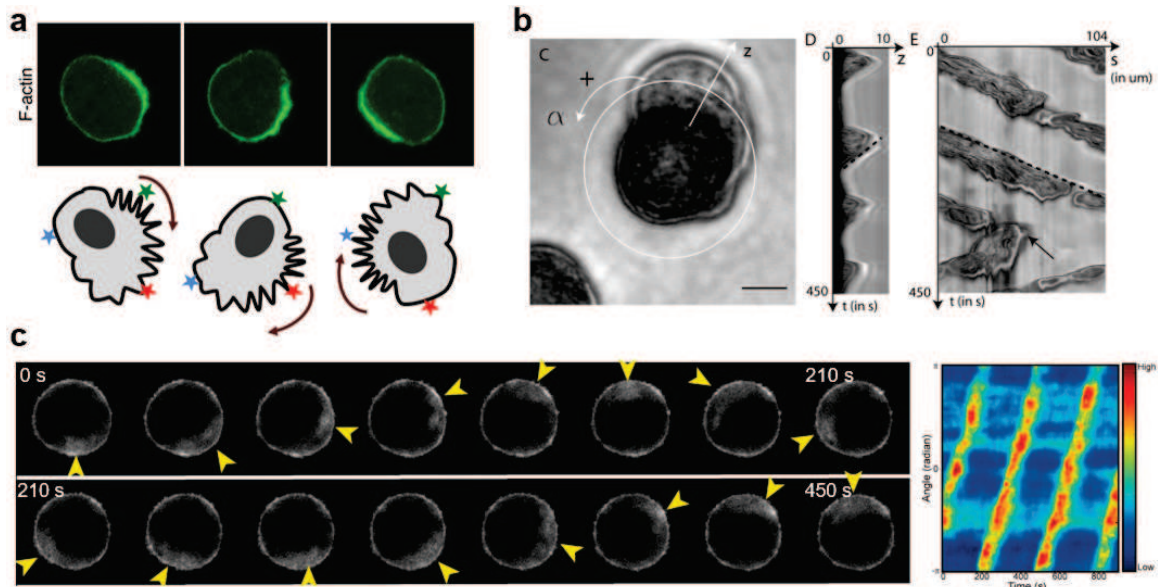
Figure 4.1: (**a**) Time-lapse image of the rovolving wave of epithelial CHO cells. (**b**) The snapshot and the kymograph of the traveling bleb known as 'circus movement' in *Xenopus* blastomere. (**c**) Time-lapse image of the revolving actin wave at the surface of the metaphase rounded HeLa cell. The right kymograph is taken along the periphery of the cell. Images were adopted from [116, 117, 118].

contractility, thus it is challenging to compare the simple theoretical prediction to the experimental results in living cells.

To overcome such limation, here we use our artificial cell system to flexibly control the biophysical parameters and to compare the experiment with theoretical models. By exploring the various physical parameter space, we found that the transition of stationary actin flow to periodic waves. Moreover, by increasing the F-actin polymerization rate at the droplet surface, we found the rotational symmetry breaking of the actin wave. Together, this is the first experimental demonstration of symmetry breaking induced pattern formation in actomyosin networks confined in cell-sized spaces, which will provide the physical understanding of the biological pattern formation driven by active cytoskeletal systems.

4.2 Materials & Methods

4.2.1 Experimental setup

Regents and Recombinant proteins. We use the same reagents and recombinant proteins that are already explained in Chapter 2 and Chapter 3. Namely, phosphatase inhibitor calyculin A which increases the net contractility of the actomyosin network, Arp2/3 activating domain VCA which enhances the actin polymerization, actin polymerization inhibitor of cytochalasin D that binds actin filaments, and myosin contractility inhibitor Y27632 that inhibits ROCK (Rho-associated coiled-coil forming kinase).

4.2.2 Image analysis

Fourier analysis. To quantitatively analyze the period of the contractile wave, we used the fourier analysis of the total intensity within the region of interest. Given that the center of the droplet is the origin $r = 0$ in the polar coordinate, the local density of the actin filaments were measured through the local fluorescent intensity $I(r, \theta, t)$. The intensity was then averaged over the region of interest $0.45R < r < 0.55R$, $0 < \theta < 2\pi$, thus $I(t) \equiv \int_{0.45R}^{0.55R} \int_0^{2\pi} I(r, \theta, t) \mathrm{d}r \mathrm{d}\theta$. We then performed the Fourier transform $\bar{I}(\omega) = (1/2\pi) \int_0^{10\mathrm{min}} I(t) e^{-i\omega t} \mathrm{d}t$. Then, the period of the actin wave was calculated from the peak of $\bar{I}(\omega_{\mathrm{peak}})$, from the relation $T_{\mathrm{peak}} = 2\pi/\omega_{\mathrm{peak}}$. Note that $T_{\mathrm{peak}} \to \infty$ (i.e., $\omega_{\mathrm{peak}} \to 0$) corresponds to the stationary flow, in which there is no oscillatory structure in the intensity time course.

Confocal microscopy To visualize the F-actin network in detail, we used confocal microscopy and focused on the mid-plane of the confined droplet (Fig. 4.2). Time-lapse images were acquired every 6 s using an epifluorescence microscope (IX73; Olympus) equipped with ×10 objective lens (U Plan WD 10×/0.25; Meiji Techno Japan)
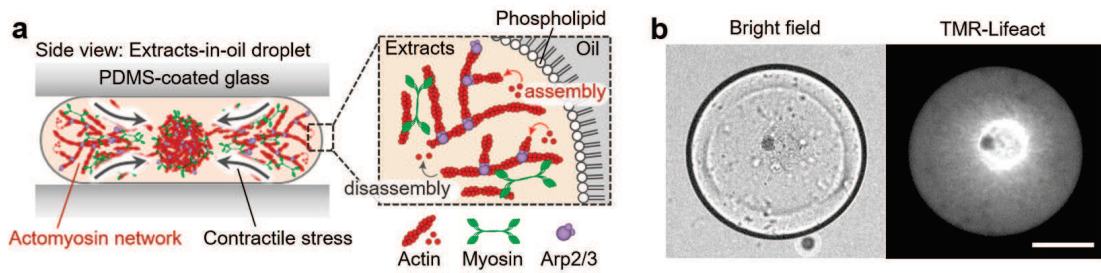
Figure 4.2: (**a**) Schematic showing the experimental setup. The droplets were confined between the PDMS-coated glass slides and the dynamics of the actomyosin contraction is observed by confocal microscopy. (**b**) A representative image taken at the middle plane of the droplet. Scale bars, 100 μm.

or $\times$20 objective lens (TU Plan ELWD 20$\times$/0.40; Nikon), a cooled CMOS camera (Neo5.5; Andor Technology), and a stable excitation light source (XLED1; Lumen Dynamics). The contact area between the droplet and substrate was recorded using a confocal microscope (IX73; Olympus) and a confocal scanning unit (CSU-X1; Yokogawa Electric Cor. Ltd.) equipped with iXon-Ultra EM-CCD camera (Andor Technologies) and $\times$20 objective lens (UPlanSApo 20$\times$/0.75; OLYMPUS) under a 488 nm fluorescence channel. For all microscopic examinations, the room temperature was maintained at 20 ± 1°C. All images were taken by confocal microscopy.

4.3 Results

4.3.1 Experiment I: Transition from steady-flow to periodic wave

In active systems, contractile stress is often a primal factor to break the symmetry [40, 41, 42]. To see the effect of contractile stress on pattern formation of the actomyosin network, we first added calyculin-A, which is a myosin II phosphatase inhibitor thus the number of active myosin motor is increased, leading to the larger contractile stress. Interestingly, we found the state transition from the stationary actin flow (Fig. 4.3a) to the periodic actin wave by increasing the concentration of calyculin-A (Fig. 4.3b). Such periodic pattern can be seen in the angular kymograph extracted from the time-course (Fig. 4.3c-e).

To quantitatively analyze the periodic wave behavior, the fluorescence intensity was averaged over the angle $0 < \theta < 2\pi$, and then Fourier transform was performed to see the periodic structures (Fig. 4.4a,b). The power spectrum of the actin intensity shows that the peak was emerged for the calyculin A concentration larger than 30 uM, indicating that the emergence of periodic wave (Fig. 4.4c). Here, the peak frequency $1/T \to 0$ indicates the wave period of $T \to \infty$, corresponding to the stationary actin flow, while the finite peak frequency $1/T$ corresponds to the periodic actin wave with a finite wave period T. The peak frequency was plotted along with the calyculin concentration, where periodic actin wave emerged around the concentration of calyculin-A 30 pM (Fig. 4.4d). Notably, the wave period was mostly remained the same value around $T \simeq 1.5$ min even for the larger calyculin concentration, indicating that the period is not determined by the myosin contractility but rather determined by the other factor such as the polymerization rate of the F-actin.
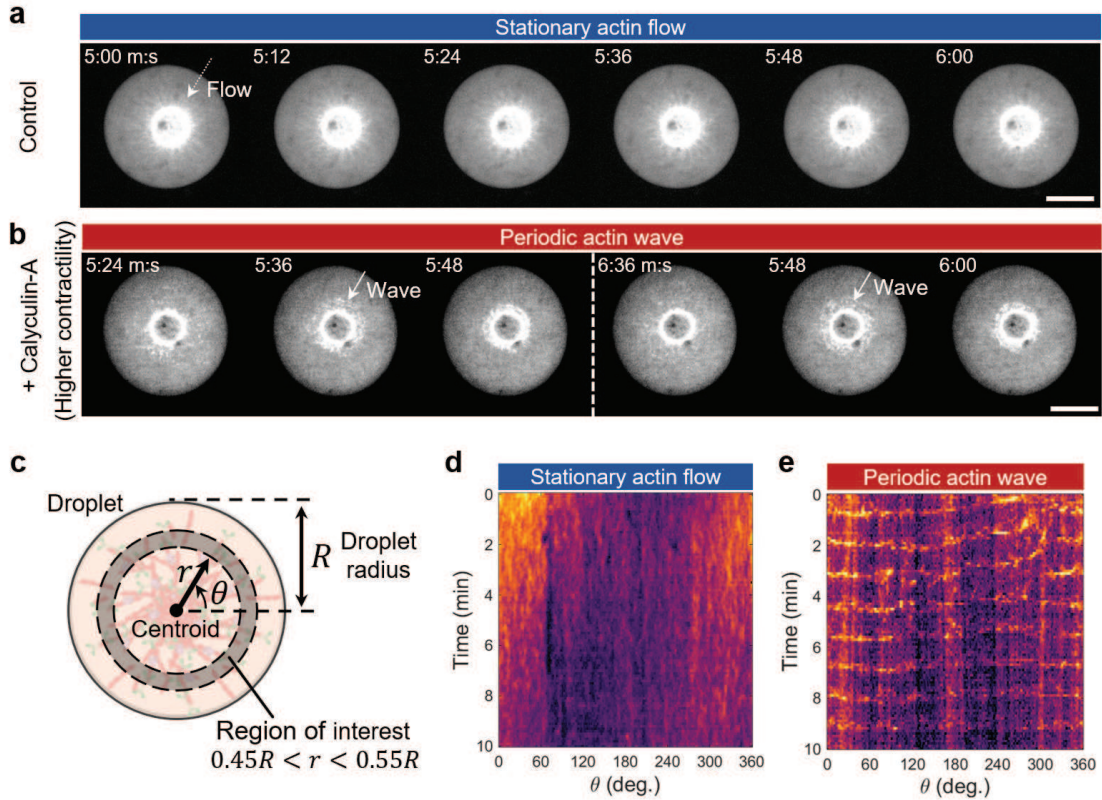
Figure 4.3: (**a**) Time-lapse images showing the stationary actin flow under control condition. (**b**) Time-lapse images showing the periodic actin wave contraction after adding 30 nM calyculin A. (**c**) Schematic showing the definition of the region of interest where kymograph was extracted for (d) and (e). (**d**) Angular kymograph extracted from (a). (**e**) Angular kymograph extracted from (b). Horizontal stripes represent the ring-shaped actin wave. All images were taken by confocal microscopy. Scale bars, 100 μm.
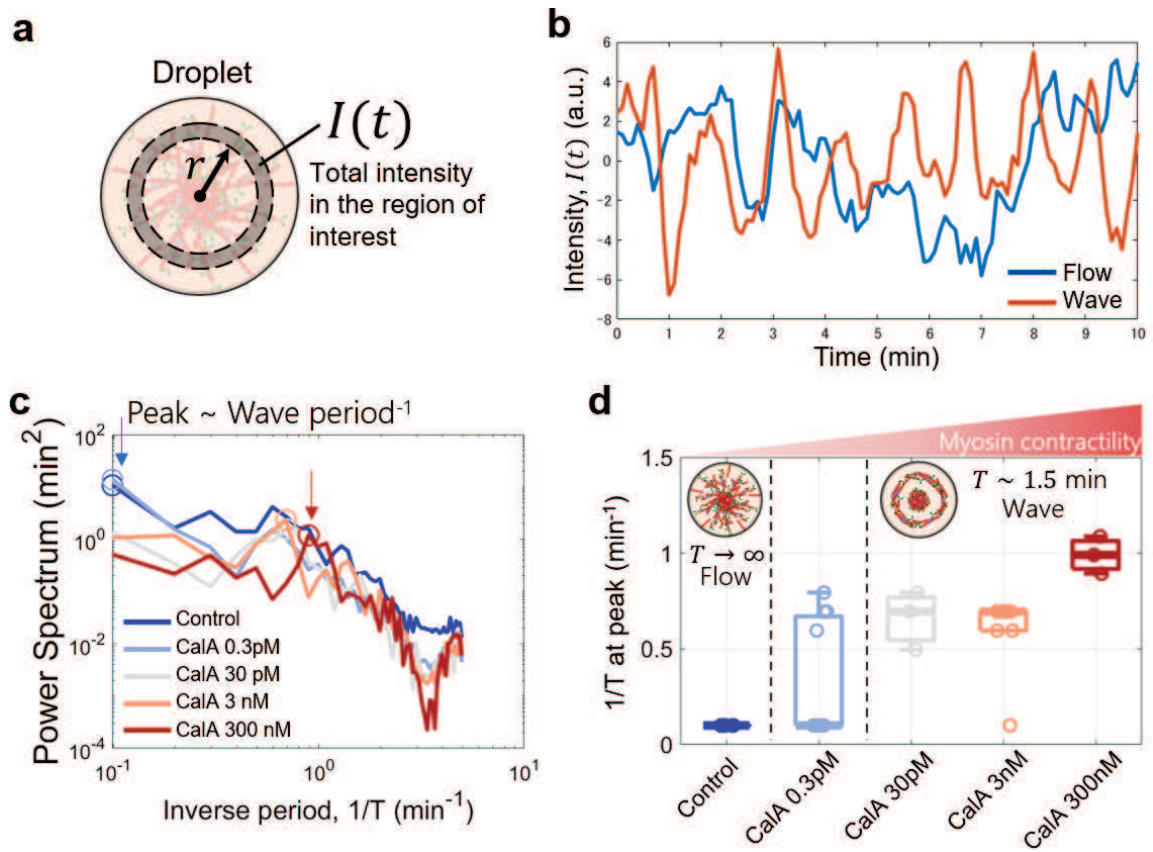
Figure 4.4: (**a**) Schematic showing the definition of the total intensity $I(t)$, which is an angular average within the region of interest. (**b**) Total intensity time course. The curve was random noise in the case of control (blue), while the periodic oscillation can be seen in the case of calyculin A (orange). (**c**) Power spectrum was calculated from (b). Note that the peak indicates the presence of periodic structure within the time course. (**d**) Peak frequency was extracted from (c). Wave-like structure is emerged at the calyculin concentration larger than 0.3 pM.

4.3.2   Theory I: Active fluid model

To understand the physical mechanism of the transition from actin flow to periodic wave, here we developed a theoretical model of actomyosin network confined in a circular confinement (Fig. 4.5a). We describe the actomyosin network as an active fluid producing active stress σ_{act}, which experiences the internal viscous stress σ_{vis} and the external friction from the cytoplasm and the membrane $-\gamma\mathbf{v}$, where γ is the effective friction coefficient. Thus, the momentum balance for the active fluid is given by

$$\nabla \cdot (\sigma_{\text{vis}} + \sigma_{\text{act}}) = \gamma\mathbf{v}. \tag{4.1}$$

The viscous stress is given by the dissipative part of the viscous fluid,

$$\sigma_{\text{vis},ij} = \eta_b \delta_{ij} \nabla \cdot \mathbf{v} + 2\eta_s \left(v_{ij} - \frac{1}{3}\delta_{ij} \nabla \cdot \mathbf{v} \right) \tag{4.2}$$

where η_b and η_s are the bulk and shear viscosities, respectively, and $v_{ij} = (1/2)(\partial_j v_i + \partial_i v_j)$. In addition, active stress is assumed to be proportional to the density of the actomyosin gel,

$$\sigma_{\text{act}} = (\zeta\Delta\mu)_0 f(\rho)\mathbf{I}, \tag{4.3}$$

where $(\zeta\Delta\mu)_0$ is the effective myosin contractility per actin filament, ρ is the local density of the actomyosin gel, and $f(\rho) = \rho/(\rho_0 + \rho)$, where ρ_0 is a constant. The actomyosin density dependence of the active stress was chosen to avoid overshoot. For simplicity, we assumed that the local myosin density is proportional to the F-actin density ρ, thus we only consider the mass conservation equation of the F-actin:

$$\frac{\partial\rho}{\partial t} + \nabla \cdot (\rho\mathbf{v}) = D\nabla^2\rho + k_p - k_d\rho, \tag{4.4}$$

where D is the effective diffusion coefficient of F-actin, k_p and k_d is the polymerization and depolymerization rate of F-actin, respectively.

4.3.3 Theory II: Phase-field model: Numerical simulation in 2D space with circular boundary

To implement circular boundary condition, we used phase-field model [119, 120]. The phase-field dynamics were developed in [121], which is written as

$$\frac{\partial \phi}{\partial t} = D_\phi \nabla^2 \phi + \Gamma_\phi U'(\phi). \tag{4.5}$$

The term on the right hand side is derived from the Helfrich free energy. The diffusion term represents the surface tension of the membrane, and the second term is the derivative of the double-well potential U, $U'(\phi) = \phi(\phi - 1)[\phi - 1/2 - \alpha_0(V/V_{\text{tar}} - 1)]$, its fixed points $\phi = 0$ and $\phi = 1$ describes the outside and the inside of the cell. The term $\alpha_0(V/V_{\text{tar}} - 1)$ describes the conservation of the cell volume $V = \iint d\mathbf{r}\phi$ toward a target volume V_{tar}.

In the phase-field model, no-flux boundary condition to constrain actomyosin within the cell boundary can be imposed by an effective energy $E(\rho, \phi) = \iint d\mathbf{r}\{(\rho^2 + \beta[(1 - \phi)^2 + \beta])\}^{1/2}$, where β is introduced to avoid singularities [121]. This led to the final, full set of non-dimensionalized equations,

$$\nabla^2 \mathbf{v} + \lambda \nabla(\nabla \cdot \mathbf{v}) + \nabla f = \mathbf{v} \tag{4.6}$$

$$\frac{\partial \rho}{\partial t} + \text{Pe}\nabla \cdot (\rho \mathbf{v}) = \nabla^2 \rho + k_p - k_d\rho + \epsilon_\rho \nabla^2 \frac{\delta E}{\delta \rho} \tag{4.7}$$

$$\frac{\partial \phi}{\partial t} = D_\phi \nabla^2 \phi + \Gamma_\phi U'(\phi) \tag{4.8}$$

where the length and time scales were non-dimensionalized by the length-scale unit $l = (\eta/\gamma)^{1/2}$ and the time-scale unit $\tau = \eta D/\gamma$. In addition, $\text{Pe} = Ul/D = \zeta/D\gamma$ is the Peclet number (i.e., the ratio between the time scale of active transport and diffusive transport), where characteristic velocity $U = \zeta/(\eta\gamma)^{1/2}$ was introduced. Also, rescaled parameters were redefined as $\rho/\rho_0 \to \rho$, $k_p/\rho_0\tau \to k_p$, $k_d/\tau \to k_d$, and $\lambda = \eta_v/\eta_s =$

4/3 is the constant. Importantly, here we imposed the local actin assembly near the inner surface of the droplet to mimic the experimental observation (Fig. 2.11b), where we introduced the bulk polymerization speed k_p^{bulk} at $0 < r < 0.9R$ and the surface polymerization speed k_p^{surface} at $0.9R < r < R$ (Fig. 4.5b). Here, we define the polymerization ratio as $\alpha_{\text{p}} \equiv k_{\text{p}}^{\text{bulk}}/k_{\text{p}}^{\text{surface}} = 0.1$.

To solve our equations, we discritise them by finite difference method and performed numerical simulation. In each time step, we first determined the density field and the phase-field through the diffusion equations Eq. (4.7) and Eq. (4.8). We then updatde the velocity field through the force balance equation Eq. (4.6), where we used Fourier transformation. In all simulations, we use $\Delta x = 10^{-1}, \Delta y = 10^{-1}$ and $\Delta t = 10^{-5}$. We checked that our results do not change for smaller values. As the initial condition, we took $\rho(x,y) = 1, v(x,y) = 0$.

We first present the solution for Pe $= 30, k_{\text{p}}^{\text{surf}} = 1.5, k_{\text{d}} = 1, \beta = 0.0001, D_{\phi} = 1, \Gamma_{\phi} = 160D_{\phi}, \epsilon_{\rho} = 20, \alpha_0 = 50$. At the boundary of the droplet, the gel contracts inwardly (Fig. 4.5c). As can been seen in the kymograph, the system relaxes into a stationary flow state of actomyosin, while the system reaches a periodic state of the contractile actomyosin ring at a larger contractility (Fig. 4.5d,e). Fourier analysis of the intensity shows that the periodic oscillation with a finite period emerges as the Pe increases (Fig. 4.5f).

To further investigate the flow to wave transition, we numerically solved the equations with different Pe and $k_{\text{p}}^{\text{surf}}$, and then obtained the phase diagram (Fig. 4.6a). At the small polymerization speed $k_{\text{p}}^{\text{surf}} \sim 0$, flow state is stable, while the larger polymerization speed $k_{\text{p}}^{\text{surf}} > 1$, the periodic wave state emerges with the large Pe. Notably, the flow state again becomes stable at a larger polymerization speed. This could be because the contrast of the actomyosin density between the bulk and the surface becomes small at a large polymerization speed.
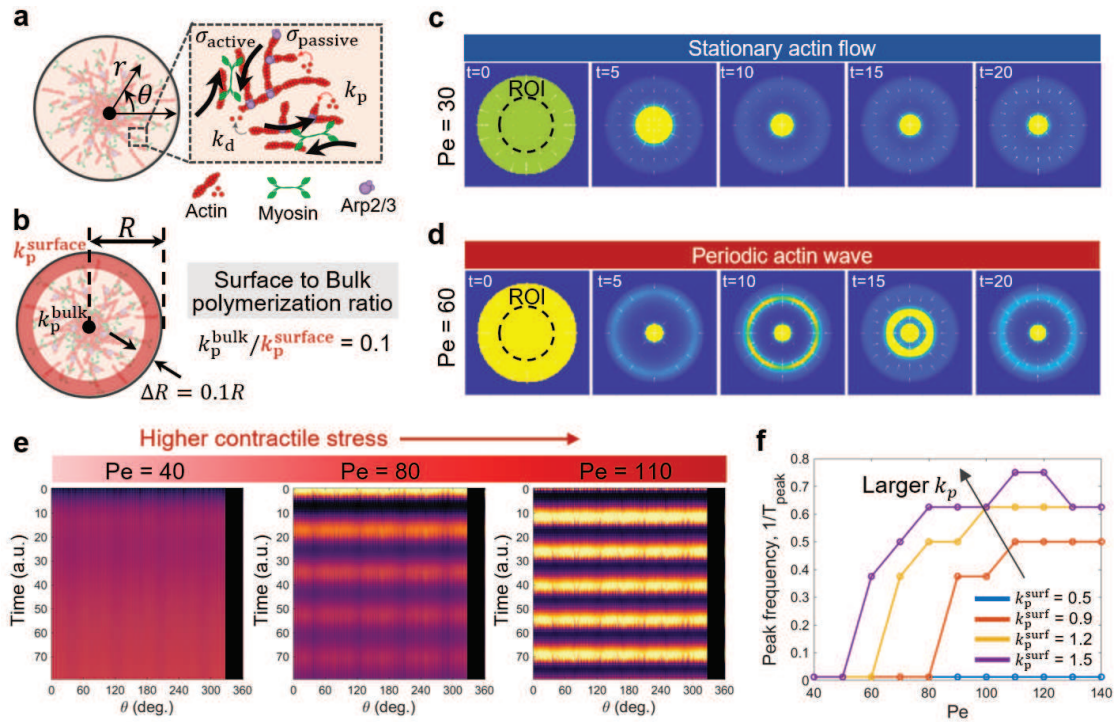
Figure 4.5: (**a**) Schematic showing the internally generated active stress σ_{act}, passive stress σ_{passive}, and the polymerization and depolymerization of F-actin k_{p} and k_{d}, respectively. (**b**) Schematic showing the definition of bulk and surface polymerization rate $k_{\text{p}}^{\text{bulk}}$ and $k_{\text{p}}^{\text{surface}}$, respectively. Here, we assume that the surface polymerization rate is 10 times faster than the bulk polymerization rate to mimic the experimentally observed local F-actin polymerization at the inner droplet surface. (**c**) At the active Peclet number Pe = 30, stationary actin flow emerged. (**d**) At Pe = 60, Periodic actin wave emerged. (**e**) Angular kymographs were extracted from the ROI in the time-sequence (c) and (d). The larger the active Peclet number (i.e., effective contractility), the periodic actin wave was stably emerged. (**f**) Active Peclet number dependence of the peak frequency is shown. The graph shows that the periodic wave emerged at a cirtain Pe as the Pe incrased. Note that the wave period is mostly same for the larger Pe, whereas the larger k_{p} changes the wave period, indicating that the wave period is determined by the polymerization speed.

4.3.4   Experiment II: Experimental verification of flow to wave transition

To substantiate the mechanism of the transition between the flow and the wave state, we performed the molecular perturbation. In the control condition, the flow state was stable (Fig. 4.6(i)). On the one hand, by adding the calyculin A, a phosphatase inhibitor that increases the net contractility, the wave state emerges (Fig. 4.6(ii)), while the flow state becomes stable by increasing the polymerization speed of F-actin with the addition of Arp2/3 activating VCA domain (Fig. 4.6(iii)). On the other hand, by adding the Cytochalasin D, an inhibitor of F-actin polymerization, the stable state was changed from the flow to the wave state (Fig. 4.6(iv)), while the flow state become stable by adding the myosin phosphorylation inhibitor Y27632 that decreases the contractility (Fig. 4.6(iv)). Together, the theoretical phase diagram was qualitatively reproduced by the experiments, which further substantiates the validity of the proposed active fluid model.
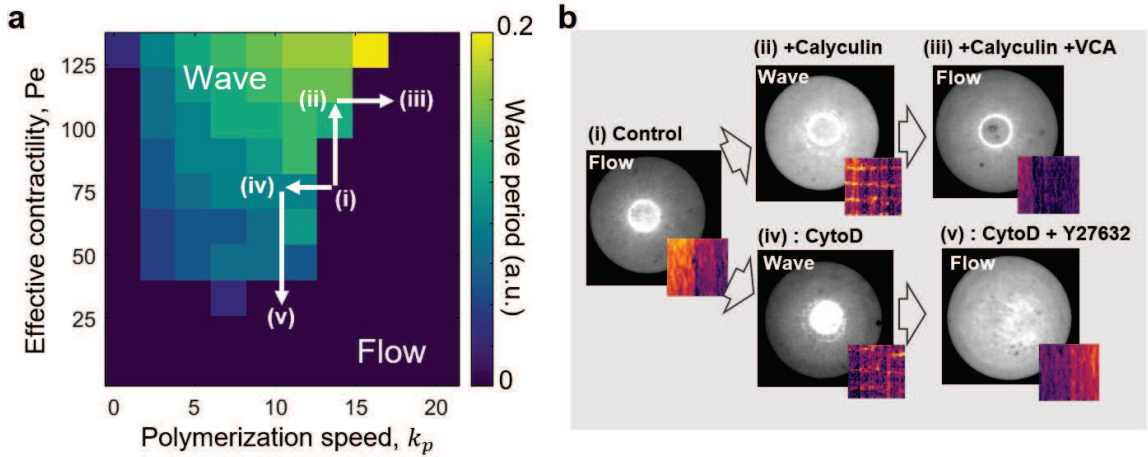
Figure 4.6: (**a**) Phase diagram of the active fluid model. (**b**) Transition between flow and wave was experimentally confirmed by the molecular perturbations. (i) Control condition. (ii) By adding the calyculin A, a myosin phosphatase inhibitor, increasing the effective contractility Pe and the wave state is stabilized. (iii) By adding the VCA, an activator of actin polymerizing protein Arp2/3, increasing the polymerization rate k_p and the flow state is stabilized. (iv) By adding cytocharasin D, a F-actin polymerization inhibitor, decreasing the polymerization rate k_p and the wave state is stabilized. (v) By adding the Y27632, an inhibitor of myosin phosphorylation, decereasing the effective contractility Pe and the flow state is stabilized.

4.3.5 Theory III: The influence of bulk/surface polymerization ratio α_p

We have so far fixed the bulk to surface polymerization ratio $\alpha_p = k_p^{\text{bulk}}/k_p^{\text{surface}} = 0.1$ to mimic the experimentally observed local F-actin assembly at the droplet surface. However, it is unclear how the value of the polymerization ratio α_p affects the phase behavior of the contractile actomyosin gel. To answer this question, we altered the bulk/surface polymerization ratio between $0.1 < \alpha_p < 1$ (Fig. 4.7a). Notably, at a fixed Pe, the wave state emerges at the smaller bulk/surface polymerization ratio (i.e., the larger bulk to surface contrast), suggesting that the ratio of bulk to surface polymerization speed is crucial to determine the contractile behavior of the confined active gels (Fig. 4.7b). Therefore, this model predicts that the phase transition of the contractile behavior of active gels in terms of the ratio of the surface to bulk
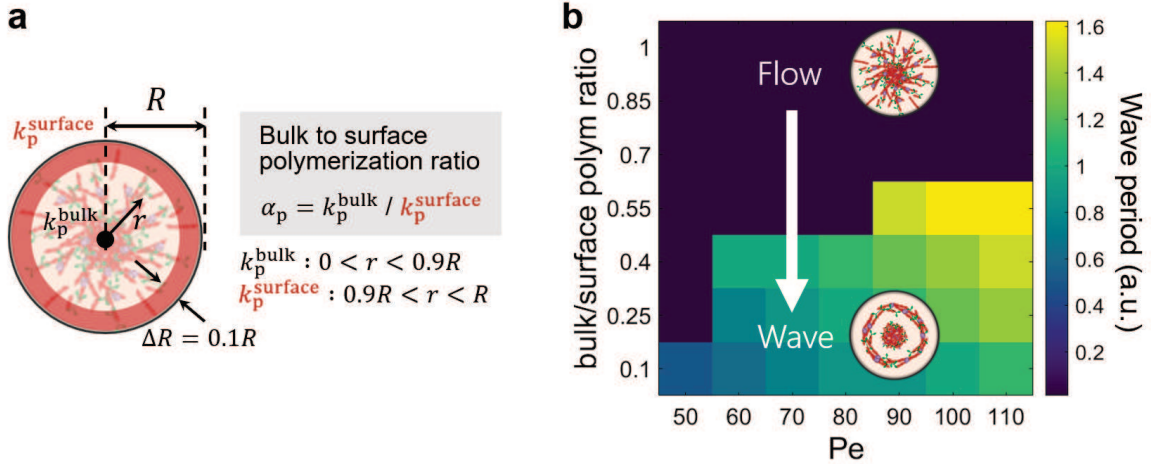
Figure 4.7: (**a**) Schematic showing the definition of the bulk and the surface polymerization speed k_p^{bulk} and $k_p^{surface}$, respectively. (**b**) Phase diagram showing the transition from stationary flow to periodic wave induced by the high contrast between the bulk and the surface polymerization speed.

polymerization speed.

4.3.6 Experiment III: Rotational symmetry breaking of active gels

To experimentally test the theoretical prediction, we then increased the polymerization at the droplet surface by using the PIP$_2$ lipid, which is locally recruited at the droplet surface and activates the F-actin nucleation via Arp2/3 as shown in Chapter 3 (Fig. 4.8a). Surprisingly, the enhanced surface F-actin assembly induced the rotational symmetry breaking of the wave, and subsequently the revolving wave emerged (Fig. 4.8b,c). We found that $\sim 15\%$ (n=34) of droplets showed the stable rotational wave, while the other droplets broke the symmetry of the cluster positioning and the rotational wave turned into the asymmetric flow. On the other hand, such rotational symmetry breaking was not observed in the numerical simulation only by increasing the contrast between the bulk and surface polymerization speed, contradicting the experimental result. Thus, we then explored the mechanism of the rotational symmetry breaking in the numerical simulation.
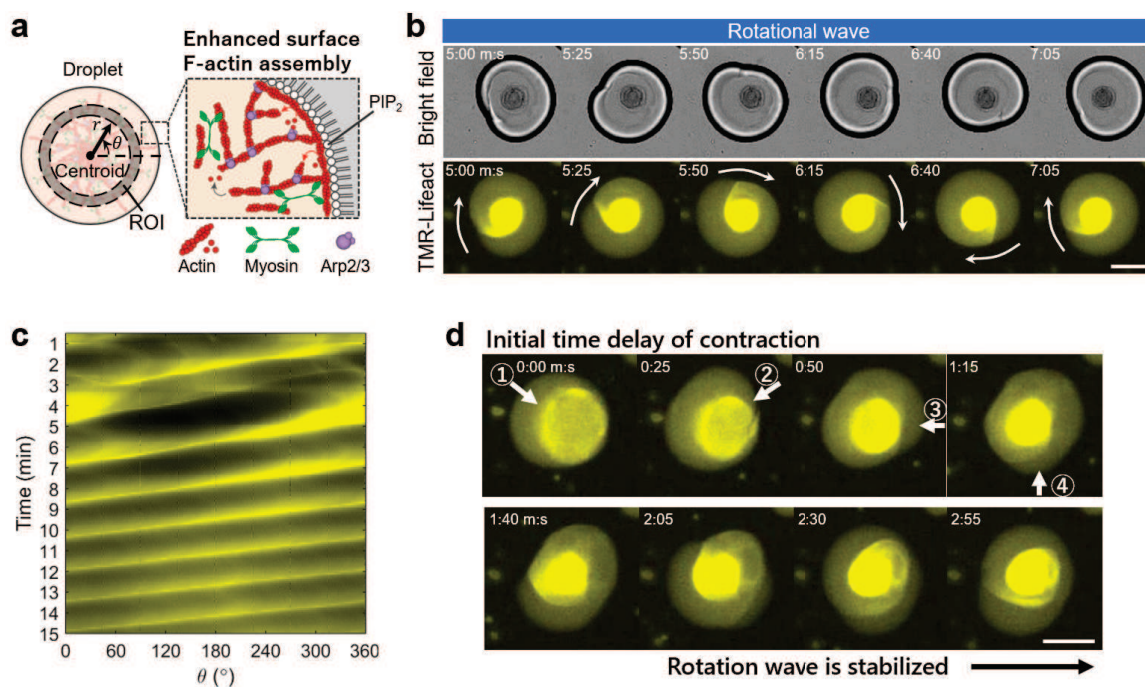
Figure 4.8: (**a**) Schematic showing the locally enhanced F-actin polymerization at the droplet surface induced by the Arp2/3 activating lipid PIP$_2$. (**b**) Time-lapse images showing the rotational wave. (**c**) The angular kymograph extracted from (b). (**d**) Initial time delay of contraction and the subsequently stabilized rotational wave. All images were taken by epi-fluorescence microscopy. Scale bars, 100 μm.

4.3.7 Theory IV: Initial time delay of contraction-induced rotational symmetry breaking

To understand the mechanism of the rotational symmetry breaking, we first focused on the onset of the rotational symmetry breaking events observed in the experiment. Notably, because of the strong actin-membrane binding induced by the F-actin assembly activating lipid PIP$_2$, the initial contraction had a time delay to detach from the droplet surface, and the rotational wave gradually became stable (Fig. 4.8d). To test the influence of such time delay of contraction in numerical simulation, we implemented the time delay of contraction as the initial condition. For simplicity, we used the non-deformable circular boundary and the circular droplet was divided into four regions and each region initially started to contract with the time delay τ_d (Fig. 4.9a,b), by which we can mimic the initial time delay events observed in the

experiments.
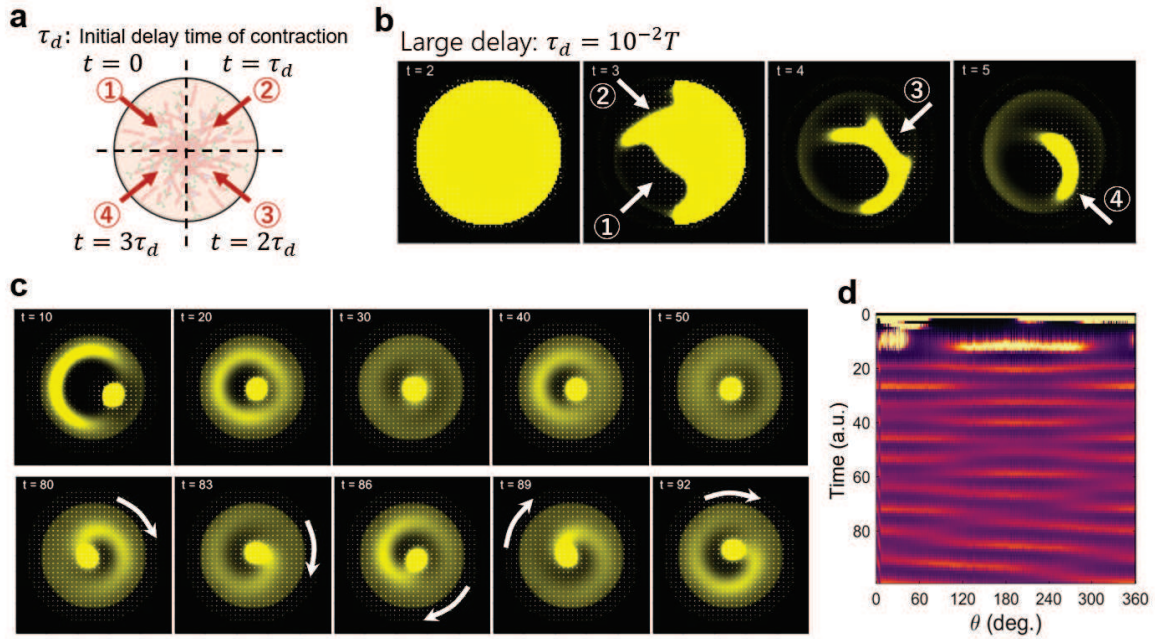
Figure 4.9: (**a**) Schematic showing the definition of the time delay in contraction. The circular domain was devided into 4 regions, in which each region successively starts to contract with time delay τ_d. (**b**) Time-lapse images of the initial time delay in contraction. Parameters were Pe = 90, k_p^{surface} = 1.75, and α_p = 0.01. (**c**) Time-lapse images showing the initial flucuation and the subsequently stabilized rotational wave. (**d**) Angular kymograph extracted from (c).

As can be seen in the kymograph, with the time delay $\tau_d = 10^{-2}T$ (T is the total simulation duration), we found that the rotational wave becomes stable after several time steps (Fig. 4.9c,d). This suggests that the rotational symmetry breaking requires an initial time delay of contraction. To see the influence of the time delay, we then changed the time delay from $\tau_d = 10^{-2}T$ to $\tau_d = 10^{-4}T$. Interestingly, the rotational wave was emerged even in the small time delay, in which we could not visually observe the time delay of the contraction (Fig. 4.10a). In this case, the ring-like wave was initially stable, while the distribution of the actomyosin gradually fluctuated, and finally, the rotation wave was stabilized (Fig. 4.10b). Importantly, we confirmed that the magnitude of τ_d did not affect the final stable rotation period, indicating that the rotation wave is not directly determined by the initial condition, but it is

rather a self-organized stable fixed point determined by the physical parameter of the system (Fig. 4.10c). Together, the active gel theory explains the mechanism of the rotational wave, that is, the rotational wave emerges as a result of an initial time delay of contraction.
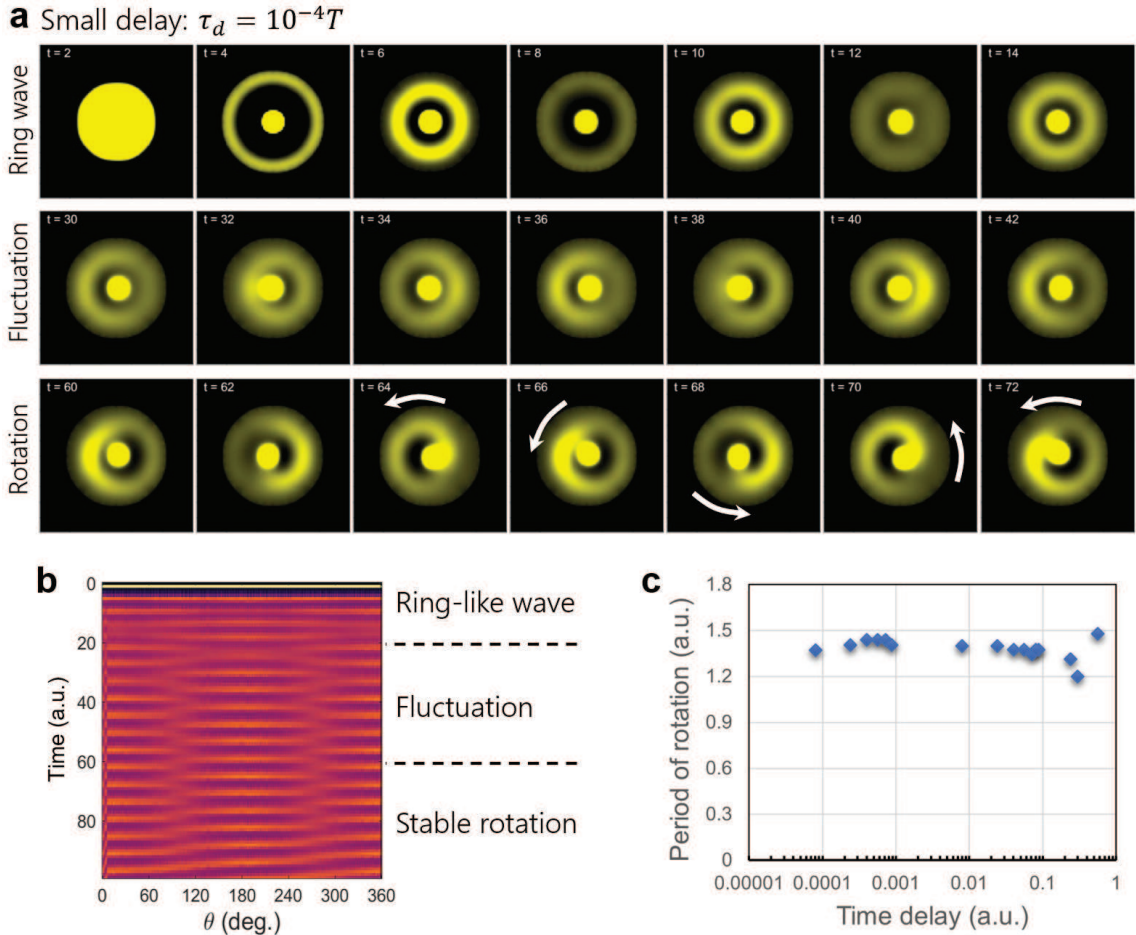
Figure 4.10: (**a**) Time lapse images showing the dynamics of the emergence of the rotational wave with visually negligibly small time delay $\tau_d = 10^{-4}T$. At the beginning, ring-like wave was stable, while the position of the highly accumulated actomyosin cluster started to fluctuate, and eventually the rotation wave was stabilized. (**b**) Angular kymograph extracted from (a). (**c**) The initial time delay dependence of the rotation period.

4.3.8 Theory V: Phase-diagram of the rotational wave

Finally, we explored the influence of the Peclet number Pe and the polymerization speed k_p^{surf} in the emergence of the rotational wave. The phase diagram shows that with a fixed k_p^{surf}, the stationary flow was stable at a small Pe, while the ring-like wave was stable at a large Pe, consistent with the previous section. Notably, however, in the presence of the initial time delay of contraction, the rotational wave emerged at the phase boundary between the flow and the ring-like wave (Fig. 4.11a, red squares). This result can be interpreted as follows. In our simulation, the contractile behavior of the actomyosin network is determined by an effective tug-of-war between the bulk actomyosin network and the actomyosin network close to the droplet periphery. The bulk actomyosin network is responsible for the stationary flow, while the surface actomyosin network is responsible for the ring-like wave. Indeed, by increasing the bulk polymerization speed, the stationary flow state was observed in the larger phase-space (Fig. 4.11b). Thus, the rotational wave would emerge at the phase boundary between the flow and the ring-like wave, at which the competing forces between the bulk and the surface actomyosin network may balance. However, the more quantitative mechanism is still unclear due to the difficulty to obtain the analytical expression from the complex equations. More detailed analysis such as non-linear perturbative analysis remains as future work.
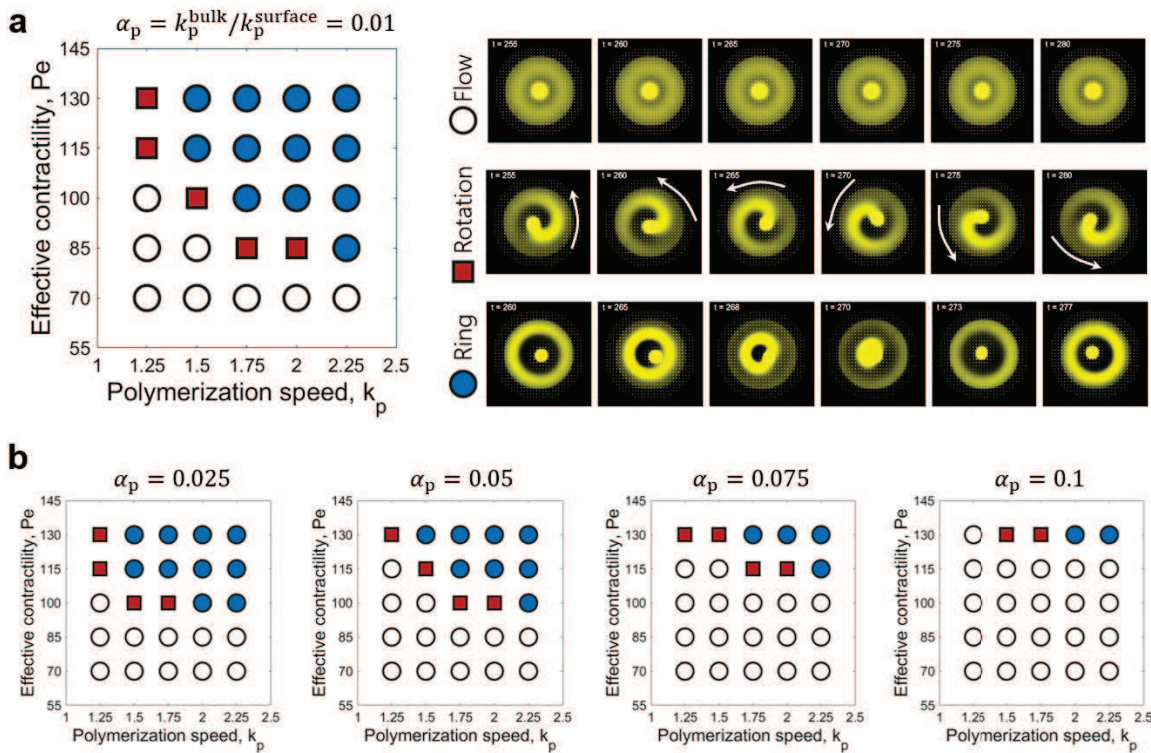
Figure 4.11: (**a**) Phase-diagram with the initial time delay in the contaction. Each symbol corresponds to the flow (empty circle), the wave (filled blue circle), and the rotation wave (filled red square). The simulation was performed with the bulk to surface polymerization ratio $\alpha_p = 0.01$. (**b**) The bulk to surface polymerization ratio $\alpha_p = 0.01$ dependence of the phase-diagram.

4.4 Discussion

Previous studies using cytoplasmic actomyosin networks found various contractile behavior of the actomyosin networks such as stationary flow [23, 24] and periodic ring-like wave [16, 28], whereas how such distinct waves emerge in the same system was elusive. In this study, combining the various molecular perturbation and theoretical modeling, we showed that such distinct contractile behavior can be realized in the same cytoplasmic actomyosin network, and we constructed the simple theoretical model explaining the mechanism of the various contractile behavior from the stationary flow, ring-like wave, to the rotational wave.

Recent studies showed that the contractile actomyosin network can be used to move the nucleus-like large structures at the center of the extracts-in-oil droplet [28, 29]. In these studies, however, different actomyosin structures, either the stationary flow or the periodic ring-like wave, were proposed as a driving force of the centering of the nucleus-like large structures. Based on the present study, we can understand that such distinct self-organized actomyosin structures were not mutually exclusive but can be realized in the same system depending on the contractility and the polymerization speed of F-actin. Therefore, our study provides an integrative understanding of the self-organization of the actomyosin networks confined in cell-sized spaces.

Importantly, our study showed that contractile stress is the key to realizing various self-organized states, in which the pattern formation is stabilized when the active stress outweighs the diffusive relaxation. This is the key difference from the pattern formation of the reaction-diffusion systems, in which the symmetry breaking emerges as a result of the different diffusion time scales between the activator and the inhibitor. Notably, the periodic actin wave can be observed in various morphological events from cell division [117] to the cell migration [11], thus the simple theoretical model developed in this study would give a mechanical understanding of such contractile behavior in living systems.
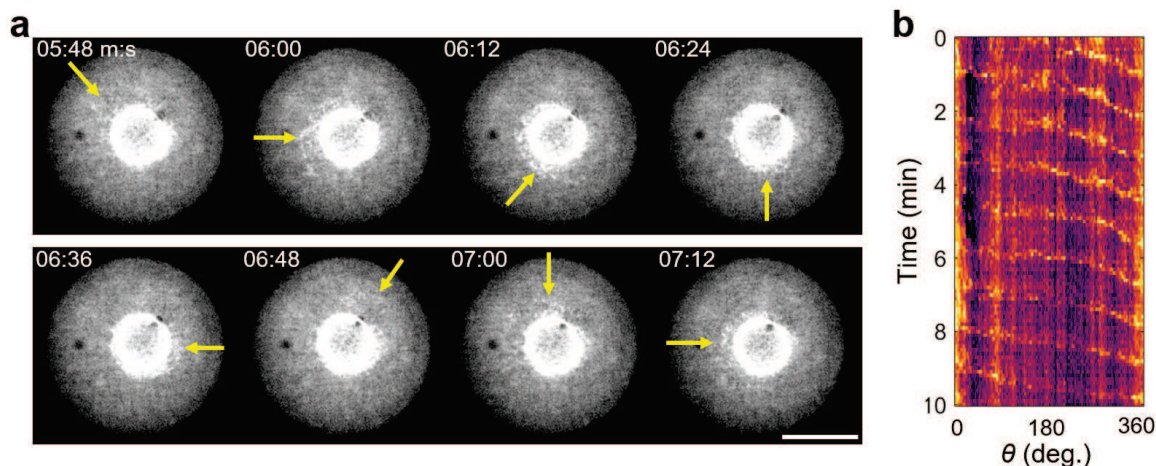
Figure 4.12: (**a**) Time-lapse images showing the rotational wave under the condition of 0.3 pM Calyculin A in the absence of the actin-membrane binding induced by PIP_2. (**b**) The angular kymograph extracted from (b). Images were taken by confocal microscopy. Scale bars, 100 μm.

Finally, we found that the rotation wave emerged in the confined cytoplasmic actomyosin networks by increasing the polymerization of F-actin at the droplet surface. Interestingly, several studies have reported such rotational wave driven by contractile actomyosin networks in various cell types, from fibroblasts [116], HeLa cell [117], CHO cell [8], fish parasite [122], *Xenopus* blastomere [118]. This suggests that the rotational wave is a universal biological phenomenon, which is not significantly affected by the detail of the system. In the present study, we provided a simple mechanism of the rotational symmetry breaking of the actomyosin network under non-deformable circular confinement, that is, the initial time delay of contraction. Such time delay could usually occur in the living system because the actomyosin network is tightly bound to the surface of the cells. Yet, in our simulation model, we have not included the effect of the membrane deformation induced by the contractilie force applied to the cell membrane. Thus, it remains open how the membrane deformation contributes to the likelifood of the rotational symmetry breaking. We expect that such deformation could change the center-of-mass of the actomyosin system, which might add initial fluctuation or asymmetry into the spatial distrubution of the contractile stress. In

fact, we rarely observed the rotational wave in the absence of actin-membrane binding (less than 3%, 1 in more than 30 droplets) (Fig. 4.12), whereas ∼15% of droplets showed stable rotaional wave with actin-membrane binding. Therefore, theoretical modeling of the influence of the membrane deformation on the rotational symmetry breaking will be a significant future challenge. Also, it would be interesting to test the influence of the time delay of actomyosin contraction in living cells using laser ablation or optogenetics to control the emergence of the rotational waves, which would further validate our theoretical model.

4.5   Conclusion

To conclude, we explored how the pattern formation driven by the contractile force is emerged in a confined space using cytoplasmic actomyosin networks encapsulated in water-in-oil droplets. The numerical simulation based on active gel theory showed that the flow to wave transition emerges as a result of the contrast between the bulk and the surface polymerization speed, in which the effective active stress Pe plays a significant role. Moreover, by imposing the initial time delay in contraction, we found that the rotational wave is finally stabilized in the system, which can only be observed at the phase boundary between the stationary flow and the rind-like wave. Together, this study provides an integrative understanding of the self-organization and pattern formation of active gels confined in cell-sized closed spaces.

Chapter 5

Summary and Conclusions

In this thesis, I have studied the mechanism of the (I) intracellular positioning symmetry breaking (Chapter 2), (II) Droplet migration induced by the shape symmetry breaking (Chapter 3), and (III) Rotational symmetry breaking induced actomyosin wave dynamics (Chapter 4), by harnessing the simplified nature of the artificial cell models and theoretical modeling based on active gel theory.

(I) Intracellular positioning symmetry breaking

In Chapter 2, positioning symmetry breaking of the nucleus-like large structures was studied. When the cytoplasmic actomyosin networks were confined in extracts-in-oil droplets, a nucleus-like spherical cluster made of the accumulated organelles was formed, in which I regarded the cluster as a model of the cell nucleus. Notably, the cluster took the two distinct positions depending on the size of the droplet, either the center in the large droplets or the edge in the small droplets. Based on the quantitative image analysis, we found that the driving forces of the positioning, in which the inwardly directed force was generated by a ring-shaped actin wave is repeatedly generated from the droplet surface to the center, while the outwardly directed force was generated by actin bridges connecting the cluster and the droplet surface. Based on this observation, we proposed a "tug-of-war model" in which the cluster position was determined by the balance of the forces exerted by the actin wave and the actin bridge.

However, this model alone did not explain how the balance of forces broke and positioning symmetry breaking occurs. To understand the mechanism of symmetry breaking, we constructed theoretical models based on the active gel theory of actin

waves and the percolation theory of stochastic bridge formation. Theoretical analysis revealed that the droplet size dependence of the actin wave period was $T \propto R$ and the characteristic time of bridge formation was $\tau_p \propto e^R$. Therefore, $\tau_p < T$ holds for the small droplets and bridge formation dominates, thus the clusters are placed at the edge, while $\tau_p > T$ holds for the large droplets and actin wave generation dominates, thus the clusters are placed at the center. Notably, at the transition point $T = \tau_{\mathrm{p}}$, the following equality holds

$$\frac{R_{\mathrm{c}}}{L} = \log_2\left(\frac{T}{\tau}\right), \tag{5.1}$$

where L is the length of actin filaments, τ is the turnover rate of crosslinkers, and T is assumed to be constant. The estimated transition diameter was $D_{\mathrm{c}} = 2R_{\mathrm{c}} \sim 73$ μm, which was close to the experimentally measured transition point $D_{\mathrm{c}} \sim 85$ μm. Therefore, this model explains the transition of the positioning symmetry as the crossover of the two characteristic time scales required for the maturation of the two distinct actomyosin structures coexisting in the same system. Together, this study will provide a physical understanding of the cluster positioning driven by the actin cytoskeleton, which could also be used as a control principle of the cluster positioning through actin network properties such as length of filaments.

(II) Droplet migration induced by the shape symmetry breaking

In Chapter 3, I expanded the intracellular force generation of the actin cytoskeleton to the force transmission to the external environments to explore the physical determinants of cell migration. In living cells, intracellularly generated contractile forces must be efficiently transmitted to the external environments, by which the cell body is propelled forward. However, because of the inherent complex membrane composition and actin-membrane interactions in living cells, physical determinants responsible for such efficient force transmission have yet to be uncovered. Here, to make the migratory artificial cell model, we imposed the symmetry breaking of cell

shape in addition to the positioning symmetry breaking. Using this artificial cell model, I can specify the actin-membrane interaction and the membrane-substrate interaction. Initially, F-actin bound to the membrane accumulates the actomyosin networks at one part of the membrane, inducing a rear-ward polarized actin flow. This polarized actin flow generates active friction at the droplet-substrate interface, propelling the droplet. Strikingly, our results showed that (i) actin-membrane binding and (ii) substrate contact are sufficient to transmit contractile forces to the external environments, uncovering the essential physical determinants for efficient force transmission. In living cells, migration onset is triggered by the polarization of actomyosin networks, and actin flow-induced friction generates propulsion forces. Notably, we showed that such polarization and force transmission can be achieved by the self-organization of membrane-bound actomyosin networks alone, without the help of biochemical signaling or specific adhesive proteins.

Moreover, we found that the migration speed of the actomyosin droplets can be controlled through confinement geometry, namely, it was slower under stronger confinement. The theoretical model suggested that the geometry-dependent balance between active friction $F_{\text{fric}}^{\text{contact}} \propto \pi R_c^2$ and passive fluid drag $F_{\text{drag}} \propto \eta_{\text{oil}} \nabla^2 v_{\text{oil}}$ determines the migration speed, where R_c is the contact radius, η_{oil} is the viscosity of the surrounding oil, and v_{oil} is the velocity of the surrounding oil. Based on this model, we derived the following geometric scaling,

$$\frac{2\eta_{\text{oil}} V_{\text{drop}}}{v_{\text{act}} D} = \alpha \, g(h/D) \tag{5.2}$$

where $g(h/D) \equiv (h/D)(1+(h/D)^2)^{-1}(1-(h/D)f(\theta))^2$, h is the height of the chamber, D is the diameter of the droplet, V_{drop} is the migration speed, v_{act} is the actin flow velocity, α is the friction coefficient, which was confirmed in experiment. Based on the theoretical model, we can explain how the migration speed is determined by

the confinement geometry as follows. At a fixed chamber height, migration speed increases with the droplet size because the associated increase of the active friction outweighs that of the fluid drag ((i) $h \ll D$). On the other hand, because the competing forces scale as $F_{\text{drag}} \propto h^{-2}$ and $F_{\text{fric}} \propto \pi R_{\text{c}}^2 \propto h^{-1}$, as the chamber height decreases ((ii) $h \to 0$), the increase of the passive fluid drag outweighs that of the active friction, resulting in the slow migration speed. Conversely, as the chamber height becomes close to the droplet diameter ((iii) $h \sim D$), although the fluid drag decreases, the active friction is inevitably decreased due to the smaller contact area between the droplet and the substrate, leading to the smaller droplet migration. Thus, we provide a basic physical mechanism of the actomyosin-based motility determined by the balance between the active friction and the passive fluid drag. Together, these findings not only provide a basic physical understanding of the actomyosin-based motility but also provide the founding ground to control cell migration capacity through actin flow-induced active friction and microenvironmental geometry from in vitro models to living cells.

(III) Rotational symmetry breaking induced actomyosin wave dynamics

In Chapter 4, I explored how self-organized actin cytoskeleton undergoes various dynamical states. The dynamical behaviors of the actin cytoskeleton are often observed in living systems, such as cytoplasmic flow, rotational waves, and pulsatile contractions. However, the physical condition to switch the different dynamical states is often difficult to find out because the complex biochemical regulations obscure the underlying mechanics. Here, I use the artificial cell as a simplified closed system in which contractile actin cytoskeleton are confined, and asked what is the minimal physical condition to switch the different dynamic states. By combining the molecular perturbation experiments and numerical simulation of the active gel theory considering the force balance and the mass conservation, I found that the key determinants of

the state transition are the contractility and the polymerization speed. Notably, we experimentally found that the sufficiently stronger actin-membrane binding induced the rotational symmetry breaking, undergoing the revolving wave. The numerical simulation revealed that the initial time delay of the contraction is key to realizing the rotational wave. These results will provide the mechanical understanding of the dynamical behavior of actin cytoskeleton controlled through physical properties and help to develop a unified theory of active gel dynamics.

Together, in this thesis, I have explored the various actomyosin dynamics by focusing on the characteristic symmetry breaking of the system. At a first glance, nucleus positioning, migration, and wave dynamics were different phenomena observed in the distinct cell types. On the contrary, we have successfully realized such distinct phenomena using the artificial cell droplets, and elucidated the underlying physical principles using active gel theory, and classified them based on characteristic symmetries. This suggests that living cells possess a flexible ability that in principle perform different dynamics such as positioning, migration, and wave, which might be responsible for the adaptability and susceptibility of the living systems. The mechanical understanding of the cellular symmetry breaking revealed in this thesis could also be tested and utilized in living cells to control cell function using modern tools such as optogenetics, which remains a significant future challenge (Fig. 5.1). Understanding the simple physical principles of the confined actomyosin networks using artificial cells will expand our knowledge of self-organization and develop a basic understanding of the out-of-equilibrium physics of cellular symmetry breaking.
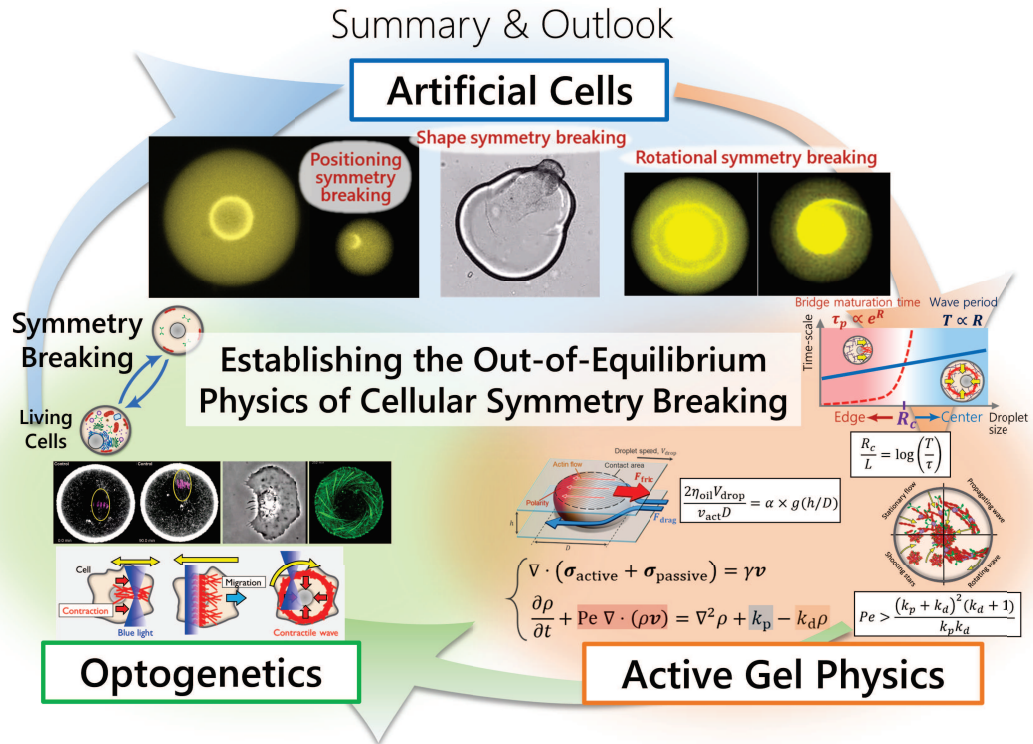
Figure 5.1: Summary and outlook of this thesis. We utilized the artificial cells to extract characteristic symmetry breakings in the living cells (from the left bottom to the top), which enables us quantitative image analysis and the theoretical modeling based on active gel theory (from the top to the bottom right). This will provide mechanical understanding for the cellular symmetry breaking, and could also be tested and utilized in living cells to control cell function using optogenetics, which remains a significant future challenge (from the right to the left). Combining the wide varieties of experimental and theoretical disciplines, we could establish the out-of-equilibrium physics of cellular symmetry breaking.

References

[1] Landau, L. D. & Lifshitz, E. M. *E. Mechanics, Third Edition: Volume 1 (Course of Theoretical Physics)*, Butterworth-Heinemann, 3 edition, (1976).

[2] Spaldin, N. A. *Magnetic Materials: Fundamentals and Applications, Cambridge University Press*, Cambridge, (2010).

[3] Nanbu, Y. Nobel Lecture. NobelPrize.org. Nobel Prize Outreach AB 2021. Thu. 23 Dec 2021. https://www.nobelprize.org/prizes/physics/2008/nambu/lecture/

[4] Almonacid, M., Ahmed, W. W., Bussonnier, M., Mailly, P., Betz, T., Voituriez, R., Gov, N. S. & Verlhac, M.-H. Active diffusion positions the nucleus in mouse oocytes. *Nat. Cell Biol.* **17,** 470-479 (2015).

[5] Schuh, M. & Ellenberg, J. A new model for asymmetric spindle positioning in mouse oocytes. *Curr. Biol.* **18,** 1986-1992 (2008).

[6] Azoury, J., Lee, K. W., Georget, V., Rassinier, P., Leader, B. & Verlhac, M.-H. Spindle positioning in mouse oocytes relies on a dynamic meshwork of actin filaments. *Curr. Biol.* **18,** 1514-1519 (2008).

[7] Yam, P. T., Wilson, C. A., Ji, L., Hebert, B., Barnhart, E. L., Dye, N. A., Wiseman, P. W., Danuser, G. & Theriot, J. A. Actin myosin network reorganization breaks symmetry at the cell rear to spontaneously initiate polarized cell motility. *J. Cell Biol.* **178,** 1207-1221 (2007).

[8] Tee, Y. H., Shemesh, T., Thiagarajan, V., Hariadi, R. F., Anderson, K. L., Page, C., Volkmann, N., Hanein, D., Sivaramakrishnan, S., Kozlov, M. M. & Bershadsky, A. D. Cellular chirality arising from the self-organization of the actin cytoskeleton. *Nat. Cell Biol.* **17,** 445-457 (2015).

[9] Salbreux, G., Charras, G. & Paluch, E. Actin cortex mechanics and cellular morphogenesis. *Trends Cell Biol.* **22,** 536-545 (2012).

[10] Sedzinski, J., Biro, M., Oswald, A., Tinevez, J.-Y., Salbreux, G. & Paluch, E. Polar actomyosin contractility destabilizes the position of the cytokinetic furrow. *Nature* **476**, 462-466 (2011).

[11] Ruprecht, V., Wieser, S., Callan-Jones, A., Smutny, M., Morita, H., Sako, K., Barone, V., Ritsch-Marte, M., Sixt, M., Voituriez, R. & Heisenberg, C.-P. Cortical contractility triggers a stochastic switch to fast amoeboid cell motility. *Cell* **160**, 673-685 (2015).

[12] Holubcová, Z., Howard, G. & Schuh, M. Vesicles modulate an actin network for asymmetric spindle positioning. *Nat. Cell Biol.* **15,** 937-947 (2013).

[13] Bergert, M., Erzberger, A., Desai, R. A., Aspalter, I. M., Oates, A. C., Charras, G., Salbreux, G. & Paluch, E. K. Force transmission during adhesion-independent migration. *Nat. Cell Biol.* **17**, 524–529 (2015).

[14] Chou, S. Z. & Pollard, T. D. Mechanism of actin polymerization revealed by cryo-EM structures of actin filaments with three different bound nucleotides. *Proc. Natl. Acad. Sci. USA* **116**, 4265–4274 (2019).

[15] Chugh, P., Clark, A. G., Smith, M. B., Cassani, D. A. D., Dierkes, K., Ragab, A., Roux, P. P., Charras, G., Salbreux, G. & Paluch, E. K. Actin cortex architecture regulates cell surface tension. *Nat. Cell Biol.* **19**, 689–697 (2017).

[16] Field, C. M., W'uhr, M., Anderson, G. A., Kueh, H. Y., Strickland, D. & Mitchison, T. J. Actin behavior in bulk cytoplasm is cell cycle regulated in early vertebrate embryos. *J. Cell Sci.* **124**, 2086–2095 (2011).

[17] Murrell, M., Pontani, L.-L., Guevorkian, K., Cuvelier, D., Nassoy, P. & Sykes, C. Spreading dynamics of biomimetic actin cortices. *Biophys. J.* **100**, 1400–1409 (2011).

[18] Pinot, M., Chesnel, F., Kubiak, J. Z., Arnal, I., Nedelec, F. J. & Gueroui, Z. Effects of confinement on the self-organization of microtubules and motors. *Curr. Biol.* **19,** 954-960 (2009).

[19] Kühler, S. & Bausch, A. R. Contraction mechanisms in composite active actin networks. *PLoS ONE* **7**, e39869 (2012).

[20] Reymann, A.-C., Boujemaa-Paterski, R., Martiel, J.-L., Guérin, C., Cao, W., Chin, H. F., Cruz, E. M. D. L., Théry, M. & Blanchoin, L. Actin network architecture can determine myosin motor activity. *Science* **336**, 1310–1314 (2012).

[21] Good, M. C., Vahey, M. D., Skandarajah, A., Fletcher, D. A. & Heald, R. Cytoplasmic volume modulates spindle size during embryogenesis. *Science* **342,** 856-860 (2013).

[22] Hazel, J., Krutkramelis, K., Mooney, P., Tomschik, M., Gerow, K., Oakey, J. & Gatlin, J. C. Changes in cytoplasmic volume are sufficient to drive spindle scaling. *Science* **342,** 853-856 (2013).

[23] Pinot, M., Steiner, V., Dehapiot, B., Yoo, B.-K., Chesnel, F., Blanchoin, L., Kervrann, C. & Gueroui, Z. Confinement induces actin flow in a meiotic cytoplasm. *Proc. Natl. Acad. Sci. USA* **109,** 11705-11710 (2012).

[24] Malik-Garbi, M., Ierushalmi, N., Jansen, S., Abu-Shah, E., Goode, B. L., Mogilner, A. & Keren, K. Scaling behaviour in steady-state contracting actomyosin networks. *Nat. Phys.* **15**, 509-516 (2019).

[25] Shah, E. A. & Keren, K. Symmetry breaking in reconstituted actin cortices. *eLife* **3**, e01433 (2014).

[26] Tan, T. H., Malik-Garbi, M., Abu-Shah, E., Li, J., Sharma, A., MacKintosh, F. C., Keren, K., Schmidt, C. F. & Fakhri, N. Self-organized stress patterns drive state transitions in actin cortices. *Sci. Adv.* **4**, eaar2847 (2018).

[27] Bendix, P. M., Koenderink, G. H., Cuvelier, D., Dogic, Z., Koeleman, B. N., Brieher, W. M., Field, C. M., Mahadevan, L., Weitz, D. A. A quantitative analysis of contractility in active cytoskeletal protein networks. *Biophys. J.* **94**, 3126–3136 (2008).

[28] Sakamoto, R., Tanabe, M., Hiraiwa, T., Suzuki, K., Ishiwata, S., Maeda, Y. T.& Miyazaki, M, Tug-of-war between actomyosin-driven antagonistic forces determines the positioning symmetry in cell-sized confinement. *Nat. Commun.* **11**, 3063 (2020).

[29] Ierushalmi, N., Malik-Garbi, M., Manhart, A., Shah, E. A., Goode, B. L., Mogilner, A. & Keren, K. Centering and symmetry breaking in confined contracting actomyosin networks. *eLife* **9**, e55368 (2020).

[30] Simon, C., Kusters, R., Caorsi, V., Allard, A., Abou-Ghali, M., Manzi, J., Cicco, A. D., Lévy, D., Lenz, M., Joanny, J.-F., Campillo, C., Plastino, J., Sens, P. & Sykes, C. Actin dynamics drive cell-like membrane deformation. *Nat. Phys.* **15**, 602-609 (2019).

[31] Litschel, T., Kelley, C. F., Holz, D., Koudehi, M. A., Vogel, S. K., Burbaum, L., Mizuno, N., Vavylonis, D. & Schwille, P. Reconstitution of contractile actomyosin rings in vesicles. *Nat. Commun.* **12**, 2254 (2021).

[32] Green, R. A., Paluch, E. & Oegema, K. Cytokinesis in animal cells. *Annu. Rev. Cell Dev. Biol.* **28**, 29-58 (2012).

[33] Takagi, J., Sakamoto, R., Shiratsuchi, G., Maeda, Y. T. & Shimamoto, Y. Mechanically distinct microtubule arrays determine the length and force response of the meiotic spindle. *Dev. Cell* **49,** 267-278 (2019).

[34] Sakamoto, R., Noireaux, V. & Maeda, Y. T. Anomalous scaling of gene expression in confined cell-free reactions. *Sci. Rep.* **8,** 7364 (2018).

[35] Paluch, E. K., Aspalter, I. M. & Sixt, M. Focal adhesion-independent cell migration. *Annu. Rev. Cell Dev. Biol.* **32**, 469-490 (2016).

[36] Kruse, K., Joanny, J. F., J́ulicher, F., Prost, J. & Sekimoto, K. Generic theory of active polar gels: A paradigm for cytoskeletal dynamics. *Euro. Phys. J. E* **16**, 5-16 (2005).

[37] Joanny, J. F., J́ulicher, F., Kruse, K. & Prost, J. Hydrodynamic theory for multi-component active polar gels. *New J. Phys.* **9**, 411 (2007).

[38] Banerjee, S. & Marchetti, C. M. Instabilities and oscillations in isotropic active gels. *Soft Matter* **7**, 463-473 (2011).

[39] Banerjee, S., Liverpool, T. B. & Marchetti, C. M. Generic phases of cross-linked active gels: Relaxation, oscillation and contractility. *Euro. Phys. Lett.* **96**, 58004 (2011).

[40] Bois, J. S., J́ulicher, F. & Grill, S. W. Pattern formation in active fluids. *Phys. Rev. Lett.* **106**, 028103 (2011).

[41] Kumar, K. V., Bois, J. S., J́ulicher, F. & Grill, S. W. Palsatory patterns in active fluids. *Phys. Rev. Lett.* **112**, 208101 (2014).

[42] Moore, T., Wu, S. K., Michael, M., Yap, A. S., Gomez, G. A. & Neufeld, Z. Self-organizing actomyosin patterns on the cell cortex at epithelial cell-cell junctions. *Biophys. J.* **107**, 2652-2661 (2014).

[43] Hiraiwa, T. & Salbreux, G. Role of turnover in active stress generation in a filament network. *Phys. Rev. Lett.* **116**, 188101 (2016).

[44] Prost, J., J´ulicher, F. & Joanny, J. F. Active gel physics. *Nat. Phys.* **11**, 111-117 (2015).

[45] Tinevez, J.-Y., Schulze, U., Salbreux, G., Roensch, J., Joanny, J.-F. & Paluch, E. Role of cortical tension in bleb growth. *Proc. Natl. Acad. Sci. USA* **106**, 18581-18586 (2009).

[46] Turlier, H., Audoly, B., Prost, J. & Joanny, J. F. Furrow constriction in animal cell cytokinesis. *Biophys. J.* **106**, 114-123 (2014).

[47] Reversat, A., Gaertner, F., Merrin, J., Stopp, J., Tasciyan, S., Aguilera, J., de Vries, I., Hauschild, R., Hons, M., Piel, M., Callan-Jones, A., Voituriez, R. & Sixt, M. Cellular locomotion using environmental topography. *Nature* **582**, 582-585 (2020).

[48] Mayer, M., Depken, M., Bois, J. S., J´ulicher, F. & Grill, S. W. Anisotropies in cortical tension reveal the physical basis of polarizing cortical flows. *Nature* **467**, 617-621 (2010).

[49] Shamipour, S., Kardos, R., Xue, S.-L., Hof, B., Hannezo, E. & Heisenberg, C.-P. Bulk actin dynamics drive phase segregation in zebrafish oocytes. *Cell* **177**, 1463-1479 (2019).

[50] Levernier, N. & Kruse, K. Spontaneous formation of chaotic protrusions in a polymerizing active gel layer. *New J. Phys.* **22**, 013003 (2020).

[51] Miller, K. G. Extending the Arp2/3 complex and its regulation beyond the leading edge. *J. Cell Biol.* **156**, 591-593 (2002).

[52] Maan, R., Loiseau, E. & Bausch, A. R. Adhesion of active cytoskeletal vesicles. *Biophys. J.* **115**, 2395-2402 (2018).

[53] Liu, A. P., Richmond, D. L., Maibaum, L., Pronk, S., Geissler, P. L. & Fletcher, D. A. Membrane induced bundling of actin filaments. *Nat. Phys.* **4**, 789-793 (2008).

[54] Boukellal, H., Campás, O., Joanny, J. F., Prost, J. & Sykes, C. Soft Listeria : actin-based propulsion of liquid drops. *Phys. Rev. E* **69,** 061906 (2004).

[55] Bermudez, J. G., Chen, H., Einstein, L. C. & Good, M. C. Probing the biology of cell boundary conditions through confinement of *Xenopus* cell-free cytoplasmic extracts. *genesis* **55**, e23013 (2017).

[56] W'uhr, M., Freeman Jr, R. M., Presler, M., Horb, M. E., Peshkin, L., Gygi, S. & Kirschner, M. W. Deep proteomic of the *Xenopus laevis* egg using an mRNA-derived reference database. *Curr. Biol.* **24,** 1467-1475 (2014).

[57] Smith, B. A., Padrick, S. B., Doolittle, L. K., Daugherty-Clarke, K., Corrêa Jr, I. R., Xu, M.-Q., Goode, B. L., Rosen, M. K. & Gelles, J. Three-color single molecule imaging shows WASP detachment from Arp2/3 complex triggers actin filament branch formation. *eLife* **2,** e08008 (2013).

[58] Alvarado, J., Sheinman, M., Sharma, A., MacKintosh, F. C. & Koenderink, G. H. Molecular motors robustly drive active gels to a critically connected state. *Nat. Phys.* **9,** 591-597 (2013).

[59] Alvarado, J., Sheinman, M., Sharma, A., MacKintosh, F. C. & Koenderink, G. H. Force percolation of contractile active gels. *Soft Matt.* **13,** 5624-5644 (2017).

[60] Loiseau, E., Schneider, J. A. M., Keber, F. C., Pelzl, C., Massiera, G., Salbreux, G. & Bausch, A. R. Shape remodeling and blebbing of activecytoskeletal vesicles. *Sci. Adv.* **2,** e1500465 (2016).

[61] Dierkes, K., Sumi, A., Solon, J. & Salbreux, G. Shape remodeling and blebbing of activecytoskeletal vesicles. *Phys. Rev. Lett.* **113,** 148102 (2014).

[62] Banerjee, D. S., Munjal, A., Lecuit, T. & Rao, M. Actomyosin pulsation and flows in an active elastomer with turnover and network remodeling. *Nat. Commun.* **8,** 1121 (2017).

[63] Howard, J. *Mechanics of motor protein and the cytoskeleton.* Sinauer, New York, (2000).

[64] Ideses, Y., Erukhimovitch, V., Brand, R., Jourdain, D., Hernandez, J. S., Gabinet, U. R., Safran, S. A., Kruse, K. & Bernheim-Groswasser, A. Spontaneous buckling of contractile poroelastic actomyosin sheets. *Nat. Commun.* **9,** 2461 (2018).

[65] Parsons, J. T., Horwitz, A. R. & Schwartz, M. A. Cell adhesion: integrating cytoskeletal dynamics and cellular tension. *Nat. Rev. Mol. Cell Biol.* **11**, 633-643 (2010).

[66] Liu, Y.-J., Berre, M. L., Lautenschlaeger, F., Maiuri, P., Callan-Jones, A., Heuzé, M., Takaki, T., Voituriez, R. & Piel, M. Confinement and low adhesion induce fast amoeboid migration of slow mesenchymal cells. *Cell* **160**, 659-672 (2015).

[67] https://www.mechanobio.info/cytoskeleton-dynamics/what-are-lamellipodia-and-lamella/what-steps-are-involved-in-lamellipodia-assembly/

[68] https://www.reading.ac.uk/nitricoxide/intro/migration/adhesion.htm

[69] Goehring, N. W., Trong, P. K., Bois, J. S., Chowdhury, D., Nicola, E. M., Hyman, A. A. & Grill, S. W. Polarization of PAR proteins by advective triggering of a pattern-forming system. *Science* **334,** 1137-1141 (2011).

[70] Gundersen, G. G. & Worman, H. J. Nuclear positioning. *Cell* **152,** 1376-1389 (2013).

[71] Chaigne, A., Campillo, C., Gov, N. S., Voituriez, R., Azoury, J., Umana-Diaz, C., Almonacid, M., Queguiner, I., Nassoy, P., Sykes, C., Verlhac, M.-H. & Terret, M.-E. A soft cortex is essential for asymmetric spindle positioning in mouse oocytes. *Nat. Cell Biol.* **15,** 958-966 (2013).

[72] Brunet, S. & Maro, B. Germinal vesicle position and meiotic maturation in mouse oocyte. *Reproduction* **133,** 1069-1072 (2007).

[73] Levi, M., Ghetler, Y., Shulman, A. & Shalgi, R. Morphological and molecular markers are correlated with maturation-competence of human oocytes. *Hum. Reprod.* **28,** 2482-2489 (2013).

[74] Leader, B., Lim, H., Carabatsos, M. J., Harrington, A., Ecsedy, J., Pellman, D., Maas, R. & Leder, P. Formin-2, polyploidy, hypofertility, and positioning of the meiotic spindle in mouse oocytes. *Nat. Cell Biol.* **4,** 921-928 (2003).

[75] McNally, F. J. Mechanisms of spindle positioning. *J. Cell Biol.* **200,** 131-140 (2013).

[76] Li, H., Guo, F., Rubinstein, B. & Li, R. Actin-driven chromosomal motility leads to symmetry breaking in mammalian meiotic oocytes. *Nat. Cell Biol.* **10,** 1301-1308 (2008).

[77] Bezanill, M. & Wadsworth, P. Spindle positioning: actin mediates pushing and pulling. *Curr. Biol.* **19,** R168-R169 (2009).

[78] Yi, K., Unruh, J. R., Deng, M., Slaughter, B. D., Rubinstein, B. & Li, R. Dynamic maintenance of asymmetric meiotic spindle position through Arp2/3-complex-driven cytoplasmic streaming in mouse oocytes. *Nat. Cell Biol.* **13,** 1252-1258 (2011).

[79] Yi, K., Rubinstein, B. & Li, R. Symmetry breaking and polarity establishment during mouse oocyte maturation. *Phil. Trans. R. Soc. B* **368,** 20130002 (2013).

[80] Riedl, J., Crevenna, A. H., Kessenbrock, K., Yu, J. H., Neukirchen, D., Bista, M., Bradke, F., Jenne, D., Holak, T. A., Werb, W., Sixt, M. & Wedlich-Soldner, R. Lifeact: a versatile marker to visualize F-actin. *Nat. Methods* **5,** 605-607 (2008).

[81] Courtemanche, N., Pollard, T. D. & Chen, Q. Avoiding artifacts when counting polymerized actin in live cells with Lifeact-fluorescent fusion proteins. *Nat. Cell Biol.* **18,** 676-683 (2016).

[82] Sliogeryte, K., Thorpe, S. D., Wang, Z., Thompson, C. L., Gavara, N. & Knight, M. M. Differential effects of LifeAct-GFP and actin-GFP on cell mechanics assessed using micropipette aspiration. *J. Biomech.* **49,** 310-317 (2016).

[83] Lin, K. M., Mejillano, M. & Yin, H. L. Ca^{2+} regulation of gelsolin by its C-terminal tail. *J. Biochem.* **275,** 27746-27752 (2000).

[84] Miyazaki, M., Kinosita, K., Jr & Shiroguchi, K. Accurate polarity control and parallel alignment of actin filaments for myosin-powered transport systems. *RSC Adv.* **3,** 8728-8733 (2013).

[85] Ohki, T., Ohno, C., Oyama, K., Mikhailenko, S. V., & Ishiwata, S. Purification of cytoplasmic actin by affinity chromatography using the C-terminal half of gelsolin. *Biochem. Biophys. Res. Commun.* **383,** 146-150, (2009).

[86] Kühn, S. & Geyer, M. Formins as effector proteins of Rho GTPases. *Small GT-Pases* **5,** e983876 (2014).

[87] Kovar, D. R., Harris, E. S., Mahaffy, R., Higgs, H. N. & Pollard, T. D. Control of the assembly of ATP- and ADP-actin by formins and profilin. *Cell* **124,** 423-435 (2006).

[88] Kubota, H., Miyazaki, M., Ogawa, T., Shimozawa, T., Kinosita Jr, K. & Ishiwata, S. Biphasic effect of profilin impacts the formin mDia1 force-sensing mechanism in actin polymerization. *Biophys. J.* **113,** 461-471 (2017).

[89] Kubota, H., Miyazaki, M., Ogawa, T., Shimozawa, T., Kinosita Jr., K. & Ishiwata, S. Processive nanostepping of formin mDia1 loosely coupled with actin polymerization. *Nano Lett.* **18,** 6617-6624 (2018).

[90] Stauffer, D. & Aharony, A. *Introduction to Percolation Theory*, Taylor & Francis, (1991).

[91] Hu, B., Fuller, D., Loomis, W. F., Levine, H. & Rappel, W. J. Phenomenological approach to eukaryotic chemotactic efficiency. *Phys. Rev. E* **81,** 031906 (2010).

[92] Wachsstock, D. H., Schwarz, W. H. & Pollard, T. D. Cross-linker dynamics determine the mechanical properties of actin gels. *Biophys. J.* **86,** 801-809 (1994).

[93] W'uhr, M., Freeman Jr, R. M., Presler, M., Horb, M. E., Peshkin, L., Gygi, S. & Kirschner, M. W. Deep proteomic of the *Xenopus laevis* egg using an mRNA-derived reference database. *Curr. Biol.* **24,** 1467-1475 (2014).

[94] Amulic, B., Cazalet, C., Hayes, G. L., Metzler, K. D. & Zychlinsky, A. Neutrophil function: from mechanisms to disease annual review of immunology. *Annu. Rev. Immunol.* **30,** 459-489 (2012).

[95] Bodor, D. L., P$'$onisch, W., Endres, R. G. & E. K. Paluch, Of cell shapes and motion: the physical basis of animal cell migration. *Dev. Cell* **52**, 550-562 (2020).

[96] Paluch, E. K., Aspalter, I. M. & Sixt, M. Focal adhesion-independent cell migration. *Annu. Rev. Cell Dev. Biol.* **32**, 469-490 (2016).

[97] Yamada, K. M. & Sixt, M. Mechanisms of 3D cell migration. *Nat. Rev. Mol. Cell Biol.* **20**, 738–752 (2019).

[98] Paul, C. D., Mistriotis, P. & Konstantopoulos, K. Cancer cell motility: lessons from migration in confined spaces *Nat. Rev. Cencer* **17**, 131–140 (2017).

[99] Tinevez, J.-Y., Perry, N., Schindelin, J., Hoopes, G. W., Reynolds, G. W., Laplantine, E., Bednarek, S. Y., Shorte, S. K. & Eliceiri, K. W. TrackMate: an open and extensible platform for single-particle tracking. *Methods* **115**, 80–90 (2017).

[100] Fukami, K., Endo, T., Imamura, M. & Takenawa, T. α-Actinin and vinculin are PIP$_2$-binding proteins involved in signaling by tyrosine kinase. *J. Biol. Chem.* **269**, 1518-1522 (1994).

[101] Kelley, C. F., Litschel, T., Schumacher, S., Dedden, D., Schwille, P. & Mizuno, N. Phosphoinositides regulate force-independent interactions between talin, vinculin, and actin. *eLife* **9**, e56110 (2020).

[102] Saarikangas, J., Zhao, H. & Lappalainen, P. Regulation of the actin cytoskeleton-plasma membrane interplay by phosphoinositides. *Physiol. Rev.* **90**, 259–289 (2010).

[103] Abercrombie, M., Heaysman, J. E. & Pegrum, S. M. The locomotion of fibroblasts in culture. 3. Movements of particles on the dorsal surface of the leading lamella. *Exp. Cell Res.* **62**, 389–398 (1970).

[104] Bausch, A. R., Ziemann, F., Boulbitch, A. A., Jacobson, K. & Sackmann, E. Local measurements of viscoelastic parameters of adherent cell surfaces by magnetic bead microrheometry. *Biophys. J.* **75**, 2038-2049 (1998).

[105] Eri, A. & Okumura, K. Viscous drag friction acting on a fluid drop confined in between two plates. *Soft Matter* **7**, 5648-5653 (2011).

[106] Maiuri, P., Rupprecht, J.-F., Wieser, S., Ruprecht, V., Bénichou, O., Carpi, N., Coppey, M., Beco, S. D., Gov, N., Heisenberg, C.-P., Crespo, C. L., Lautenschlaeger, F., Berre, M. L., Lennon-Dumenil, A.-M., Raab, M., Thiam, H.-R., Piel, M., Sixt, M. & Voituriez, R. Actin flows mediate a universal coupling between cell speed and cell persistence. *Cell* **161**, 374-386 (2015).

[107] Sanchez, T., Chen, D. T. N., DeCamp, S. J., Heymann, M. & Dogic, Z. Spontaneous motion in hierarchically assembled active matter. *Nature* **491**, 431-434 (2012).

[108] Venturini, V., Pezzano, F., Castro, F. C., H′akkinen, H.-M., Jiménez-Delgado, S., Colomer-Rosell, M., Marro, M., Tolosa-Ramon, Q., Paz-López, S., Valverde, M. A., Weghuber, J., Loza-Alvarez, P., Krieg, M., Wieser, S. & Ruprecht, V. The nucleus measures shape changes for cellular proprioception to control dynamic cell behavior. *Science* **370**, eaba2644 (2020).

[109] Elosegui-Artola, A., Andreu, I., Beedle, A. E. M., Lezamiz, A., Uroz, M., Kosmalska, A. J., Oria, R., Kechagia, J. Z., Rico-Lastres, P., Roux, A.-L. L., Shanahan, C. M., Trepat, X., Navajas, D., Garcia-Manyes, S. & Roca-Cusachs, P. Force triggers YAP nuclear entry by regulating transport across nuclear pores. *Cell* **171**, 1397–1410 (2017).

[110] Rianna, C., Radmacher & M., Kumar, S. Direct evidence that tumor cells soften when navigating confined spaces. *Mol. Biol. Cell* **31**, 1726–1734 (2020).

[111] Miyazaki, M., Chiba, M., Eguchi, H., Ohki, T. & Ishiwata, S. Cell-sized spherical confinement induces the spontaneous formation of contractile actomyosin rings *in vitro. Nat. Cell Biol.* **17,** 480-489 (2015).

[112] Kondo, S. & Miura, T. Reaction-diffusion model as a framework for understanding biological pattern formation. *Science* **329,** 1616-1620 (2010).

[113] Raskin, D. M. & de Borer, P. A. Rapid pole-to-pole oscillation of a protein required for directing division to the middle of Escherichia coli. *Proc. Natl. Acad. Sci. USA* **96,** 4971-4976 (1999).

[114] Raskin, D. M. & de Borer, P. A. MinDE-dependent pole-to-pole oscillation of division inhibitor MinC in Escherichia coli. *J. Bacteriol.* **181,** 6419-6424 (1999).

[115] Marcon, L., Diego, X., Sharpe, J. & M´uller, P. High-throughput mathematical analysis identifies Turing networks for patterning with equally diffusing signals. *eLife* **5,** e14022 (2016).

[116] Driscoll, M. K., Losert, W., Jacobson, K., & Kapustina, M. Spatiotemporal relationships between the cell shape and the actomyosin cortex of periodically protruding cells. *Cytoskeleton* **72,** 268-281 (2015).

[117] Mitsushima, M., Aoki, K., Ebisuya, M., Matsumura, S., Yamamoto, T., Matsuda, M., Toyoshima, F. & Nishida, E. Revolving movement of a dynamic cluster of actin filaments during mitosis. *J. Cell Biol.* **191,** 453-462 (2010).

[118] Charras, G. T., Coughlin, M., Mitchison, T. J. & Mahadevan, L. Life and times of a cellular bleb. *Biophys. J.* **94,** 1836-1853 (2008).

[119] Shao, D., Rappel, W. J. & Levine, H. Computational model for cell morphodynamics. *Phys. Rev. Lett.* **105,** 108104 (2010).

[120] Ziebert, F., Swaminathan, S. & Aranson, I. S. Model for self-polarization and motility of keratocyte fragments. *J. R. Soc. Interface* **9,** 1084-1092 (2012).

[121] Goff, T. L., Liebchen, B. & Marenduzzo, D. Actomyosin contraction induces in-bulk motility of cells and droplets. *Biophys. J.* **119,** 1025-1032 (2020).

[122] Alama-Bermejo, G., Holzer, A. S. & Bartholomew, J. L. Myxozoan adhesion and virulence: ceratonova shasta on the move. *Microorganisms* **7,** 397 (2019).

Acknowledgements

I would like to thank my esteemed supervisor – Dr. Yusuke T. Maeda for his invaluable supervision, support, and tutelage during the course of my PhD degree. My gratitude extends to the Japan Society for the Promotion of Science for the funding opportunity to undertake my studies. Additionally, I would like to express gratitude to Dr. Makito Miyazaki for his treasured support which was influential in shaping my experiment methods and critiquing my results. I also thank Dr. Guillaume Charras, Dr. Tetuya Hiraiwa, Dr. Yuta Shimamoto, for their mentorship. I thank my dissertation committee – Prof. Daisuke Mizuno and Prof. Yasuyuki Kimura for their critical reading of my dissertation. I would like to thank my friends, lab mates, colleagues, and research team – Dr. Tatuya Fukuyama, Dr. Kazusa Beppu, Dr. Ziane Izri, for a cherished time spent together in the lab, and in social settings. My appreciation also goes out to my family and friends for their encouragement and support all through my studies.

Publication

Original articles

- Ryota Sakamoto, Masatoshi Tanabe, Tetsuya Hiraiwa, Kazuya Suzuki, Shin'ichi Ishiwata, Yusuke T. Maeda, Makito Miyazaki, Tug-of-war between actomyosin-driven antagonistic forces determines the positioning symmetry in cell-sized confinement. *Nature Communications* **11,** 3063, (2020).

- Ryota Sakamoto, Ziane Izri, Yuta Shimamoto, Makito Miyazaki, Yusuke T. Maeda, Geometric trade-off between active friction and viscous drag determines actomyosin-based motility of a cell-sized droplet. (*in review*).

- Jun Takagi, Ryota Sakamoto, Gen Shiratsuchi, Yusuke T. Maeda, Yuta Shimamoto, Mechanically distinct microtubule arrays determine the length and force response of the meiotic spindle. *Developmental Cell* **49,** 267-278 (2019).

- Ryota Sakamoto, Vincent Noireaux, Yusuke T. Maeda, Anomalous scaling of gene expression in confined cell-free reactions. *Scientific Reports* **8,** 7364 (2018).

Review articles

- Kazusa Beppu, Ziane Izri, Yusuke T. Maeda, Ryota Sakamoto, Geometric effect for biological reactors and biological fluids. *Bioengineering* **5,** 110 (2018).